Quantum simulation using ultracold atoms in two-dimensional optical lattices

Sarah Al-Assam

A thesis submitted in partial fulfilment of
the requirements for the degree of
Doctor of Philosophy at the University of Oxford

Balliol College
University of Oxford
Michaelmas Term 2010

Abstract

Quantum simulation using ultracold atoms in two-dimensional optical lattices

Sarah Al-Assam, Balliol College, Oxford
D.Phil thesis, Michaelmas 2010

Ultracold atoms in optical lattices can be used to model condensed matter systems. They provide a clean, tuneable system which can be engineered to reach parameter regimes that are not accessible in condensed matter systems. Furthermore, they provide different techniques for probing the properties of these systems.

This thesis presents an experimental and theoretical study of ultracold atoms in optical lattices for quantum simulation of two-dimensional systems. The first part of this thesis describes an experiment with a Bose-Einstein condensate of ^{87}Rb loaded into a two-dimensional optical lattice. The beams that generate the optical lattice are controlled by acousto-optic deflection to provide a flexible optical lattice potential. The use of a dynamic 'accordion' lattice with ultracold atoms, where the spacing of the lattice is increased in both directions from 2.2 to 5.5 μm, is described. This technique allows an experiment such as quantum simulations to be performed with a lattice spacing smaller than the resolution limit of the imaging system, while allowing imaging of the atoms at individual lattice sites by subsequent expansion of the optical lattice. The optical lattice can also be rotated, generating an artificial magnetic field. Previous experiments with the rotating optical lattice are summarised, and steps to reaching the strongly correlated regime are discussed.

The second part of this thesis details numerical techniques that can be used to describe strongly correlated two-dimensional systems. These systems are challenging to simulate numerically, as the exponential growth in the size of the Hilbert space with the number of particles means that they can only be solved exactly for very small systems. Recently proposed correlator product states [Phys. Rev. B **80**, 245116 (2009)] provide a numerically efficient description which can be used to simulate large two-dimensional systems. In this thesis we apply this method to the two-dimensional quantum Ising model, and the Bose-Hubbard model subject to an artificial magnetic field in the regime where fractional quantum Hall states are predicted to occur.

Acknowledgements

I am extremely fortunate to have been part of two groups during my PhD, and as such have many people to thank.

First I must express my sincere gratitude to my supervisors Christopher Foot and Dieter Jaksch for giving my the opportunity to work in their groups. Without their guidance and encouragement I would not have been able to complete this task. Having two such inspirational physicists to advise me was a real privilege.

I extend a special thank you to the two senior colleagues I have had the pleasure of working most closely with: Ross Williams, with whom I worked in the lab and Stephen Clark, who I collaborated with on the theory work. Both have provided me with invaluable help throughout my PhD and very kindly proof-read this thesis. Ross was a great lab partner: his admirable drive and knowledge, and our many rewarding discussions, made for a productive and enjoyable working environment. Stephen was always available as a source of many excellent ideas and interesting discussions, and had a seemingly bottomless reserve of patience for explaining concepts to me!

I would also like to thank those who worked on the experiment in -111 before me: Ben Fletcher, Andrian Harsono and Martin Shotter, either for passing down their skills and knowledge first hand, or through their informative notes in the log book.

Many thanks also to all the many people who made working in Oxford Physics a great experience, in particular Eileen Nugent, Marcus Gildemeister, Ben Sherlock, Marcin Kubasik, and Alexander Klein for their useful advice and assistance, as well as the many other members of both groups who have provided both interesting discussions and camaraderie: Dimitri Trypogeorgos, Ben Sheard, Herbert Crepaz, Amita Deb, Ed Owen, Pierre-Louis Giscard, Uwe Dorner, Simon Thwaite, Richard Walters and Matthias Rosenkranz. Thank you also to our technician Graham Quelch for all his help in keeping the experiment running smoothly.

Of course, I would not have been able to reach this position without the love and support of my family over the years, who always had the right words on hand for both encouragement when things went well and comfort in the event of lab mishaps! A very special thank you to my husband Liam, for his brilliant guidance and help in the areas that his non-physics background allowed, and his unfailing support and understanding during my PhD.

Contents

1 Introduction **1**
- 1.1 Background and motivation . . . 1
- 1.2 Ultracold atoms and optical lattices . . . 3
  - 1.2.1 Bose-Einstein condensation . . . 3
  - 1.2.2 Dipole trapping force . . . 3
  - 1.2.3 Model Hamiltonian in periodic potential . . . 4
- 1.3 Quantum simulation . . . 6
  - 1.3.1 Artificial magnetic fields . . . 6
  - 1.3.2 Spin models . . . 7
- 1.4 Thesis overview . . . 8

2 Experimental arrangement **10**
- 2.1 Producing a BEC . . . 10
- 2.2 Moving to a pancake-shaped geometry . . . 12
- 2.3 Imaging . . . 14
- 2.4 Optical lattice . . . 16
  - 2.4.1 Optical lattice arrangement . . . 16
  - 2.4.2 Characterisation of the optical lattice . . . 21
  - 2.4.3 Loading atoms into the optical lattice . . . 26

3 Optical lattice with dynamically variable periodicity **29**
- 3.1 Single site imaging using an accordion lattice . . . 29
  - 3.1.1 Background . . . 30
  - 3.1.2 Experimental sequence . . . 31
  - 3.1.3 Estimate of minimum ramp time . . . 32
  - 3.1.4 Extensions to technique . . . 36
- 3.2 Other applications of accordion lattice . . . 37
  - 3.2.1 Flexible lattice potentials . . . 37
  - 3.2.2 Adjusting system parameters . . . 37

3.2.3 Spatially varying modulation 37

4 Artificial magnetic fields: mean-field regime and route to strongly-correlated states 39
4.1 Artificial magnetic fields and optical lattices 39
4.1.1 Generating artificial magnetic fields 39
4.1.2 Ground states in an optical lattice 43
4.2 Mean field regime 43
4.2.1 Large particle filling: frustrated Josephson-junction arrays 43
4.2.2 Experiments in the Josephson-junction regime 46
4.2.3 Mean-field states at low and intermediate filling 55
4.3 Strongly correlated states 55
4.3.1 Continuum FQH regime 56
4.3.2 FQH effect near Mott insulator transition 56
4.3.3 High field FQH regime 57
4.3.4 Reaching the strongly correlated regime in a rotating optical lattice 57

5 Correlator product states 61
5.1 Strongly correlated states 62
5.1.1 Hilbert space size 62
5.1.2 Entanglement scaling 62
5.1.3 Tensor network description of many body states 64
5.2 Correlator product states 65
5.2.1 Representing the wave function 66
5.2.2 Relation to matrix product states 67
5.3 Determining the ground-state wave function 70
5.3.1 Calculating expectation values 70
5.3.2 Minimising the energy 73

6 Two-dimensional quantum Ising model 75
6.1 Background 75
6.2 System set-up 76
6.2.1 Correlator types 76
6.2.2 Calculation of energy and derivative 78
6.3 Results 80
6.3.1 Energies 80
6.3.2 Transition point 81
6.3.3 Long-range correlations 85
6.4 Summary 88

7 The fractional quantum Hall effect in optical lattices 90
7.1 Background 90
7.2 Exact calculations 91
7.3 CPS representation of the Laughlin wave function 94
7.3.1 Ground state calculation 96
7.4 Results 97
7.5 Further work 102

8 Summary and conclusions 104
8.1 Summary of results 104
8.2 Future prospects 105

A Atomic transitions in ^{87}Rb 108

B The time-splitting spectral method 110
B.1 Stationary optical lattice 110
B.2 Rotating optical lattice 112

List of Figures

2.1 Schematic of the experimental arrangement surrounding the science cell . . . 11
2.2 False colour surface plots of absorption images taken in the yz-plane showing the cloud at different stages of evaporation . 13
2.3 Schematic of the experimental arrangement for generating the optical lattice . . . 17
2.4 False colour plots of *in situ* absorption images taken in the xy-plane for different lattice angles . . . 20
2.5 False colour plots of absorption images taken in the xy-plane at 20.5 ms time-of-flight, after an optical lattice has been flashed on for 50 μs . . . 23
2.6 Lattice depth as a function of the amplitude of the rf signal supplied from a given DDS chip . . . 24
2.7 Axial absorption image of atoms trapped in an optical lattice with spacing 4.6(1)μm . . . 25
2.8 Phase of the wave function after an optical lattice has been ramped up to 4 kHz in 40 ms for different hold times . . . 27
2.9 Overlap with the ground state and density, calculated for different ramp times for a 1.5 kHz and 4 kHz optical lattice . . . 28

3.1 Absorption image of atoms trapped in a two-dimensional optical lattice before and after the lattice spacing has been increased 33
3.2 Illustration of the relative speed of neighbouring lattice sites when the optical lattice is expanded. . . . 34
3.3 Effective trapping potential at the n^{th} lattice site in a reference frame accelerating at $n\ddot{d}$ . . . 34
3.4 Numerically calculated probability of finding a single particle in the ground state or a bound state of the $\cos^2(x)$ potential well after the spacing is increased . . . 35

4.1 Energy levels as a function of rotation frequency 41
4.2 Schematic illustrating different phases for atoms in an optical lattice in an artificial magnetic field 44
4.3 Hopping induced phases in the symmetric gauge for $\alpha = 1/2$. 45
4.4 Vortices in a rotating BEC after ramp down of the rotating optical lattice 47
4.5 Number of vortices as a function of rotation frequency, and minimum rotation frequency to nucleate a vortex, for various optical lattice depths 48
4.6 Simulations results for ramp up of the rotating optical lattice to $\Omega/2\pi = 10$ Hz 49
4.7 Simulation results for a lattice rotating at $\Omega/\omega \geq 1$ 51
4.8 Simulation results for a rotating lattice with $\alpha = 1$ 53
4.9 Simulation results for a rotating lattice with $\alpha = 1/3$ 54

5.1 Illustration of the area-law for entanglement scaling 63
5.2 Illustration of the CPS ansatz for a simple 2 by 2 system with open boundary conditions. 66
5.3 Illustration of the equivalence between matrix product states and correlator product states 68

6.1 Illustration of the different correlator types used to simulate the 2D Ising model 77
6.2 Bond correlators for $\Delta\mathbf{r}_{\max} = (2, 2)$ 78
6.3 Magnetisation as a function of transverse magnetic field for an $L \times L$ system, for the ground state found using 2×2 plaquette correlators 81
6.4 Absolute magnetisation at $B = 4$ for an $L \times L$ lattice 82
6.5 Absolute magnetisation as a function of transverse magnetic field for a 31×31 system, for the ground state found using different sized correlators 83
6.6 Transverse magnetisation as a function of transverse magnetic field for a 31×31 system, for the ground state found using different sized correlators 84
6.7 Two point correlation function at $B = 3.05$ for different correlator types 86
6.8 Difference in energy between ground state calculated using nearest-neighbour bond correlators and 4×4 plaquette correlators 87

6.9 Difference in two point correlation function between ground state calculated using nearest-neighbour bond correlators and 4×4 plaquette correlators 88

7.1 Overlap of the ground state in a disk with the Laughlin wave function as a function of average filling factor 93
7.2 Overlap of the ground state in a disk with the Laughlin wave function as a function of the number of the number of magnetic flux quanta per plaquette 94
7.3 Overlap of the ground state in a disk with the Laughlin wave function as a function of the on-site interaction energy 95
7.4 Density and correlation function of the Laughlin state for ten atoms in a 15×15 lattice 99
7.5 Energy minimisation, density and correlation function of a ten atom correlator product state at $\nu_{\text{eff}} = 1/2$ in a 15×15 lattice 101
7.6 Energy minimisation, density and correlation function of a ten atom correlator product state at $\nu_{\text{ave}} = 10$ in a 15×15 lattice 102

A.1 Hyperfine levels of the ground and first excited states in ^{87}Rb, and the transitions used for during the experimental sequence. 109

Chapter 1

Introduction

This thesis is concerned with using ultracold atoms in optical lattices to simulate condensed matter systems. In this chapter, the motivation for using ultracold atoms in optical lattices as quantum simulators is discussed, and then the various models used in this work are introduced, before an outline of the thesis is presented.

1.1 Background and motivation

Many interesting phenomena in condensed matter systems, such the fractional quantum Hall effect [1, 2] and high temperature superconductivity [3], occur as a result of strong interactions between particles. The very properties that make these systems interesting — the strong correlations — also means that it is extremely challenging to treat these systems theoretically, and there are still features of these systems that are not well understood.

It has been proposed that, although a classical computer cannot simulate these systems, a quantum computer can be programmed to simulate any local quantum system efficiently [4, 5]. There are two broad classes of quantum simulator [6]. The first of these comprises an array of qubits that encode the state of the quantum system, where its unitary evolution is described in terms of elementary quantum gates, and implemented in a circuit based quantum computer. The second of these is an 'analogue' quantum simulator, which is a system that obeys the same Hamiltonian as the system we are interesting in simulating, but can be more easily manipulated and probed. In this thesis, we will be concerned with this second type of quantum simulator.

Recent progress in the laser cooling of neutral atoms has led to these systems being ideal candidates for simulation of condensed matter physics. The

achievement of Bose Einstein condensation in 1995 [7, 8, 9] paved the way to experiments probing the coherence and superfluid properties of these macroscopic matter waves [10, 11, 12, 13]. The weakly-interacting BEC can be well-modelled using mean-field theory, and does not exhibit strong correlations. However the interactions can be tuned by using a Feshbach resonance [14, 15], or by loading the atoms into the tightly confined potential of an optical lattice.

In optical lattices, the periodic potential provided by a dipole trap acts to mimic the periodic potential experienced by electrons in a periodic array of ions in condensed matter systems. They provide clean periodic potentials with unprecedented control over the system parameters, and typically contain several thousand sites. For example, using optical lattices it is possible to control the dimensionality of the system, the lattice geometry, and the lattice depth. As we will see below, using optical lattices it is possible to model spin systems, or engineer artificial magnetic fields for neutral atoms. Furthermore such systems interact only weakly with their environment and thus benefit from long coherence times.

Using ultracold atoms in optical lattices to act as simulators for condensed matter systems was first proposed with respect to realising the superfluid-Mott insulator (MI) transition in Bose-Hubbard model [16], and evidence for the superfluid-MI transition with ultracold bosons was first observing experimentally in 2002 [17]. Fermions trapped in optical lattices have been used to realise the Mott and band-insulating states [18, 19]. There have been many proposals as to how optical lattices can be engineered so that they map onto Hamiltonians in condensed matter systems, and there has been rapid experimental progress [20, 21, 22].

Using optical lattices we can reach parameter regions that are not achievable in condensed matter systems (for example much larger magnetic fields), and these properties can allow us to map out the phase diagram of interesting systems. Modelling these systems using different species is also beneficial. For example, it has been predicted that in the bosonic analogue of fractional quantum Hall systems, the highly interesting non-Abelian states are more prominent than those in the conventional quantum Hall effect of a two-dimensional electron gas [23].

Another reason for simulating these systems using optical lattices are the different ways that the state of the system can be probed. Imaging these systems after some time-of-flight reveals the momentum distribution, or adiabatic band mapping techniques can be used to reveal the population in each band [24]. Recently demonstration of single atom imaging of atoms in a MI state has been achieved [25, 26]. Spatial correlations have also been investigated by measuring the noise correlations [27, 28].

In this thesis we investigate systems of bosonic atoms trapped in two dimensional optical lattice under the influence of an artificial magnetic field both experimentally in the Josephson-junction regime where there are many atoms per site, and theoretically in the strongly correlated regime. In addition, we will theoretically investigate the two-dimensional quantum Ising model in a transverse magnetic field. We also describe an experiment where atoms are trapped in a very deep optical lattice with dynamically variable periodicity. In sections 1.2 and 1.3 we will describe how these models are realised.

1.2 Ultracold atoms and optical lattices

1.2.1 Bose-Einstein condensation

Bose-Einstein condensates (BEC) are represented by a macroscopic wave function $\psi(\mathbf{r}, t)$, which obeys the time-dependent Gross-Pitaevskii equation (GPE) [29, 30]:

$$\mathrm{i}\hbar\frac{\partial\psi(\mathbf{r},t)}{\partial t} = \left[-\frac{\hbar^2}{2M}\nabla^2 + V(\mathbf{r},t) + gN|\psi(\mathbf{r},t)|^2\right]\psi(\mathbf{r},t), \tag{1.1}$$

where M is the atomic mass, N is the number of atoms and the interaction parameter $g = 4\pi\hbar^2 a_s/M$, a_s being the s-wave scattering length. This mean-field description of the weakly-interacting condensate has proven to be very successful, with theoretical predictions of the properties of these states showing remarkable agreement with those found experimentally [31, 32]. Realisation of strongly-interacting systems can be achieved by loading these dilute gases into deep periodic potentials.

1.2.2 Dipole trapping force

The optical dipole force originates from interaction of the electric dipole of the atom with the time-varying electric field of the light. It leads to a potential for atoms in the laser field of the form [33]

$$V_{\mathrm{dip}}(\mathbf{r}) = \frac{3\pi c^2}{2\omega_0^3}\frac{\Gamma}{\Delta}I(\mathbf{r}), \tag{1.2}$$

where $I(\mathbf{r})$ is the intensity profile of the laser field, and $\Delta \equiv \omega_L - \omega_0$ is the detuning of the laser field from atomic resonance. For red frequency-detuning ($\Delta < 0$) the potential minima coincide with the intensity maxima,

whereas for blue frequency-detuning ($\Delta > 0$) the potential minima coincide to the intensity minima. A periodic intensity profile arises from the interference of two counter-propagating beams, leading to a potential of the form $V_0 \cos^2(k_L x)$ with $k_L = \pi/d$, d being the lattice periodicity. Two and three dimensional lattices are built from standing waves in perpendicular directions, with different frequencies of the light to ensure that they do not interfere.

1.2.3 Model Hamiltonian in periodic potential

The Hamiltonian for atoms moving in the lattice potential (in second quantised form) is given by:

$$H = \int \mathrm{d}\mathbf{r} \left\{ \hat{\Psi}^\dagger \left[\frac{\mathbf{p}^2}{2M} + V_{\mathrm{ext}}(\mathbf{r}) + V_{\mathrm{latt}}(\mathbf{r}) + \frac{g}{2}\hat{\Psi}^\dagger\hat{\Psi} \right] \hat{\Psi} \right\}, \tag{1.3}$$

where $\hat{\Psi}$ is the field operator obeying bosonic commutation relations, $V_{\mathrm{ext}}(\mathbf{r})$ is an external trapping potential such as a harmonic trap, and $V_{\mathrm{latt}}(\mathbf{r})$ is the lattice potential given above.

In a periodic potential (considering one dimension and ignoring the external trapping potential for simplicity), according to Bloch's theorem, the single particle eigenstates have the form $\psi_q(x) = \mathrm{e}^{iqx} u_q(x)$ where $u_q(x)$ is a function that has the same periodicity as the underlying lattice, i.e. $u_q(x) = u_q(x + d)$, and q is the quasimomentum defined with a Brillouin zone $-\pi/d < q \leq \pi/d$ [34]. Substituting this ansatz into the Schrödinger equation, and taking the Fourier transform of $u_q(x) = \frac{1}{\sqrt{2\pi}} \sum_m c_{q,m} \mathrm{e}^{\mathrm{i}Gmx}$ and $V_{\mathrm{latt}} = \frac{V_0}{2} + \frac{V_0}{4}(\mathrm{e}^{\mathrm{i}Gx} + \mathrm{e}^{-\mathrm{i}Gx})$ leads to the following set of eigenvalue equations for each value of q

$$\left[\frac{\hbar^2}{2M}(q - mG)^2 + V_0 \right] c_{q,m} + \frac{V_0}{4}(c_{q,m+1} + c_{q,m-1}) = E_q c_{q,m}. \tag{1.4}$$

Solving this for each value of q determines the band structure $E_n(q)$, which are the eigenenergies for each value of q, with an eigenfunction given by the Fourier components $c^n_{q,m}$. Depending on the lattice parameters, this system can be modelled by various Hamiltonians. The most appropriate Hamiltonian to use depends on the following properties of the system [35]: (a) The number of atoms in the system; (b) The width of the lowest band; (c) The interaction energy; and (d) The band gap i.e. the gap between the ground state and the first excited state.

Weak potential

When the lattice potential is weak (i.e. less than the chemical potential of the cloud) and there are a large number of atoms, the field operator $\hat{\Psi}(\mathbf{r},t)$ can be expressed as a classical field $\psi(\mathbf{r},t)$, i.e. we assume a condensate ground state. The system can then be modelled by time dependent GPE of equation (1.1) with a periodic potential term. This can be solved numerically using well-known methods, such as the time-splitting spectral method described in Appendix B. This is the approach we use to model our experimental system in Chapters 2 and 4.

Tight-binding limit

In the tight-binding approximation, we model the wave function as a sum of well-localised wave functions on individual lattice sites. This approximation is valid when the band gap E_g is greater than the band-width and the interaction energy, and results in a cosinusoidal band-structure for the lowest band $E_0(q) = -2J_0\cos(qd)$. We can assume that the atoms occupy the lowest band if $k_BT \ll E_g$. We decompose the field operator as $\hat{\Psi}(\mathbf{r}) = \sum_i w_0(\mathbf{r}-\mathbf{r}_i)\hat{a}_i$, and where $\hat{a}_i$ is the bosonic annihilation operator for site i, and $w_0(r,r_i)$ is the Wannier state in the lowest band localised on site i, which is related to the Bloch states $\psi_q(x)$ by a Fourier transform [34]. Substituting this into equation 1.3, and neglecting long range terms, above leads to the Bose-Hubbard Hamiltonian

$$H = -J\sum_{\langle i,j\rangle}\hat{a}_i^\dagger\hat{a}_j + \text{h.c.} + \frac{U}{2}\sum_i \hat{a}_i^\dagger\hat{a}_i^\dagger\hat{a}_i\hat{a}_i, \tag{1.5}$$

where $\langle i,j\rangle$ denotes all nearest neighbour pairs, J is the tunnelling energy, and U is the on-site interaction energy given by $U = g\int|w_0(\mathbf{r}-\mathbf{r}_i)|^4\mathrm{d}\mathbf{r}$. The tunnelling energy J is related to the band structure by

$$J = \int w_0^*(\mathbf{r}-\mathbf{r}_i)\left[\frac{\mathbf{p}^2}{2M} + V_{\text{latt}}(\mathbf{r})\right]w_0(\mathbf{r}-\mathbf{r}_j)\mathrm{d}\mathbf{r} = \frac{1}{\nu_{\text{BZ}}}\int \mathrm{e}^{\mathrm{i}\mathbf{q}\cdot(\mathbf{r}_i-\mathbf{r}_j)}E_0(\mathbf{q})\mathrm{d}\mathbf{q}, \tag{1.6}$$

which is J_0 for all i,j separated by a single lattice site (where ν_{BZ} is the volume of a Brillouin zone).

When there are hundreds of atoms per lattice site, we can replace the annihilation operator by a $\hat{a}_i = \sqrt{N_i}\exp^{\mathrm{i}\hat{\theta}_i}$, resulting in the following Hamiltonian

$$H = -\sum_{\langle i,j\rangle}E_{J_{(ij)}}\cos(\theta_i-\theta_j). \tag{1.7}$$

where $E_{J_{(ij)}} = 2\sqrt{n_i n_j}$, and we have assumed $U \ll E_{J_{(ij)}}$ so that the interaction term can be neglected. This is known as the XY model that describes Josephson-junction arrays — a regular network of superconducting islands weakly coupled by tunnel junctions.

Note that in the weakly-interacting limit with hundreds of atoms per lattice site, it is still possible to describe the system using the time-dependent GPE (1.1). This is the approach we use for our numerical calculations in the mean-field regime since we wish to use a model that describes the properties of the system in both the weak potential and deep potential limit. Note that the discrete non-linear Schrödinger equation (DNLSE) can also be used in this regime [36, 37, 38] (however we do not take this approach in this thesis).

Isolated condensates

The simplest system we can consider is one in which the lattice potential is so deep that tunnelling between the lattice sites is negligible on typical experiment time scales. In this case we treat each potential minima as a separate system. If we ignore interactions we can simply work out the single particle ground state at each lattice site, and this is the procedure we follow in Chapter 3. Alternatively, to include interactions each lattice site can be treated separately using the GPE (1.1).

1.3 Quantum simulation

Optical lattice potentials are highly tuneable, and quantum simulation experiments can explore the different phases of these models by varying system parameters. The first demonstration of this was varying the lattice depth V_0 to control the ratio U/J in the Bose-Hubbard model (1.5), and so observe the quantum phase transition from a superfluid to Mott insulator [17]. Here, we introduce the model Hamiltonians that will be used in this thesis.

1.3.1 Artificial magnetic fields

Some of the more exotic phenomena in condensed matter systems occur when there is a magnetic field present, such as the quantum Hall effect. Artificial magnetic fields for neutral atoms can be generated using a variety of methods in cold atom systems, which will be described in section 4.1.1. One method is to rotate the optical lattice: this can be seen simply by considering the form of the Lorentz force $F = -e(\mathbf{v} \times \mathbf{B})$, which has the same form as the Coriolis force $F = 2m(\mathbf{v} \times \mathbf{\Omega})$ in a frame corotating with the lattice.

The Hamiltonian for atoms in an artificial magnetic field is given by

$$H = \int \mathrm{d}\mathbf{r} \left\{ \hat{\Psi}^\dagger \left[\frac{1}{2M}(\mathbf{p} - M\mathbf{A})^2 + \frac{1}{2}M\omega_{\mathrm{eff}}^2 r^2 + V_{\mathrm{latt}}(\mathbf{r}) + \frac{g}{2}\hat{\Psi}^\dagger\hat{\Psi} \right] \hat{\Psi} \right\}, \quad (1.8)$$

where $\mathbf{A}$ is the magnetic vector potential. In this thesis, we study optical lattices in artificial magnetic field in two parameter regimes: experimentally in the Josephson-junction regime, and numerically in the fractional quantum Hall regime.

To arrive at the Hamiltonian in the tight-binding regime, we make the Peierls substitution [39, 40, 41]. This consists of replacing the momentum term $\mathbf{q}$ in the band structure $E_0(\mathbf{q}) = -2J_0[\cos(q_x d) + \cos(q_y d)]$ with the covariant momentum $(\mathbf{p} - M\mathbf{A})$ and treating it as the effective Hamiltonian. Calculation of the tunnelling matrix elements as given in equation (1.6) leads to the following Bose-Hubbard Hamiltonian:

$$H = -J \sum_{\langle i,j \rangle} \mathrm{e}^{\mathrm{i}\phi_{ij}} \hat{a}_i^\dagger \hat{a}_j + \mathrm{h.c.} + \frac{U}{2} \sum_i \hat{a}_i^\dagger \hat{a}_i^\dagger \hat{a}_i \hat{a}_i + \sum_i \varepsilon_i \hat{a}_i^\dagger \hat{a}_i, \quad (1.9)$$

where $\phi_{ij} = (M/\hbar) \int_i^j \mathbf{A} \cdot \mathrm{d}\mathbf{r}$. Equation (1.9) differs from the Bose-Hubbard Hamiltonian in a static lattice by means of phases on the hopping terms. The total magnetic flux through a plaquette α that can be reached using artificial magnetic fields can be ~ 1, which is not possible in condensed matter systems due to the small plaquette size. Thus cold atoms can be used to investigate the interesting effects that occur in these regimes.

1.3.2 Spin models

Spin exchange interaction

A variety of spin models can be realised by using the spin exchange interaction for spinor bosons or fermions in an optical lattice [42, 43, 44]. We consider atoms having two internal spin states $\sigma = \uparrow, \downarrow$, where the two spin states are trapped in independent lattices, so that the lattice parameters for each spin state can be independently controlled. The Hamiltonian in the tight-binding limit is

$$H = -\sum_{\langle i,j \rangle, \sigma} (J_\sigma \hat{a}_{i\sigma}^\dagger \hat{a}_{j\sigma} + h.c.) + \frac{1}{2} \sum_{i,\sigma} U_\sigma \hat{n}_{i\sigma}(\hat{n}_{i\sigma} - 1) + U_{\uparrow\downarrow} \sum_i \hat{n}_{i\uparrow}\hat{n}_{i\downarrow}. \quad (1.10)$$

In the regime where $J_\sigma \ll U_\sigma, U_{\uparrow\downarrow}$ and $\langle \hat{n}_{i\uparrow}\rangle + \langle \hat{n}_{i\downarrow}\rangle = 1$, this can be expressed as a spin Hamiltonian:

$$H = \sum_{\langle i,j\rangle} [\lambda_z \sigma_z^{[i]} \sigma_z^{[j]} - \lambda_\perp (\sigma_x^{[i]} \sigma_x^{[j]} + \sigma_y^{[i]} \sigma_y^{[j]})], \tag{1.11}$$

with $\sigma_z^{[i]} = \hat{n}_{i\uparrow} - \hat{n}_{i\downarrow}$, $\sigma_x^{[i]} = \hat{a}_{i\uparrow}^\dagger \hat{a}_{j\downarrow} + \hat{a}_{i\downarrow}^\dagger \hat{a}_{j\uparrow}$ and $\sigma_y^{[i]} = -\mathrm{i}(\hat{a}_{i\uparrow}^\dagger \hat{a}_{j\downarrow} - \hat{a}_{i\downarrow}^\dagger \hat{a}_{j\uparrow})$, and where the '-' is replaced by a '+' for fermions. This is the anisotropic Heisenberg model (the XXZ model). The parameters $\lambda_{z,\perp}$ are given by $\lambda_z = (J_\uparrow^2 + J_\downarrow^2)/2U_{\uparrow\downarrow} - J_\uparrow^2/U_\uparrow - J_\downarrow^2/U_\downarrow$ and $\lambda_\perp = J_\uparrow J_\downarrow / U_{\uparrow\downarrow}$, so it can be seen that the model can be tuned by varying the relative lattice depths of the two state-dependent lattices, thus changing the magnitude of U_σ/J_σ or through using a Feshbach resonance [14, 15]. The Ising model is realised if $J_\downarrow$ becomes negligible while $J_\uparrow$ remains finite, while the isotropic Heisenberg model is realised for equal tunnelling and interaction energies. The energy scales as J^2/U, which is a few nanokelvin for typical experimental parameters.

Mapping to hard core boson model

Spin models can also be realised by mapping onto the hardcore boson model (i.e. where for a sufficiently large on-site interaction energy we can assume that there is a maximum of one atom allowed on each site). In this case, the Fock states $|0\rangle_i, |1\rangle_i$ map to spin states $|\uparrow\rangle_i, |\downarrow\rangle_i$. The bosonic creation and annihilation operators $\hat{a}_i, \hat{a}_i^\dagger$ are mapped onto the spin-1/2 operators as $\sigma_x^{[i]} = \hat{a}_i + \hat{a}_i^\dagger$, $\sigma_y^{[i]} = -\mathrm{i}(\hat{a}_i - \hat{a}_i^\dagger)$ and $\sigma_z^{[i]} = 1 - 2\hat{a}_i^\dagger \hat{a}_i$ [45]. This transforms the Hamiltonian to

$$H = -\frac{J}{2} \sum_{\langle i,j\rangle} \sigma_x^{[i]} \sigma_x^{[j]} + \sigma_y^{[i]} \sigma_y^{[j]}. \tag{1.12}$$

Unlike with the spin exchange interaction above, the energy scales are of order J and thus it is easier to model this system experimentally.

1.4 Thesis overview

This thesis describes both experimental work and theoretical work related to quantum simulation of two-dimensional condensed matter systems.

In Chapter 2, the experimental arrangement used to produce a BEC of ^{87}Rb and provide a flexible two-dimensional optical lattice potential is described. Calibration of the optical lattice parameters and adiabaticity of

loading atoms into the optical lattice are discussed. The optical lattice periodicity can be varied dynamically to provide an 'accordion' lattice, and experiments with ultracold atoms trapped in an accordion lattice are described in Chapter 3. In these experiments the atoms remain bound whilst the spacing of the lattice is increased in both directions from 2.2 to 5.5 μm in a few milliseconds. This technique allows a quantum simulation experiment to be performed with a lattice spacing smaller than the resolution limit of the imaging system, while allowing imaging of the atoms at individual lattice sites by subsequent expansion of the optical lattice.

Chapter 4 is concerned with artificial magnetic fields, and an overview of methods to generate artificial magnetic fields is given. The optical lattice described in Chapter 2 can also be rotated, which results in an artificial magnetic field. With many atoms per lattice site the system is analogous to a Josephson-junction array, and previous experiments carried out in this regime are summarised, and compared with simulations carried out by solving the time-dependent GPE for our experimental parameters. Other phases that arise for atoms in optical lattices subject to artificial magnetic fields, and the steps that would be required to reach the strongly correlated regime, are then discussed.

Chapters 5 to 7 are concerned with efficient numerical techniques for describing strongly correlated two-dimensional systems. Such calculations are important for improving our understanding of these systems, and for determining the parameters required to reach these regimes in an experiment. In Chapter 5 the tensor network description of states and the correlator product state representation are introduced. Estimation of expectation values using Monte Carlo sampling and determining the ground state using stochastic minimisation are described. In Chapter 6 these techniques are applied to the two-dimensional quantum Ising model in a transverse magnetic field. It is demonstrated that large system sizes can be reached using this description, and the degree to which long-range correlations can be described are compared for different correlator types. In Chapter 7 we apply the correlator product state method to the two-dimensional Bose-Hubbard model in a magnetic field in the regime in which fractional quantum Hall physics is predicted to occur. Exact diagonalisation calculations for small systems in a disk geometry are first described, and these are then compared with results found using correlator product states. Preliminary results for larger systems are also presented.

A summary of the thesis is given in Chapter 8, and future directions for both experimental and theoretical work are discussed.

Chapter 2

Experimental arrangement

This chapter describes the arrangement used to perform experiments with a BEC of ^{87}Rb in a dynamic optical lattice. The BEC-producing parts of the apparatus built before my arrival are described in detail in earlier theses from the group [46, 47, 48], so only an overview of experimental sequence is described below. For a schematic of the atomic transitions used to cool and image the atoms, see appendix A.

2.1 Producing a BEC

Figure 2.1 shows the experimental arrangement used to produce a BEC in our lab, illustrating the paths of the various beams used to cool and trap the atoms, and the positions of the magnetic coils.

The vacuum system is made up of two sections at different pressures:

- The pyramid chamber has a background pressure of approximately 10^{-9} mbar, and contains the rubidium source (SAES getters) for the initial loading;
- The science cell, which is kept at ultra-high vacuum. This is the region in which we trap atoms in the magnetic trap for evaporating to BEC and loading into the optical lattice.

Cold atoms are loaded into the magnetic trap using a double magneto-optical trap (MOT) system [49]. The atoms released from heated getter sources create a vapour pressure of rubidium in the pyramid chamber. Using a pyramid MOT [50, 51] provides a simple way to provide the initial loading

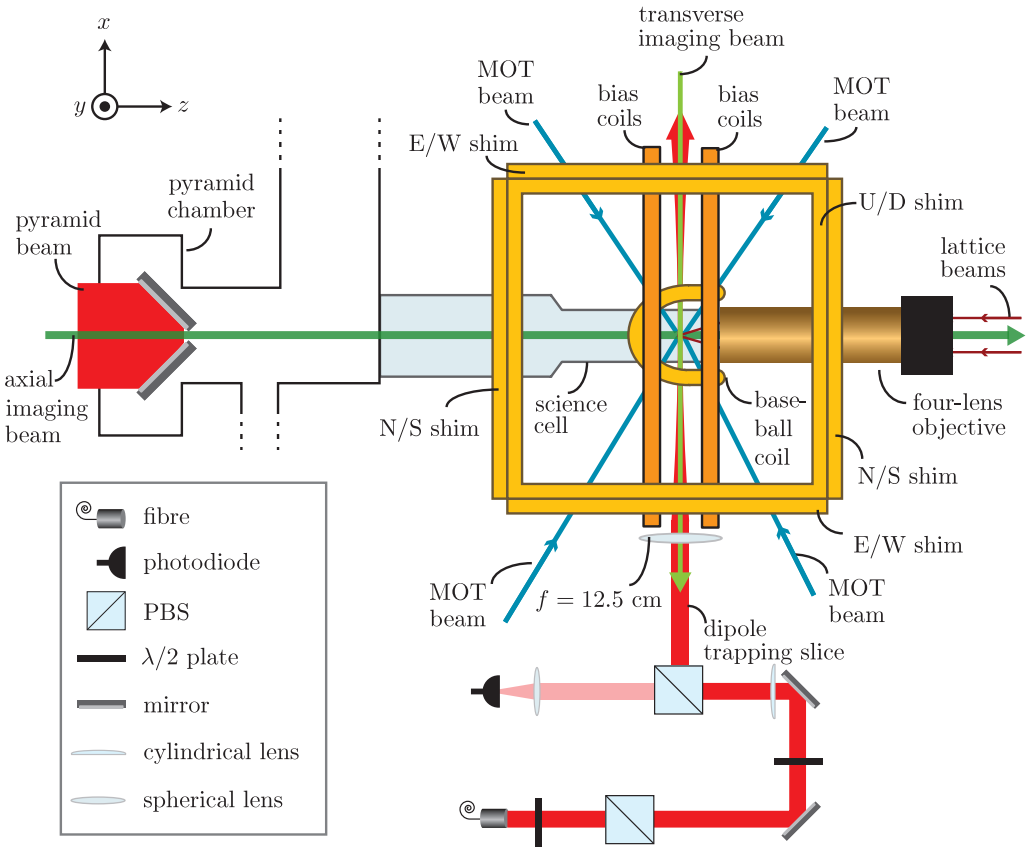

Figure 2.1: Schematic showing a plan of the experimental arrangement surrounding the science cell. The figure shows only the main parts of the apparatus and the beam paths incident on the atoms. The y-axis is the vertical axis.

since the six MOT beams are generated from a single beam by means of the four pyramid mirrors. A flux of cold atoms is directed into the science cell through a 1×2 mm slit at the vertex of the pyramid. Here the atoms are captured by a conventional six-beam MOT. Figure 2.1 shows the position of the four horizontal MOT beams (there are two additional vertical MOT beams that are not shown). We are able to capture up to 3×10^8 atoms in one minute in our six-beam MOT.

After the initial MOT loading stage the atoms are prepared for optimal loading into the magnetic trap by a compressed MOT stage to increase the phase space density of the cloud. This is done by increasing the quadrupole field gradient and the detuning. Then the optical molasses technique is used to cool the atoms to around 40 μK. The cold atoms are optically pumped

into the $F = 1, m_F = -1$ hyperfine level for magnetic trapping, using a laser beam which follows the path of the transverse imaging beam (shown in Figure 2.1).

The atoms are cooled to quantum degeneracy using radio-frequency (rf) evaporative cooling in an Ioffe-Pritchard type magnetic trap provided by the baseball coil and the bias coils. The magnetic trap gives strong trapping in the xy (radial) plane and weak trapping in the z (axial) direction leading to a cigar shaped cloud. We perform initial evaporation in 90 seconds in the 'tight' magnetic trap with parameters $\omega_r = 2\pi \times 167$ Hz, $\omega_z = 2\pi \times 5.4$ Hz. The tight magnetic trap is best for evaporative cooling because of the high collision rate and minimal (10 μm) gravitational sag. However for performing experiments in the optical lattice we relax to the 'weak' trap with $\omega_r = 2\pi \times 20$ Hz, $\omega_z = 2\pi \times 4.6$ Hz (for reasons explained in the following section). We complete the evaporative cooling in the weak trap, which although less efficient, has the advantage of damping any slosh generated by relaxation of the trap. After 30 seconds of evaporation we obtain a BEC of around 500,000 atoms, although we usually continue evaporation until there is no discernible thermal component. We typically work with a BEC of between 100,000 and 200,000 atoms, where we choose the optimal cloud size for a given experiment. Figure 2.2 shows the cloud at different stages of evaporation, illustrating the transition from a thermal cloud to a BEC.

2.2 Moving to a pancake-shaped geometry

The cigar-shaped dimensions of the final BEC are not optimal for loading into our 2D optical lattice. The radius of a 100,000 atom cloud in this trap is only 9.1 μm, and this would not result in a large number of filled lattice sites. Also the low axial trapping frequency means that there is only a small energy barrier to exciting higher vibrational levels in the axial direction, and the large axial extent (40 μm) makes imaging in the radial plane challenging. For these reasons, the next step in the sequence is to change the geometry of the trap to result in a pancake-shaped BEC. We achieve this by increasing the axial trapping frequency using an optical dipole trap.

The optical dipole trap is formed using a single slice of light with a red frequency detuning. The laser set-up for the dipole trapping sheet (not shown) consists of a tapered amplifier (Eagleyard TPA-850-1W) seeded with broadband light from a multi-mode diode (Roithner QL86T4HD) operating at 865 nm with a line width of 3 nm.[1] This large line width results in laser light

[1]The beam profile of the light from the multi-mode diode is very poor, and to obtain an optimal beam for seeding the tapered amplifier we first pass the beam through a single-

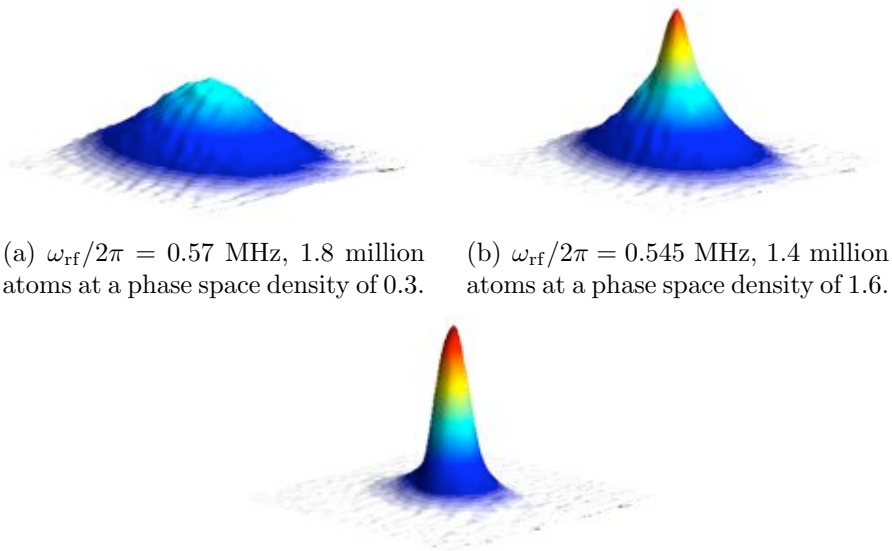

(a) $\omega_{\rm rf}/2\pi = 0.57$ MHz, 1.8 million atoms at a phase space density of 0.3.

(b) $\omega_{\rm rf}/2\pi = 0.545$ MHz, 1.4 million atoms at a phase space density of 1.6.

(c) $\omega_{\rm rf}/2\pi = 0.505$ MHz, 500,000 atoms at a phase space density of 35.

Figure 2.2: False colour surface plots of absorption images taken in the yz-plane showing the cloud at different stages of evaporation, with ω_{rf} the final rf frequency. In these images, all the evaporation is carried out in the tight trap, and the clouds are imaged at 28 ms time-of-flight. The field of view of each image is 1.12×1.12 mm.

with a coherence length of order 100 μm, which cuts down any interference that would occur on length scales larger than this. Crucially, the coherence length is smaller than the thickness of the quartz science cell (2 mm), thus there is no interference caused by multiple reflections between the cell walls. We have found that using broadband light significantly improves the beam profile of the trapping slice, and improves the lifetime of the condensate if the atoms are moving in the trap (e.g. if they are rotating), as well as reducing the damping rate of such movement. The resulting light beam is passed to the vacuum system optical table through a single-mode optical fibre. The optics used to form the slice are shown in Figure 2.1. The vertical slice is formed by passing the spherically symmetric beam output from the fibre through a telescope formed by a 15 cm cylindrical lens and a 12.5 cm circular lens. The $1/e^2$ waists of the beam at the centre of the magnetic trap are $w_y = 1.30(1)$ mm and $w_z = 22.5(3)$ μm, and the maximum power we can attain is around 200 mW. The beam power is controlled using a PID

mode fibre. Coupling into the fibre is achieved with only $\sim 5\%$ efficiency, but the 26 mW that results is adequate for our purposes.

intensity servo, using a photodiode to monitor the power of a pick-off beam transmitted through a polarising beam splitting cube (PBS).

The dipole trapping slice yields a potential of the form

$$V(x,y,z) = -\frac{V_0}{\zeta_y(x)\zeta_z(x)} \exp\left(-\frac{2y^2}{w_y^2\zeta_y^2(x)} - \frac{2z^2}{\zeta_z^2(x)w_z^2}\right), \tag{2.1}$$

where $\zeta_{y(z)}(x) = \sqrt{1 + x^2\lambda^2/\pi w_{y(z)}^4}$ with λ the wavelength of the trapping light. This can be approximated as a harmonic trap with $\overline{\omega}_{y(z)} = \sqrt{4V_0/Mw_{y(z)}^2}$ and $\overline{\omega}_x = \sqrt{V_0\lambda^2/\pi M w_{(z)}^4}$ close to the centre of the trap.

We calibrate the axial trapping frequency as a function of control voltage by giving the cloud a small kick and observing the frequency of oscillations in time-of-flight. The maximum power corresponds to a trapping frequency of $\overline{\omega}_z = 2\pi \times 180$ Hz. At this power, the scattering rate $\Gamma_{\text{scatt}} = 40$ ms^{-1}, equivalent to a heating rate of 4 nK/s, and thus it is not desirable to use such a deep trap for more than a second. However, since $\overline{\omega}_z^2$ scales with $\sqrt{P}$, P being the optical power, we are still able to work at trap frequencies of around $\overline{\omega}_z = 2\pi \times 50$ Hz with negligible heating for a few seconds. For $\overline{\omega}_z = 2\pi \times 100$ Hz, a 100,000 atom cloud has a radius of 16.8 μm in the xy-plane, and an axial radius of 3.4 μm.

The trapping frequencies along the radial directions when $\overline{\omega}_z = 2\pi \times 100$ Hz are $\{\overline{\omega}_x, \overline{\omega}_y\} = 2\pi \times \{3.4, 1.7\}$ Hz, which when added in quadrature to the magnetic radial trapping frequency, changes the overall frequencies by 0.1 Hz and 0.3 Hz respectively.

2.3 Imaging

We have the ability to image in two directions: in the yz-plane (transverse imaging) and in the xy-plane (axial imaging). To image the atoms in both cases, we use conventional absorption imaging. We first optically pump the atoms to the F = 2 level by illuminating them with repumper light (see appendix A) along all the MOT beam paths. We then image the atoms by illuminating the atoms by a collimated beam of light resonant with the $5S_{1/2}$ $F = 2$ – $5P_{3/2}$ $F' = 3$ transition. The light is absorbed by the atoms, and it is the shadow in the probe beam that is imaged. The intensity of a probe beam propagating along z varies as $I = I_0 \mathrm{e}^{-O(x,y)}$, where $O(x,y)$ is

the optical density, which on resonance is given by

$$O(x,y) = \frac{\sigma_0}{1 + I/I_{\text{sat}}} \int n(x,y,z)\mathrm{d}z \tag{2.2}$$

where σ_0 is the absorption cross section and $n(x,y,z)$ is the density of the cloud. In our experiment the measured value of the optical density saturates at ~ 3, due to small parts of the probe beam that cannot be observed (i.e. off-resonant, incorrectly polarised, or scattered light). It is therefore important to ensure that $O(x,y) < 3$. This is usually satisfied when imaging at a long time-of-flight, however for imaging *in situ* the optical density is ~ 100. When imaging *in situ* we only repump a fraction of the atoms, either by repumping only a thin slice of the condensate, or by detuning the repumper light. Doing this means that there are fewer atoms that interact with the probe beam, thus reducing the optical density. The same Andor CCD camera is used for both types of imaging, with flipping mirrors used to switch between the two imaging methods. The arrangement of the imaging beams is illustrated in Figure 2.1.

For transverse imaging, the light is first incident on a 12.5 cm lens, and the image is brought at the camera using a 25 cm lens. The images have a magnification of 2, and the field of view in the object plane is around 4 mm across, allowing a large variation of the time-of-flight to be viewed in this plane without adjustment of the beam path. Transverse imaging is used for imaging the atom cloud at a long time-of-flight (typically up to 30 ms). A small bias field to define a quantisation axis is provided by the E/W shim coils, and the probe light is polarised to drive the $\sigma^+ m_F = 2$ to $m_{F'} = 3$ transition. For transverse imaging we use a probe pulse duration of 200 μs, and the images in Figure 2.2 are taken with $I/I_{\text{sat}} = 1$.

To image in the plane of the lattice and at high resolution, we use axial imaging. The objective lens [52] is a compound four-lens arrangement, made according to the design described in [53]. The four-lens objective is designed to give diffraction-limited performance at a large working distance, and to correct spherical aberrations introduced by the cell window through which the cloud is observed. It is also designed give a good performance at both 780 nm for imaging, and at 830 nm for forming the optical lattice (described below). The numerical aperture (NA) of the lens is 0.27, and it has a working distance of 37 mm. The theoretical maximum resolution of the axial imaging system is $d_{\text{res}} = 0.61\lambda/\text{NA} = 1.8$ μm, however the depth of field of the imaging system is $\lambda/\text{NA}^2 = 10$ μm. This limits the minimum structure size we can resolve, since the axial extent of the cloud is usually comparable with this.

The image is brought to a focus on the same Andor camera using a 75 cm lens, and the magnification is 18.7,[2] with a field of view of around 440 μm. When imaging *in situ* in the weak trap, there is a large magnetic field along the z-direction of 66 G that defines the quantisation axis. This shifts the probe transition frequency by 92 MHz, so the probe light is frequency shifted (using an additional acousto-optic modulator (AOM)) for *in situ* imaging. We use $I/I_{\mathrm{sat}} = 0.75$,[3] and a probe pulse of 50 μs or less. We find that a longer probe pulse causes blurring of the atoms due to movement during imaging.

2.4 Optical lattice

The optical lattice is generated using acousto-optic deflectors and an optical interferometer that has been previously reported in [48, 54]. This arrangement is extremely flexible and allows smooth variation of the optical potential as we have demonstrated for a rotating optical lattice [55], and a lattice with dynamically varying periodicity (an 'accordion' lattice) as described in Chapter 3.

2.4.1 Optical lattice arrangement

The arrangement used to generate the optical lattice used in these experiments is shown in Figure 2.3. The light for the optical lattice is provided by a Ti:sapphire laser (Coherent MBR-110) operating at 830 nm. The laser is positioned on a separate optical table (not shown), and the light passes through a single-mode fibre giving a beam with a $1/e^2$ radius of 2.8 mm. A small portion of the beam is picked off and sent to a photodiode for monitoring the beam power. The beam power is controlled by the attenuation of an AOM on the same optical table as the Ti:Sapphire laser, and a PID controller. This keeps the beam power stable with variations of less than 1%.

Acousto-optic deflection of beams

The laser beam at 830 nm is then split into two beams of equal power at a PBS to provide the light for each of the two orthogonal lattices. Each

[2]The magnification of the imaging system is found conventionally by monitoring the distance a cloud falls in time-of-flight.

[3]We do not have much flexibility over this value, since we are limited in the beam size by the requirement that the imaging passes through the vertex of the pyramid chamber, and also limited in the beam power by the requirement that we have sufficient counts at the camera.

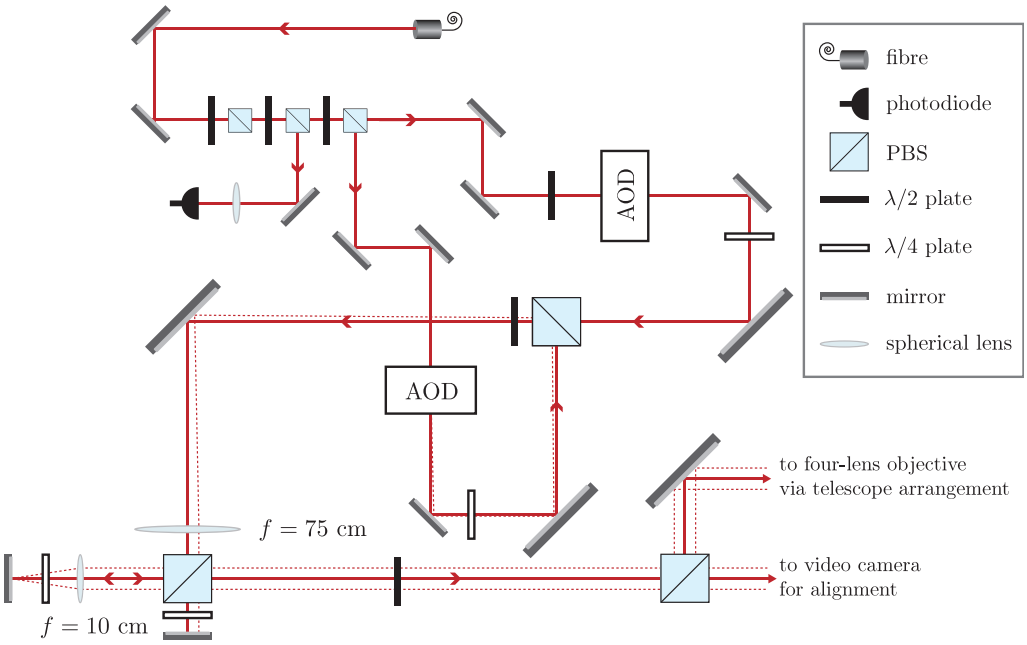

Figure 2.3: Schematic showing a plan of the experimental arrangement for generating the optical lattice. The sold line shows the optical axis of the arrangement, while the dashed line shows a beam displaced from the optical axis in the x-direction by an acousto-optic deflector (AOD).

beam being sent to its respective acousto-optic deflector (AOD), which is a dual axis Isomet LS110A-830XY comprising two crystals oriented at 90° to provide deflection in two directions. The rf signal used to control the beam deflection is provided by a custom built Direct Digital Synthesis (DDS) system, described in [47], which we operate with a frequency resolution of 1 Hz,[4] and a frequency update rate of 10 MHz. The DDS system has four chips (which will be referred to as X_1 to X_4), three of which are used for control of the optical lattice: X_1 controls the x deflection of the first lattice; X_2 controls both the x deflection of the first lattice and the y deflection of the second lattice; and X_4 controls the x deflection of the second lattice. (The remaining chip, X_3, was used to provide an rf signal for evaporation in later parts of the experimental sequence). Control of the DDS signal is provided by a LabView program, allowing flexible and easily programmable control of the beam deflection. In addition to controlling the deflection of the beams, the DDS system also allows control of the power of the rf signal, giving us

[4]It is possible to reach a frequency resolution of 1 μHz if all 48 bits of frequency resolution are used.

another means for varying the depth of the optical lattice.

The centre frequencies of the AODs (which define the optical axis) are displaced from one another by 10 MHz, while the maximum amplitude used is 3.8 MHz, ensuring that there is always a detuning of a few MHz between the beams to prevent interference. This maximum amplitude corresponds to a deflection of 0.3° from the optical axis. The deflected beams are recombined at a PBS after being passed through a quarter-wave plate to ensure maximum transmission/reflection as required (since the beam is circularly polarised after the AOD). At a distance of 75 cm from both AODs, the beams are passed through a 75 cm lens, which produces a beam parallel to the optical axis and displaced by an amount proportional to the deflection angle (for the small angles that we deal with).

Interferometer arrangement

The deflected beam from each AOD then passes through the interferometer optics: the short arm of the interferometer simply reflects the beam, while the long arm of the interferometer includes a 10 cm lens arranged as a $4f$ optical imaging system, which deflects the beam to the opposite side of the optical axis while leaving the characteristics of the beam profile unchanged. The quarter-wave plate in both arms ensures that no power is lost. The final result is a beam pair (from each AOD) that are always deflected by the same distance, but in opposite directions, from the optical axis. Directly after the interferometer the beam pairs will have perpendicular polarisations. The following half-wave plate (which rotates the polarisation through 45°) and PBS ensure that the beam pair will have the same linear polarisation. A final quarter wave-plate (not shown) is used to give all the beams the same circular polarisation.[5]

Optical lattice alignment

Note that half the power is lost at the final PBS, and unfortunately there is no way to avoid this (using non-polarising beam splitting cubes would simply result in the same power loss at the interferometer). The transmitted beam is used as a tool for aligning the lattice beams, and an infra-red video camera is positioned for this purpose. Careful alignment of the beams is necessary to ensure that the centres of the two lattices are the same, and that the lattice spacing does not change while the lattices are rotated. The alignment routine we used is described in detail in [48]. Briefly, we monitor the positions of

[5]This ensures that the electric field component in the plane of the interference fringes remains constant as the lattice rotates.

the beams as the deflection angle is rotated. For correctly aligned beams, the positions of the beam pairs should coincide when the deflection angle is rotated 180° degrees, and a fast switching of the beam position indicates if this condition is satisfied. The alignment of the optical lattice is monitored every day, and a small adjustment of the first 75 cm lens or of the beam path of the AOD is required every few days to maintain optimum alignment. This procedure can keep good alignment for several weeks, after which realignment of the whole system from the AODs onwards is carried out.

Path to atoms

After the final beam splitting cube, the optical lattice could be created by simply bringing the beams to a focus at the atoms using the four-lens objective. However, in our set-up, for practical reasons, there are a few metres between the science cell and the interferometer. In addition, the beam waist and displacement produced for a given rf frequency are not optimal for our experimental parameters. For these reasons the beam is passed through a number of telescopes before it reaches the four-lens objective. A 1:1 telescope maps the beam parameters to a further position along the optical bench, while a 1:2 telescope halves the beam waist at the atoms (increasing the lattice depth for a given power), and doubles the beam displacement from the optical axis for a given rf frequency.[6] The beam displacement in the back focal plane of the four lens objective is related to the rf displacement $\Delta\nu_{x(y)}$ by $\mathrm{D} \propto (\Delta\nu_x, \Delta\nu_y)$ for small angles.

The optical lattice is formed in the focal plane of the four-lens objective, which is arranged to be at the same position as the centre of the weak magnetic trap. Each beam pair produces interference fringes with an intensity distribution of the form

$$I = I_0 \mathrm{e}^{-2(x^2+y^2)/w^2} \times \left[2 + \cos\left(\frac{2\pi}{d}(x\cos\theta + y\sin\theta)\right) + \cos\left(\frac{2\pi}{d}(y\cos\theta - x\sin\theta)\right)\right], \tag{2.3}$$

where I_0 is the peak intensity, $w = 69$ μm is the beam waist, θ is the orientation angle of the lattice with respect to the horizontal direction given by $\tan\theta = \Delta\nu_x/\Delta\nu_y$. The distance between intensity maxima d, which is the optical lattice spacing, is given by $d = f\lambda/D \propto 1/\sqrt{((\Delta\nu_x)^2 + (\Delta\nu_y)^2}$. In this way both the angle of orientation of the lattice and the lattice spacing

[6] This is preferable since the diffraction efficiency decreases with increasing displacement.

can be varied dynamically by changing the frequency of the rf signals applied to the AODs.

The minimum lattice spacing is constrained by the NA of the objective lens to $d_{\min} = \lambda/2(\mathrm{NA}) = 1.53\ \mu$m, although in our experimental sequences we keep to a lattice spacing of above 2.2 μm to be sure that no clipping of the lattice beams occurs.

Alignment onto atoms

As well as ensuring the lattice optics are well aligned, it is important to ensure that the optical lattice is well aligned with the centre of the magnetic trap. This is more critical for rotation where a mismatch of a few microns can lead to a lot of heating. It is also important for the accordion lattice (see Chapter 3), as if the centre of expansion of the lattice is far from the centre of the magnetic trap the velocity of the atoms on the outside of the cloud will be larger, causing more heating.

The initial alignment of the optical lattice is carried out using two mirrors placed before the four-lens objective. The alignment of the optical lattice drifts by a few microns over a timescale of a few days, and small adjustments of the relative alignment of the magnetic trap and optical lattice are made by varying the current in the E/W and U/D shim coils. We monitor the position of the centre of the lattice by looking at the position of a rotated cloud at different points during a period of rotation.

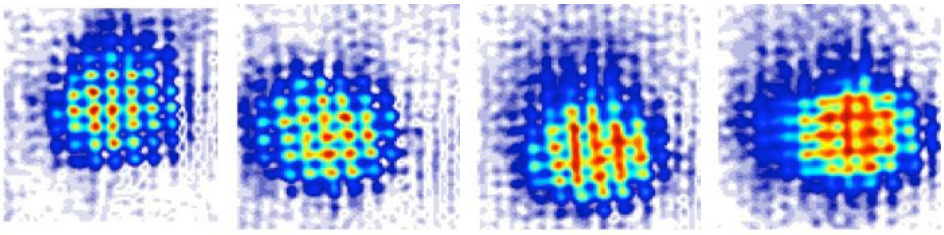

Figure 2.4: False colour plots of *in situ* absorption images taken in the xy-plane. An optical lattice with $V_0 = h \times 8.5$ kHz and $d = 7.5\ \mu$m is ramped on, and then rotated at a frequency of 5 Hz. Shots are taken every quarter of a rotation period. In these shots the atoms trace out a circle with radius 8 μm, which gives the offset between the centre of the optical lattice and the centre of the magnetic trap.

Figure 2.4 shows an example of these images taken *in situ*, but this technique can also be used in time-of-flight. For monitoring the position *in situ*, the position of the cloud is monitored while atoms are trapped in a rotating optical lattice. For monitoring the position in time-of-flight, the optical

lattice is first ramped down while it is rotating, and the cloud imaged after different hold times in the magnetic trap. The accuracy to which we can align the optical lattice is limited by the accuracy to which we can determine the centre of the magnetic trap, which is around ± 2 μm.

2.4.2 Characterisation of the optical lattice

Lattice depth

We can estimate the lattice depth V_0 from the optical power using [33]

$$V_0 = \frac{\pi c^2}{2}\left(\frac{2\Gamma_2}{\Delta_2\omega_2^3} + \frac{\Gamma_1}{\Delta_1\omega_1^3}\right)\frac{8P}{\pi w^2}, \tag{2.4}$$

where P is the power of one of the beam pairs, $\Gamma_{1,2}$ is the natural line width of the $D_{1,2}$ transition, $\omega_{1,2}$ is the frequency of each transition and $\Delta_{1,2}$ is the detuning of the trapping light from each transition (and where for this rough estimate we have ignored the contribution from the ground state hyperfine splitting). This gives an initial estimate for the lattice depth as a function of beam power as 7.6 kHz/mW for our parameters. However, it is more accurate to measure the beam depth directly, since determining the beam characteristics accurately is difficult. For example, the lattice depth is likely to be smaller than the calculated value due to losses at the science cell, and imperfect beam balance. Measuring the lattice depth can be done in a variety of ways, e.g. by parametric excitation of atoms in the optical lattice [56], or by measuring the frequency of Rabi oscillations after switching on a moving optical lattice [57].

We choose to measure the lattice depth using Kapitza-Dirac diffraction from the optical lattice [58]. In this technique, the optical lattice is flashed on for a short duration, imprinting a spatially dependent phase on the cloud. The atoms are then imaged after time-of-flight to reveal the resulting density distribution. This differs from the most commonly used method of diffraction, where atoms are loaded into the ground state of the optical lattice before release, and typically only two diffraction orders are present (although this can also be used to measure the lattice depth [57]). Here, the plane wave wave function of the BEC evolves under the lattice Hamiltonian, populating many higher Bloch bands. One advantage of measuring the lattice depth in this way is that it does not require knowledge of the lattice spacing. We work within the Raman-Nath regime, i.e. on timescales short enough that the movement of the atoms is assumed to be much smaller than the lattice spacing. To satisfy this, we require that the pulse length τ is smaller than a quarter of the period of oscillation in the bottom of the trap (approxi-

mating the sinusoidal potential as harmonic). We work with $P \sim 3$ mW and $d = 2.2$ μm, and estimating the lattice depth from the formula above, gives $\tau \ll 100$ μs. Beyond this time limit, a characteristic collapse of the diffraction orders occurs, as reported in [59].

We assume an optical potential of the form $V(x, y) = \frac{1}{2}V_x \sin(Gx) + \frac{1}{2}V_y \sin(Gy)$, G being the reciprocal lattice vector $2\pi/d$, i.e. we assume the depth of the optical lattice is uniform over the extent of the atomic cloud. Taking the single-particle Hamiltonian to comprise the potential term only, the wave function evolves as

$$\psi(x, y, \tau) = \left(\sum_{n_x=-\infty}^{\infty} \mathcal{J}_{n_x} \left(\frac{-V_x \tau}{2\hbar} \right) \mathrm{e}^{\mathrm{i}n_x G x} \right) \times \left(\sum_{n_y=-\infty}^{\infty} \mathcal{J}_{n_y} \left(\frac{-V_y \tau}{2\hbar} \right) \mathrm{e}^{\mathrm{i}n_y G y} \right) \psi(x, y, 0), \tag{2.5}$$

where $\mathcal{J}_n(z)$ is a Bessel function of the first kind, and where we have used the identity $\mathrm{e}^{\mathrm{i}z\sin\phi} = \sum_{n=-\infty}^{\infty} \mathcal{J}_n(z)\mathrm{e}^{\mathrm{i}n\phi}$.

The momentum distribution is given by the Fourier transform of the single particle density matrix, and so will have the form of peaks at $\mathbf{k} = (n_x G, n_y G)$, and the position in time-of-flight $\mathbf{r}_{\mathrm{tof}}$ is mapped to momentum as $\mathbf{r}_{\mathrm{tof}} = \hbar \mathbf{k} t_{\mathrm{tof}}/m$. The population in each peak is given by $N(n_x, n_y) = N_T \mathcal{J}_{n_x}^2(V_x\tau/2\hbar)\mathcal{J}_{n_y}^2(V_y\tau/2\hbar)$, where N_T is the total number of atoms. We use a pulse length of 50 μs, and have verified numerically that the expression for the population in each order is well described by this expression up to this timescale.

We start with a BEC of 100,000 atoms in the weak trap, with axial trapping frequency $\omega_z = 2\pi \times 56$ Hz. We release the optical axial trap only, and then after a 3 ms delay flash on the optical lattice, after which we release the magnetic trap and the optical lattice at the same time.[7] After 20.5 ms time-of-flight, we take an absorption image in the xy-plane. To determine the trapping depth as a function of optical power, we vary the amplitude of the rf signal supplied to the AOD. Examples of the absorption images obtained are shown in Figure 2.5. We also take images at multiple orientations of the lattice, to monitor how the lattice depth changes as a function of rotation angle.

[7] Releasing the axial trap first reduces the mean-field interaction energy, thus reducing the unwanted effects of the atom-atom interaction in the diffraction images.

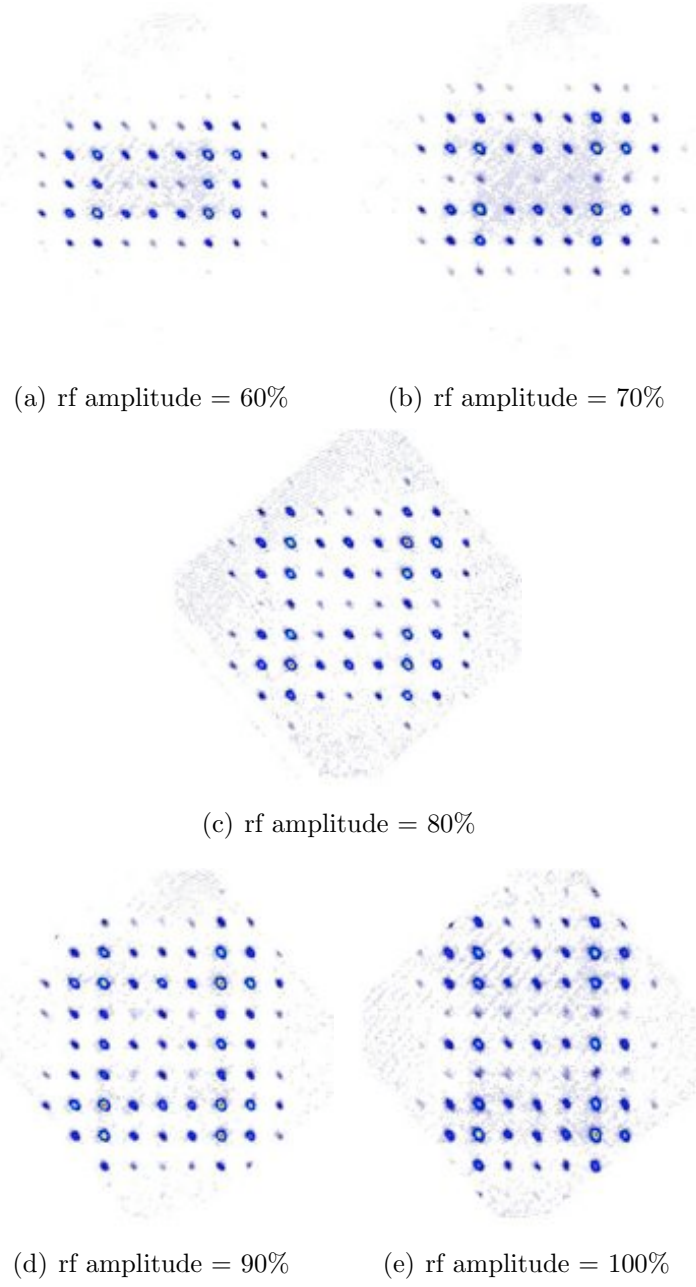

(a) rf amplitude = 60%

(b) rf amplitude = 70%

(c) rf amplitude = 80%

(d) rf amplitude = 90%

(e) rf amplitude = 100%

Figure 2.5: False colour plots of absorption images taken in the xy-plane at 20.5 ms time-of-flight, after an optical lattice has been flashed on for 50 μs. In these plots the horizontal lattice depth V_x is kept constant while the vertical lattice depth V_y is increased by changing the amplitude of the rf signal supplied to the AOD. In the sequence, the lattice was oriented at 130°, and the images subsequently rotated.

To extract the optical lattice depth from these images, we first clean the images to remove fringes by removing high-frequency noise in the Fourier transform of the images, and rotate the image so that the lattice axes are perpendicular to the image axes (Figure 2.5 shows the images already cleaned and rotated). For each of the two lattices, we integrate over the perpendicular direction, and fit to the thermal background, which is then subtracted. We then perform a multi-peak Gaussian fit to determine the relative population in each of the diffraction peaks. These peaks $n_{x(y)}$ are then fitted to $\mathcal{J}^2_{n_x}(V_{x(y)}\tau/2\hbar)$ to determine the depth.

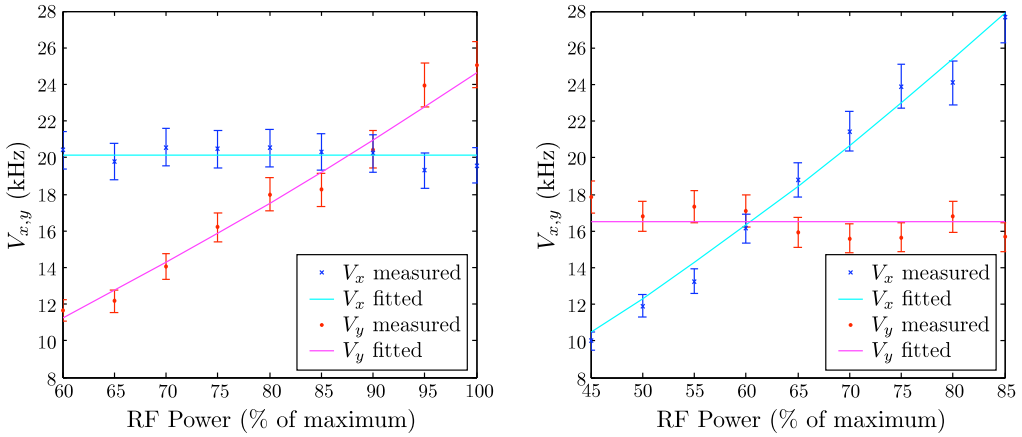

(a) $A(X_4)$ constant at 65%, $A(X_1)$ varied (b) $A(X_1)$ constant at 80%, $A(X_4)$ varied

Figure 2.6: Lattice depth as a function of the amplitude of the rf signal supplied from a given DDS chip $A(X_{1(4)})$. The lattice depths are calculated by fitting Bessel functions to the relative populations of the diffracted orders. The lattice depth varies as $V_x \propto A(X_1)^{1.55}$, and $V_x \propto A(X_4)^{1.54}$.

Figure 2.6 shows the lattice depths obtained as a function of the amplitude of the rf signal supplied to the AODs. Note that the diffracted optical power is not proportional to this value: we perform a fit of the form $V_{x(y)} = bA(X_{1(4)})^c$, where $A(X_{1(4)})$ is the amplitude of the rf signal supplied from a given DDS chip. We also measure the diffracted optical power as a function of $A(X_{1(4)})$, and find the dependence is consistent with that fitted for the depth. This technique allows us to determine the optical depth to an accuracy of $\pm 5\%$. It also allows us to determine a relation for the lattice depth as a function of optical power (measured just before the four-lens objective), which we find to be 6.0 kHz/mW. This value is lower than the value calculated using equation (2.4) above, which can be explained by power losses at the four-lens objective and glass cell, as well differences in intensity between to the two beam pairs

at the position of the atoms.

There is a small long-term variation in the lattice depth (around 2 kHz, noticeable in Figure 2.6) as a function of optical power over the course of the day, which is improved by taking care to ensure that fluctuations of the temperature in the lab over a 24 hour period are kept to a minimum ($< 1°$). However, this variation makes it difficult to use this technique for normalising the beam depth as a function of lattice angle, and instead we use the power of the beams measured after the four-lens objective for normalisation.

Optical lattice spacing

Although it is possible to calculate the lattice spacing using the beam deflection angle from the AOD and the focal lengths of the lenses, again it is more accurate to calculate this value directly. A detailed discussion of these effects and of calibration of the lattice spacing is given in [48], and what follows is a summary. We measure the optical lattice spacing in three ways:

Spacing of interference fringes In our arrangement, the vacuum system is mounted on rails, and can be easily rolled out so that the focal plane of the four lens objective can be reached. We can then image the interference fringes directly by placing a mirror in the focal plane, and reflecting the optical lattice light back through the axial imaging system to form an image on the CCD camera.

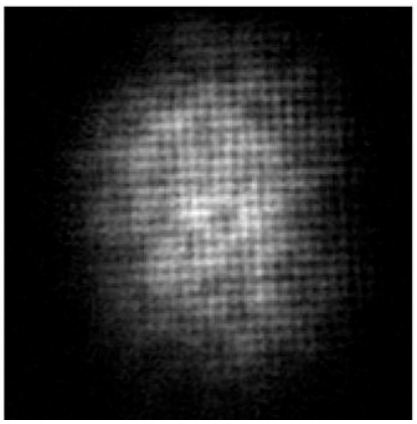

Figure 2.7: Axial absorption image of atoms trapped in an optical lattice with spacing 4.6(1)μm. The field of view is 140×140 μm.

Imaging atoms trapped in the optical lattice For lattice spacings of 4.6 μm and above, we can resolve individual lattice sites, and so determine the lattice spacing directly. Figure 2.7 shows such an image at the minimum resolvable lattice spacing.

Distance between diffraction orders

As described above, the distance between diffraction orders in time-of-flight is given by the condition $k = 2\pi/d = mx_{\mathrm{tof}}/\hbar t_{\mathrm{tof}}$. This allows us to determine small lattice spacings. However, the distance between orders can be

significantly modified by interaction effects which reduces the accuracy of this measurement technique.

We find that the lattice spacing is related to the rf frequency as $d = (8.53(4)/\Delta\nu)$ μm, where $\Delta\nu$ is given in MHz.

2.4.3 Loading atoms into the optical lattice

When performing experiments with the optical lattice it is important that atoms are loaded adiabatically, i.e. that atoms are loaded into the ground state of the optical lattice as the lattice depth is ramped up. The requirements to ensure this depend on the properties of the condensate that are loaded into the optical lattice.

In the case where the density is low, such that the mean-field interaction is negligible, the important timescale is that set by the gap E_g to the first excited state. To ensure that no atoms are excited from the ground state $|0\rangle$ to the first excited state $|1\rangle$, the adiabaticity criterion $|\langle 1|\dot{H}|0\rangle| \ll E_g^2/\hbar$ should be satisfied (where we assume that the initial momentum of the condensate is zero). The energy gap $E_g \geqslant 4E_R$ (where E_R is the lattice recoil energy $\hbar^2(G/2)^2/2M$) for all V_0 for zero quasimomentum, so the requirement is that $\dot{V}_0 \ll 16E_R^2/\hbar$ [60]. For a 2.2 μm lattice, $E_R = h \times 119$ Hz. Assuming a linear ramp of lattice depth to $V_0 = h \times 2$ kHz, the requirement is that the ramp time should be much greater than 1.4 ms (although it would be possible to ramp faster than this while satisfying the adiabaticity criterion if an exponential ramp was used).

This criterion ensures that the ramp in depth is adiabatic with respect to the single-particle motion only. When atom-atom interactions are important, as they are for our experimental parameters, the lattice ramp must be adiabatic with respect to the interaction timescale. This can be understood as follows: when the optical lattice is ramped up, the density at the potential minima increases, increasing the mean-field energy. To minimise the energy, the radius of the cloud increases, leading to the sum of the mean field energy $U_0|\psi(\mathbf{r})|^2$ and the trap potential being constant across the optical lattice (in the Thomas-Fermi limit).

We can determine the time required to ramp up the optical lattice adiabatically by numerically solving the 2D Gross-Pitaevskii equation (GPE) using a time-splitting spectral method (see Appendix B for details). We take the 2D interaction parameter $\beta = 1000$, which corresponds to around 80,000 atoms with $\omega_z = 2\pi \times 100$ Hz. We start with the ground state in the harmonic trap, ramp up a 2.2 μm optical lattice with an exponential ramp, and then determine the final wave function $\psi_f(\mathbf{r})$ for different ramp times. This final wave function is then compared to the ground state in the optical lattice

$\psi_g(\mathbf{r})$ by calculating the overlap $|\int \psi_g^*(\mathbf{r})\psi_f(\mathbf{r})\mathrm{d}\mathbf{r}|^2$.

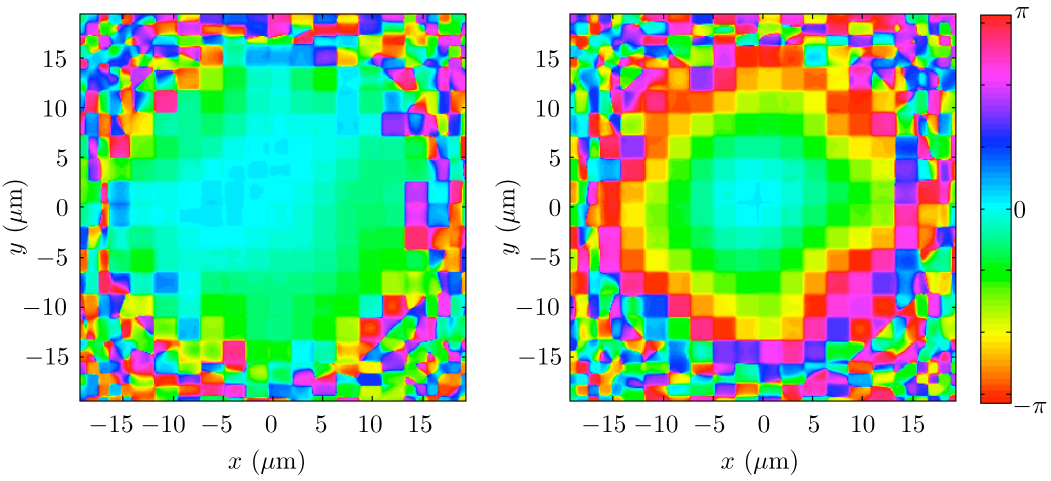

(a) $t_{\mathrm{hold}} = 0$ (b) $t_{\mathrm{hold}} = 15.5$ ms

Figure 2.8: Phase of the wave function after an optical lattice has been ramped up to 4 kHz in 40 ms for different hold times t_{hold}. Immediately after the ramp the phase is relatively uniform at the overlap with the ground state is 0.77. While held in the trap the phase at each lattice site evolves at a different rate, and after 15.5 ms hold the wave function has dephased, and the overlap dropped to 0.27.

Note that the overlap found straight after the ramp can be misleading: if the ramp time is too short, the sum of the mean field energy $U_0|\psi(\mathbf{r})|^2$ and the trap potential are not constant across the lattice, and the phase at each lattice site evolves at a different frequency. Thus the overlap with the ground state initially oscillates, and at certain times the phases can be approximately constant. The effect is illustrated in Figure 2.8 which shows the phase of the wave function directly after the lattice is loaded, and then at a later hold time corresponding to a minimum in overlap with the ground state. The effect of this was shown experimentally in [61], where it was found that the visibility of the interference pattern oscillates in time when the loading of the lattice was nonadiabatic with respect to the chemical potential.

Figure 2.9 shows the overlap calculated as a function of ramp time, showing the full range of calculated overlaps after 200 ms hold in the optical lattice. The plot shows that ramp times of a few hundred milliseconds are necessary to remain adiabatic. This is consistent with our observations of expansion in time-of-flight after ramping on the optical lattice, where the visibility of the diffraction peaks is largest for ramp times of 500 ms and above.

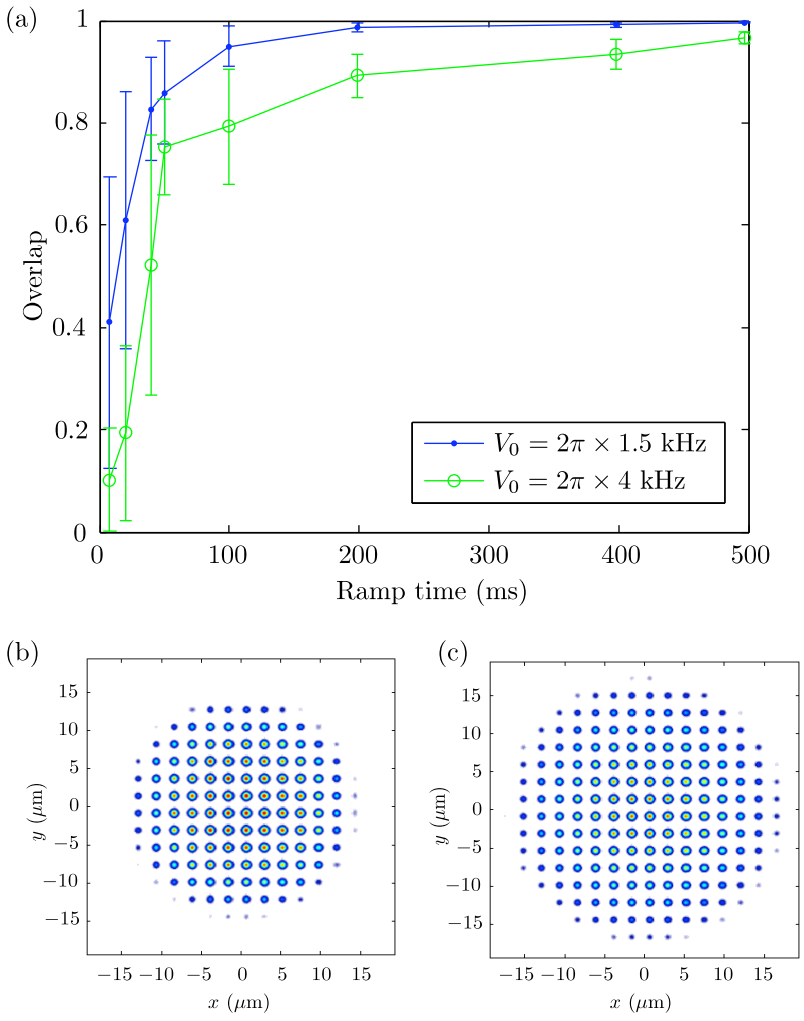

Figure 2.9: Data calculated for different ramp times for a 1.5 kHz and 4 kHz optical lattice. (a) Overlap with the ground state in the optical lattice after the lattice depth is ramped exponentially for different times. The error bars denote the minimum and maximum overlaps in 200 ms hold in the optical lattice. (b) and (c) Plots of the density after a 4 kHz lattice is ramped up in 8 ms and 500 ms respectively. Note the difference in the radii of the clouds.

Chapter 3

Optical lattice with dynamically variable periodicity

We have published the results in this chapter in [62].

3.1 Single site imaging using an accordion lattice

As described in Chapter 1, optical lattices create clean, tunable and flexible periodic potentials for ultracold atoms that are an important tool for investigating the quantum behaviour of strongly correlated many-body systems [16, 20, 21]. Such investigations require lattices with sub-micron spacing to ensure that the quantum dynamics occurs on millisecond timescales (and so is not subject to decoherence). The small spacing also ensures that the tunnelling energy J and on-site interaction energy U are comparable ($J/U \sim 1$) at a lattice depth for which the band gap $E_g \gg k_B T$, assuming a typical temperature of tens of nanokelvin. The sub-micron lattice spacing makes it challenging to observe atoms at individual lattice sites with light or near infrared radiation, and typically time-of-flight expansion has been used to probe the momentum of the atoms [17]. Being able to detect the position of the atoms *in situ* can yield further information about the system, and the ability to address atoms at single lattice sites is crucial for quantum information processing [63]. *In situ* imaging of the atoms has been demonstrated for lattice spacings from 2 μm upwards [64, 65, 66], however at these spacings the

single-atom tunnelling is negligible on typical experimental timescales. Scanning electron microscopy has been used to detect single atoms in a 0.6 μm optical lattice and determine the density distribution by summing over multiple images [67]. Recently there has been significant progress on directly imaging single atoms trapped in optical lattice sites at sub-micron lattice scales using fluorescence imaging [25, 26]: in both cases sophisticated optical arrangements were used. The difficulty of obtaining the theoretical maximum resolution in an optical imaging system increases dramatically as the numerical aperture increases.

Our method of imaging such systems is to use a lattice with a dynamically variable spacing. Ultracold atoms are prepared in a lattice with small spacing and then the lattice potential is expanded to facilitate imaging. This allows individual lattice sites to be resolved without the need for a complex or expensive microscope arrangement. This approach could also be used for addressing individual lattice sites; a previous experiment [66] demonstrated addressing single lattice sites spaced by 5.3 μm. Increasing the spacing between the trapped atoms also reduces the error in qubit readout fidelity introduced by cross talk between neighbouring atoms [68]. Dynamically varying the lattice spacing could provide a promising technique for measurement based quantum computing where very high ground state fidelities are required — after a cluster state is created [69, 70] the optical lattice could be expanded to allow measurements to be carried out.

3.1.1 Background

Diffraction from a 1D lattice with variable periodicity [59], and investigation of the dynamics of a BEC loaded into a large period 1D lattice with tuneable spacing [71] have been demonstrated; neither of these arrangements, however, were capable of changing the lattice spacing whilst keeping the atoms trapped. Transport of ultracold atoms in optical lattices has also been demonstrated: an accelerating optical lattice has been used to transfer momentum to a BEC in multiples of the $\hbar G$ [60]; and atoms have been transported up to 20 cm in a moving 1D optical lattice [72]. An arrangement for generating 1D dynamically varying accordion lattices has been shown [73] in which mechanical means were used to vary the lattice spacing from 0.96 μm to 11.2 μm over one second (although it was not demonstrated with trapped ultracold atoms).

We have demonstrated the first use of an accordion lattice arrangement to dynamically increase the optical lattice spacing while the atoms are trapped. Unlike in the work described above [59, 71, 73], the lattice spacing is increased in two dimensions, and the arrangement allows the optical potential to be

varied smoothly and quickly, free of mechanical vibrations. We show that the atoms remain trapped in the optical lattice for ramp times as short as a few milliseconds, well within the timescales of a typical BEC experiment.

3.1.2 Experimental sequence

The accordion lattice is generated as described in Chapter 2, and yields an optical lattice potential of the form

$$V(x, y, t) = V_l(x, y)\{\cos^2[\pi x/d(t)] + \cos^2[\pi y/d(t)]\}; \tag{3.1}$$

the spatially-dependent lattice depth $V_l(x, y)$ has a Gaussian distribution $-V_0 \exp[-2(x^2 + y^2)/w^2]$, where V_0 is the peak lattice depth and w is the waist.

We start with a nearly pure BEC of 80,000 ^{87}Rb atoms in the $F = 1, m_F = -1$ state in a combined magnetic and optical trap with harmonic trapping frequencies $\{\omega_r, \omega_z\} = 2\pi \times \{20.1, 112\}$ Hz.[1] This trap is on for the remainder of the experimental sequence. An optical lattice potential of the form given in Equation (3.1) with $V_0 = h \times 1.5$ kHz, $w = 69$ μm and $d = 2.2$ μm is ramped on in 500 ms. This timescale is long enough to ensure the system is in the ground state of the optical lattice.

Figure 3.1(a) shows an *in situ* absorption image of atoms trapped in the optical lattice. As described in the previous chapter, we first apply the repumping light to drive the atoms to the $F = 2$ hyperfine level, and then probe the atoms by applying a 20 μs pulse of circularly polarised light resonant with the $5S_{1/2}$ $F = 2$ – $5P_{3/2}$ $F' = 3$ transition. To image these dense clouds, the optical pumping light is detuned to ensure only a fraction of the atoms are pumped to the $F = 2$ level. The detuning is chosen such that the optical density in the lattice is reduced to order one to prevent saturation of the absorption images. The individual lattice sites cannot be resolved, because the finite axial extent of the cloud, which is 11 μm diameter or more, is comparable with the depth of field of the imaging system. The trapped cloud has radius $r_0 = 18$ μm, which indicates that there are around eight lattice sites filled in each direction, with around 1200 atoms in each central lattice site.

The lattice depth is then ramped to $h \times 37$ kHz in 5 ms, which cuts off tunnelling between the lattice sites. This ensures that the lattice dynamics are frozen during the expansion of the lattice. The ramp time is short

[1] We use a small BEC for this sequence for technical reasons: the smaller axial extent of the BEC improves imaging, and a smaller number of sites loaded means that a larger expansion ratio can be achieved (as explained below).

compared to the single-particle tunnelling time, however it is long enough to ensure that the atoms remain in the lowest energy band of the optical lattice, i.e. $\langle \partial H/\partial t \rangle \ll E_g^2/\hbar$.

The lattice spacing is varied as a smoothed ramp given by the Gauss error function $d(t) = d_0(1 + (\mathcal{S} - 1)\{\mathrm{erf}[7.14(t/t_r - 0.5)] + 1\}/2)$, where d_0 is the initial spacing (2.2 μm), $\mathcal{S}$ is the ratio of the final spacing to the initial spacing and t_r is the ramp time (which is varied). The peak lattice depth V_0 is kept constant during the ramp, and $\mathcal{S}$ is 2.5. In principle the lattice spacing can be expanded to any size provided that the lattice spacing remains smaller than the beam waist w. In practice, to ensure that atoms at the edge of the cloud are not lost, $\mathcal{S} \lesssim w/r_0$ should be satisfied. For our parameters, after a 2.5 times expansion, the radius is 45 μm, and the depth at the outermost lattice site has dropped to about 40% of the depth at the centre of the lattice. The final lattice spacing, 5.5 μm, is large enough to be resolved by our imaging system, as shown in Figure 3.1(b). The number of lattice sites filled is consistent with the dimensions of the cloud before expansion. To confirm that the accordion lattice is working as expected, we also expand by a factor of 2.5 from an initial lattice spacing that is large enough to be resolved before expansion (5.5 μm to 13.75 μm). The result, presented in Figure 3.1(c) and 3.1(d), shows that the atoms do remain bound for this ramp.

3.1.3 Estimate of minimum ramp time

During the expansion of the lattice, the central lattice site remains stationary,[2] while the first lattice site moves with speed $v_1 = \dot{d}$, the second lattice site moves with speed $v_2 = 2\dot{d}$, and the n^{th} lattice site moves with speed $v_n = n\dot{d}$, as illustrated in Figure 3.2. To determine the evolution of the system during the ramp in lattice spacing, we describe the atoms at each lattice site by localised wave functions $|\psi_{n_x,n_y}\rangle$, evolving according to

$$i\hbar \frac{\partial |\psi_{n_x,n_y}(t)\rangle}{\partial t} = \left(\frac{p^2}{2M} + V(x,y,t) \right) |\psi_{n_x,n_y}(t)\rangle, \tag{3.2}$$

where M is the mass of an atom, and interactions are ignored.

If the accordion lattice is to be used for quantum computing, it is important that the ground state fidelity remains high during the lattice expansion. However, if the lattice is expanded for the purpose of imaging the atoms,

[2]We assume that the position of the central lattice site corresponds to the centre of expansion. In practice the position of the central lattice site will depend on the relative phase of the lattice beams.

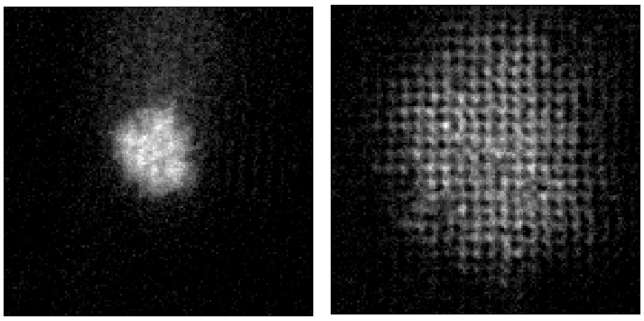

(a) Before ramp (b) After ramp

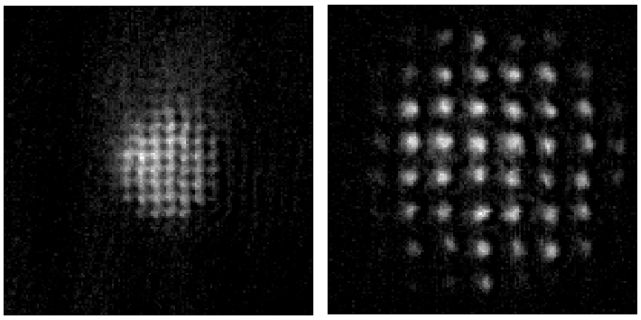

(c) Before ramp (d) After ramp

Figure 3.1: Absorption image of atoms trapped in a two-dimensional optical lattice before and after the lattice spacing has been ramped by: a factor of 2.5 from 2.2 μm to 5.5 μm in 10 ms [(a) and (b)]; a factor of 2.5 from 5.5 μm to 13.75 μm in 50 ms [(c) and (d)]. The field of view is 120 μm by 120 μm in each image.

moving the atoms slowly enough to retain high ground state fidelity is not necessary — instead there is the less stringent requirement that an atom remains in a bound state of the same lattice site.

To estimate the maximum acceleration for which the atoms in the n^{th} well remain bound, we can move to an accelerating reference frame in which the n^{th} lattice site is at rest. In this reference frame, the lattice potential is tilted due to a linear potential term $Mn\ddot{d}x$ [74] which has the effect of reducing the potential barrier between neighbouring lattice sites, as illustrated in Figure 3.3. The minimum barrier height ΔV is given by

$$\frac{\Delta V}{V_0} = \sqrt{1 - A^2} + A(\arcsin(A) - \pi/2), \tag{3.3}$$

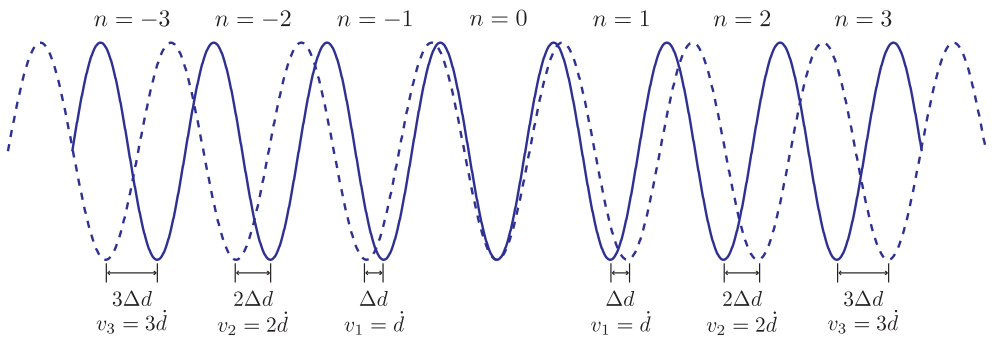

Figure 3.2: Illustration of the relative speed of neighbouring lattice sites when the optical lattice is expanded.

where A is the scaled acceleration $A = Mn\ddot{d}d/\pi V_0$.[3] We would expect atoms to be lost when the minimum barrier height ΔV approaches the energy of the trapped atoms, which for our experimental parameters would occur for accelerations corresponding to a ramp time of around 3 ms. Since ΔV decreases with increasing scaled acceleration, the maximum acceleration can be larger for a deeper lattice, or for a smaller lattice spacing. This approach gives an order of magnitude estimate for the minimum expansion time, however it does not take into account the reduction of the barrier height during expansion due to the envelope of the lattice beams, the effect of the magnetic trap, nor does it take into account excitations to higher bands during the ramp.

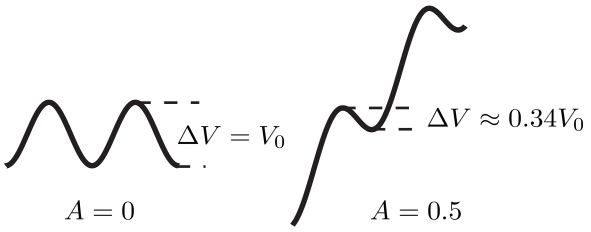

Figure 3.3: Effective trapping potential at the n^{th} lattice site in a reference frame accelerating at $n\ddot{d}$, in terms of the scaled acceleration $A = Mn\ddot{d}d/\pi V_0$.

We perform a more detailed analysis of the minimum expansion time by numerically solving Equation (3.2). The optical lattice potential $V(x, y, t)$

[3]The fact that the barrier height in the accelerating frame goes to zero when $A = 1$ can be understood classically, by equating $Mn\ddot{d}$ with the maximum restoring force of the sinusoidal potential in the lab frame $\pi V_0/d$.

has the form given in Equation (3.1), with our experimental parameters ($V_0 = h \times 37$ kHz, $d_0 = 2.2$ μm, $w = 69$ μm, $\mathcal{S} = 2.5$) and the harmonic trapping potential is included. We take the initial wave function $|\psi_{n_x,n_y}(t = 0)\rangle$ to be the ground state of a single well of the sinusoidal potential centred on $x = n_x d_0$, $y = n_y d_0$. A sixth order finite difference formula is used to express the second derivative, and the wave function is evolved using the propagator $U(t) = \exp[-iH(t)\Delta t/\hbar]$ for each time-step Δt. We solve Equation (3.2) in one dimension along the direction of motion for each lattice site.[4]

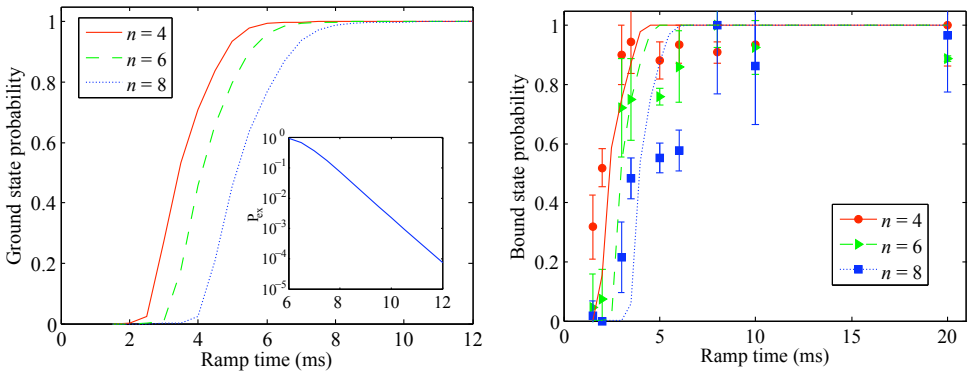

(a) (b)

Figure 3.4: (a) Numerically calculated probability of finding a single particle in the ground state of the $\cos^2(x)$ potential well of the n^{th} lattice site after the spacing is increased from 2.2 μm to 5.5 μm for different ramp times. $V_0 = h \times 37$ kHz. The inset in (a) shows the excited state probability against ramp time for the outermost lattice site ($n_x = 8$, $n_y = 8$). (b) Probability of finding an atom in a bound state for the same parameters. The lines denote the numerically calculated probability and the points show experimental data.

The probability of an atom remaining in the ground state, $|\langle\psi_{n_x,n_y}(t = t_r)|\psi_{\text{ground}}\rangle|^2$, is shown in Figure 3.4(a) (we find the probability for the n^{th} lattice site by averaging over n_y for each value of n_x). For the outermost lattice site ($n_x = 8$, $n_y = 8$) the ground state fidelity is more than 99.99% for ramp times longer than 12 ms. The time taken to spontaneously scatter a photon is 7 s in our lattice (with $V_0 = h \times 37$ kHz), and can be several minutes in optical lattices with blue frequency detuning. Thus many expansion and addressing operations could be carried out with high fidelity before coherence is destroyed due to spontaneous emission.

[4]We have also calculated the ground state probability for one set of parameters in two dimensions, to verify that ignoring the dynamics along the direction perpendicular to motion does not introduce significant errors.

The probability of an atom remaining in a bound state of the optical lattice is also calculated numerically and we compare this with experimental results. In the experiment, we expand the lattice as described above for different ramp times. To determine the probability of an atom in a given site remaining bound, we first sum over the columns of the lattice, then calculate the number of atoms in site n. The number of atoms in the outermost site does not change (within the margin of error) for expansion times between 8 and 20 ms, so the number of atoms is normalised to the number of atoms in site n for these ramp times. The results are shown in Figure 3.4(b).

The experimental and numerically calculated results agree well. The small discrepancy (the ramp time for a given probability is slightly longer in the experiment) may be due to the fact that the numerical results are for a single particle only. In the experiment, however, there are on average a few hundred atoms per lattice site, and the calculations do not take into account the energy due to repulsive interactions. The close agreement with the numerically calculated results indicates that the main source of atom losses is the speed of expansion rather than from a source of instability in the ramp, confirming that the ramp of the optical potential is smooth.

Note that the minimum ramp time has been calculated for only one lattice depth and one form of ramp. With a deeper lattice, the expansion timescales would be even faster. Also, we have found (through numerical calculations) that the minimum ramp time has a strong dependence on the form of the ramp, and it is possible that the minimum ramp time could be reduced further by optimising this.

3.1.4 Extensions to technique

In this experiment the initial lattice spacing was 2.2 μm, and this technique can be easily used to expand from smaller lattice sizes if a higher numerical aperture (NA) lens is used to form the optical lattice — the minimum lattice spacing $d_{\mathrm{min}} = \lambda_l/2\mathrm{NA}$, where λ_l is the wavelength of light forming the optical lattice. Note that d_{min} is not equal to the imaging resolution; atoms can just be resolved when they are spaced by more than $d_{\mathrm{res}} = 0.61\lambda_i/\mathrm{NA}$, where λ_i is the wavelength of imaging light. For $\lambda_l < \lambda_i$ (blue frequency detuning) the lattice spacing is smaller than the imaging resolution.

Note that this technique can be extended to three dimensions by applying an additional accordion lattice in the axial direction, enabling planes of atoms to be moved out of focus of the imaging system, thus facilitating imaging of a single plane. The use of an accordion lattice for expanding the period of an optical lattice has been demonstrated for the case of absorption imaging, but it could also be utilised for single atom fluorescence imaging.

3.2 Other applications of accordion lattice

In our experiments on the accordion lattice we have concentrated on proving its usefulness for expansion of cold atoms in a periodic potential which is equivalent to increasing the magnification of the optical imaging system, however there are other modes of operation of the accordion lattice.

3.2.1 Flexible lattice potentials

Two, or more, optical lattices of different spacing can be created at the same time by applying the requisite driving frequencies to the AODs. The principle of superposition works for reasonable rf powers and the light intensities and resulting optical potentials add together as for the orthogonal lattices described above [75]. In this way cold atoms can be into an optical lattice of double wells (which is an example of a superlattice) in two ways. The atoms can be loaded directly into a potential arising from the addition of two lattices of period d and $2d$ with control of the phase (or spatial offset) between them. The atoms could be loaded into a lattice of period d, the spacing of the wells then expanded to $2d$ and then another lattice of spacing d gradually switched on to split each potential well in two. This splitting process could be repeated to further subdivide the cloud of atoms. Note that for the loading to be reproducible, the lattice beams must be phase-stabilised (which is not the case in our experiment).

3.2.2 Adjusting system parameters

The optical lattice can be expanded to decrease the tunnelling energy without changing the lattice depth, allowing investigation of different quantum phases. This could be used to reduce the tunnelling energy J whilst leaving the trap depth constant. However it should be noted that increasing the lattice spacing will also decrease the on-site interaction energy U, although the ratio U/J will in general increase with an increase in lattice spacing.

3.2.3 Spatially varying modulation

When an oscillating force is applied to atoms in an optical lattice, it can modify the tunnelling energy J [76]. This can be understood by considering the Floquet states for the periodically time-dependent Hamiltonian of the system, and assuming that the periodic driving does not excite atoms to higher Floquet zone, the J is renormalised as $\mathcal{J}_0(K/\hbar\omega_s)$, K is the modulation strength, and ω_s is the modulation frequency. If the optical lattice is

'shaken' uniformly, then the ratio U/J can be controlled, and at $K/\hbar\omega \approx 2.4$, J becomes zero. This has been performed experimentally, and the transition between a superfluid and a Mott insulator observed [77].

In our system, an oscillating force could be applied to the atoms by rapidly oscillating the lattice periodicity. However, with reference to Figure 3.2, it is clear that the modulation amplitude will not be constant in the lattice, but instead will increase linearly with increasing distance from the lattice.[5] This could then provide a spatially varying modulation of the tunnelling parameter. The modulation amplitude could be arranged so that the argument of the Bessel function becomes zero at a predefined radius, thus providing a box-like potential. It has also been predicted that a spatially inhomogeneous tunnelling element could be used to achieve a truly incompressible Mott phase in a harmonic trap [78].

[5] Although the analysis is complicated by the fact that the lattice spacing is also varying as the force is applied.

Chapter 4

Artificial magnetic fields: mean-field regime and route to strongly-correlated states

In Chapter 1 it was explained how an artificial magnetic field modifies the tight-binding Hamiltonian by adding phase factors on the hopping terms. Many different methods have been proposed for generating such artificial magnetic fields, both in the continuum and specifically in optical lattices. The presence of the periodic potential leads to a rich phase diagram that depends on the interplay of the optical lattice parameters and the magnitude of the magnetic field.

4.1 Artificial magnetic fields and optical lattices

4.1.1 Generating artificial magnetic fields

In the following, we assume that the magnetic field $\mathbf{B}$ is aligned along the z-axis. An electron in a magnetic field $\mathbf{B}$ experiences a Lorentz force $\mathbf{F}_L = -e(\mathbf{v}\times\mathbf{B})$, where e is the electronic charge. This corresponds to the covariant momentum $\mathbf{P}$ of an electron in a magnetic field being $\mathbf{P} = \mathbf{p} + e\mathbf{A}$, where $\mathbf{A}$ is the magnetic vector potential. Taking the symmetric gauge we have $\mathbf{A} = \frac{1}{2}\mathbf{B}\times\mathbf{r} = \frac{1}{2}B(-y, x, 0)$. The single-electron system is described by the

Hamiltonian

$$H_{\mathrm{e}} = \frac{1}{2M}\left[\left(p_x - \frac{eBy}{2}\right)^2 + \left(p_y + \frac{eBx}{2}\right)^2\right]. \tag{4.1}$$

The electron undergoes cyclotron motion in the magnetic field and the energy of the system is given by discrete Landau levels with spacing $\hbar\omega_c$, where $\omega_c = eB/M$ is the cyclotron frequency.

Most methods for generating artificial magnetic fields in ultracold atom systems fall into two categories: the first of these is to rotate the system in some way [79, 80] (and we perform rotation using the optical lattice described in Chapter 2); the second of these is to generate an artificial geometric potential using a suitably designed laser field [81].

Rotating an optical lattice

To create an artificial magnetic field, we wish to apply a force of the same form as the Lorentz force to a neutral particle. A conceptually simple way of generating this force is to move to a frame rotating at angular frequency Ω, which leads to a Coriolis force $\mathbf{F}_C = 2M(\mathbf{v} \times \mathbf{\Omega})$. Generation of an artificial magnetic field using rotation is suitable when the confining potential is symmetrical about the rotation axis.

We can see how rotating the system leads to an artificial magnetic field by transforming to the rotating frame. This is done by switching from the co-ordinates in the lab frame x_L, y_L to coordinates x, y in a frame rotating at frequency Ω.

This transforms the Hamiltonian in the lab frame H_L to the Hamiltonian in the rotating frame as $H_{\mathrm{rot}} = H_L - \mathbf{\Omega} \cdot \mathbf{L}$, where $\mathbf{L}$ is the total angular momentum [82]. This leads to the following Hamiltonian:

$$\begin{aligned} H_{\mathrm{rot}} &= \frac{\mathbf{p}^2}{2M} + \frac{1}{2}M\omega^2(x^2+y^2) - (\mathbf{\Omega}\times\mathbf{r})\cdot\mathbf{p}, \\ &= \frac{1}{2M}\left[(p_x + M\Omega y)^2 + (p_y - M\Omega x)^2\right] + \frac{1}{2}M(\omega^2 - \Omega^2)(x^2+y^2). \end{aligned} \tag{4.2}$$

Here it is assumed that the rotation axis is perpendicular to the x-y plane, and that movement is suppressed in the direction parallel to the rotation axis so the system can be represented in two dimensions. Note that one effect of moving to a rotating frame is the introduction of a centrifugal term $-\frac{1}{2}M\Omega^2(x^2+y^2)$ in addition to the Coriolis term, and if the harmonic trapping frequency is smaller than the rotation frequency the particle will no longer be trapped.

By comparing equations (4.2) and (4.1) it is clear that the behaviour of an electron in a magnetic field is analogous to a particle in rotating system when the centrifugal term is exactly balanced by the harmonic trap potential, i.e. when $\omega_{\text{eff}}^2 \equiv \omega^2 - \Omega^2 = 0$. The artificial magnetic field in the rotating system has magnitude $B = 2M\Omega/e$, and the cyclotron frequency is given by $\omega_c = 2\Omega$.

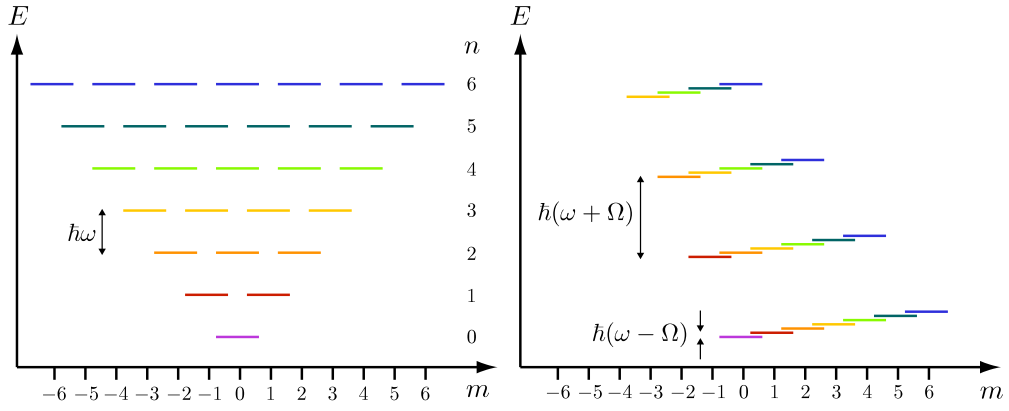

Figure 4.1: Energy levels in a harmonic trap with trapping frequency ω when there is no rotation (left), and in a frame rotating at angular frequency Ω (right). When $\Omega = 0$, for each harmonic oscillator level n there are $2n + 1$ degenerate angular momentum states m. These split for non-zero Ω, and for $\Omega = \omega$ degenerate Landau levels are formed. (The levels are colour coded according to n.)

The energy levels are given by $E(n, m) = n\hbar\omega + m\hbar\Omega$, where m is the angular momentum which ranges from $-n$ to n in steps of two. This is shown in Figure 4.1. For $\Omega = 0$ the energy eigenvalues are simply the harmonic oscillator levels, while for $\Omega = \omega$ the energy eigenstates are a series of Landau levels. For a small non-zero $\omega - \Omega$, each Landau level splits into sub-levels of spacing $\hbar(\omega - \Omega)$. The lowest Landau level (LLL) description is appropriate when the temperature and interaction energy is smaller than the gap to the next Landau level. By considering the chemical potential in a rotating condensate $\mu \sim \hbar\omega[(Na_s/a_z)(1 - \Omega/\omega)]^{1/2}$ the condition of the interaction energy requires [21]

$$1 - \frac{a_z}{Na_s} < \frac{\Omega}{\omega}, \tag{4.3}$$

where a_z is the harmonic oscillator length in the axial direction. For $\omega_z = 2\pi \times 112$ Hz, and $N = 100,000$, this requires $\Omega/\omega > 0.998$

We now consider the Hamiltonian for bosons in a rotating optical lattice.

As described in section 1.3.1, the Bose-Hubbard Hamiltonian is modified by phases $\phi_{\mathbf{r}_1,\mathbf{r}_2}$ on the hopping terms, which are related to the vector potential by $\phi_{\mathbf{r}_1,\mathbf{r}_2} = (M/\hbar)\int_{\mathbf{r}_1}^{\mathbf{r}_2} \mathbf{A}\cdot \mathrm{d}\mathbf{r}$. For a rotating lattice, the vector potential is given by $\mathbf{\Omega}\times\mathbf{r}$, which gives $\alpha = 2M\Omega d^2/h$, with the Hamiltonian given by

$$H = \sum_{i,j}\Big\{-J\left(e^{\mathrm{i}\pi\alpha i}\,\hat{a}^\dagger_{i,j}\hat{a}_{i,j-1} + e^{-\mathrm{i}\pi\alpha j}\,\hat{a}^\dagger_{i,j}\hat{a}_{i-1,j} + \text{h.c.}\right) + \varepsilon_{i,j}\hat{a}^\dagger_{i,j}\hat{a}_{i,j} + \frac{U}{2}\hat{a}^\dagger_{i,j}\hat{a}^\dagger_{i,j}\hat{a}_{i,j}\hat{a}_{i,j}\Big\}, \tag{4.4}$$

where $i = x/d$ labels the lattice index in the x-direction, $j = y/d$ labels the lattice index in the y-direction, J is the hopping matrix element between adjacent sites, U is the on-site interaction energy, and $\varepsilon_{i,j} = \frac{1}{2}m\omega^2_{\text{eff}}(i^2+j^2)d^2$ is the energy offset on each lattice site when there is a difference between the harmonic trapping frequency and the rotation frequency. The single particle spectrum of this Hamiltonian is described in section 4.1.2.

Other methods

Another way to generate an artificial magnetic field is to use laser fields that cause an atom to gain an Aharanov-Bohm geometric phase factor when it follows a closed contour. The Lorentz-type force results from the perturbation of the atomic internal state due to the slow motion of the atom through the laser field [83]. In one proposal [84] the magnetic field is generated using Raman transitions with a position-dependent detuning. This has been demonstrated experimentally in continuous system [85, 86], although an optical lattice potential could be added to the arrangement. Artificial magnetic fields can also be generated by using beams with orbital angular momentum [87, 88]. Other schemes rely on the presence of an optical lattice potential, and laser assisted tunnelling between two state-dependent optical lattices can be used to generate phases on the hopping terms. To ensure that the correct phases are generated (rather than a staggered magnetic field), the schemes include an additional linear potential gradient [89], or a superlattice potential [90]. One advantage of using these methods is that there is no centrifugal term. These schemes are also less sensitive to imperfections in (the non-rotating part of) the trapping potential. However, there can be other complications that limit the maximum magnetic field that can be reached, such as heating from the Raman beams.

Instead of rotating the optical lattice, one scheme proposes generating a phonon-induced artificial magnetic field for atoms in a stationary, ring-shaped optical lattice immersed in a rotating BEC [91, 92]. Another pro-

posal involves a combination of a time-varying quadrupolar potential and a modulation of J in time [93].

In this work we only consider Abelian gauge fields. However it should be mentioned that schemes also exist for generating non-Abelian gauge fields using laser assisted state sensitive tunnelling [94].

4.1.2 Ground states in an optical lattice

The form of the ground state in the optical lattice potential is highly dependent on a number of parameters. The ratio of optical lattice periodicity d and the magnetic length $\ell_B = \sqrt{\hbar/2M\Omega}$ (reflected in α the number of magnetic flux quanta per plaquette), is an important quantity and determines to what extent the optical lattice modifies the continuum state. The interaction strength U/J and the average number of atoms per lattice site N_s (where $N_s = \rho d^2 = \alpha\nu$, ν being the filling factor) also play an important part. The residual harmonic trapping frequency ω_{eff} also effects the types of states that occur. A summary of these regimes is shown in Figure 4.2, and they are discussed in detail below. In the figure we assume the presence of repulsive interactions, which can lead to the strongly correlated phases indicated.

Single particle regime

Before discussion of the regimes in the presence of interactions, we will address the single particle states in an optical lattice subject to an artificial magnetic field. The energy spectrum forms a fractal structure known as the Hofstadter butterfly [95] due to the periodicity of the optical lattice, which becomes evident for $\alpha \sim 1$. When the number of magnetic flux quanta per plaquette is a rational fraction p/q, the single particle energy band (of width $4J$) splits into q bands. In addition the single particle density distributions close to simple rational fraction p/q show an q-site periodicity [96, 97].

4.2 Mean field regime

4.2.1 Large particle filling: frustrated Josephson-junction arrays

As described in section 1.2.3, when there are many atoms per lattice site we can express the annihilation operator as a c-number, and in the presence of an artificial magnetic field (which we express in the symmetric gauge), the

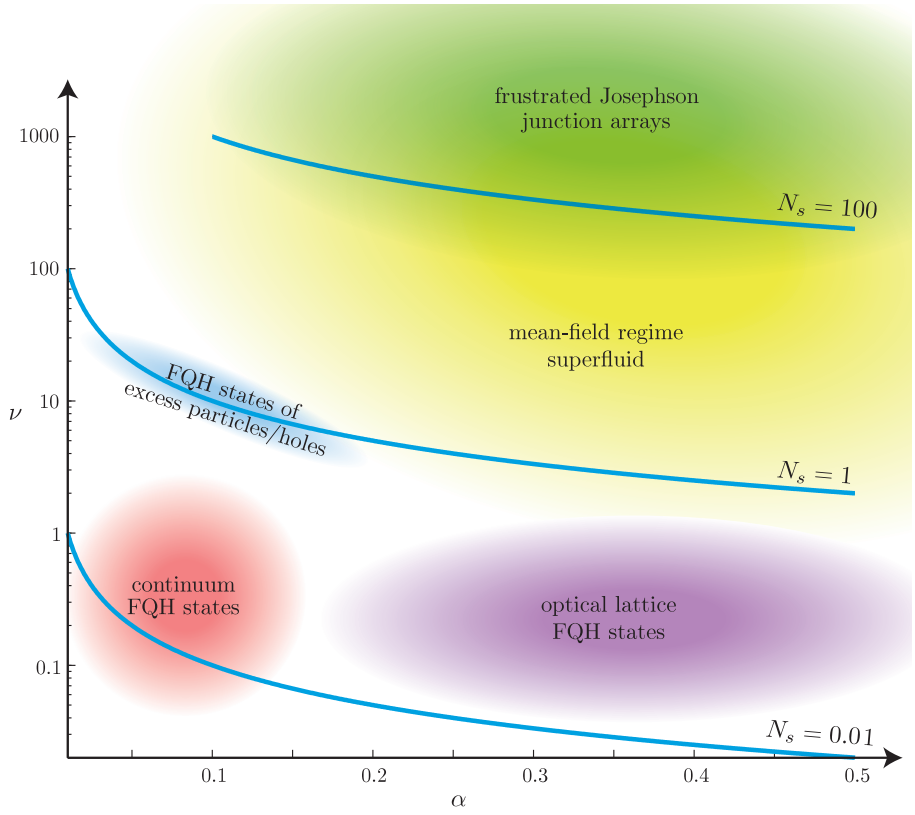

Figure 4.2: Schematic illustrating approximate regions of different phases for atoms in an optical lattice in an artificial magnetic field, as a function of the filling factor ν, the number of atoms per magnetic flux quantum, and α, the number of magnetic flux quanta per lattice plaquette (for repulsively-interacting atoms in the tight-binding regime). The lines plot points with a constant average particle filling per lattice site N_s.

Hamiltonian is given by [98]

$$H = -E_J \sum_{i,j} \cos(\theta_{i,j} - \theta_{i,j+1} - \pi\alpha i) + \cos(\theta_{i,j} - \theta_{i+1,j} + \pi\alpha j), \qquad (4.5)$$

where we take the limit $E_J \gg U$ so that the interaction term can be neglected. This is known as the uniformly frustrated XY model. The system is fully-frustrated when $\alpha = 1/2$, which is illustrated in Figure 4.3. When $\alpha = 1/2$ it is not possible to arrange the phases (shown by green arrows) of each condensate so that the energy is simultaneously minimised for each bond. To understand this, consider the plaquette in Figure 4.3(a) with points

(0,0), (0,1), (1,0) and (1,1). As seen from equation (4.5), the energy on each bond is minimised when the argument of the cosine is zero. Taking the phase to be zero on (0,0), (0,1), (1,0), to minimise the energy on the (0,1) to (1,1) bond requires the phase on (1,1) to be $\pi/2$, whereas to minimise the energy on the (1,0) to (1,1) requires (1,1) to be $-\pi/2$. Instead a compromise is reached, and there are two degenerate ground states shown in Figures (b) and (c) with a complimentary checkerboard pattern of vortices (where a vortex is defined as a 2π phase winding around a plaquette). The phases in these figures are determined from considering the gauge invariant phase differences in the $\alpha = 1/2$ ground state [99]. Ground states for other rational fractions of $\alpha = p/q$ also take the form of a checkerboard of vortices with a $q \times q$ unit cell [98, 99].

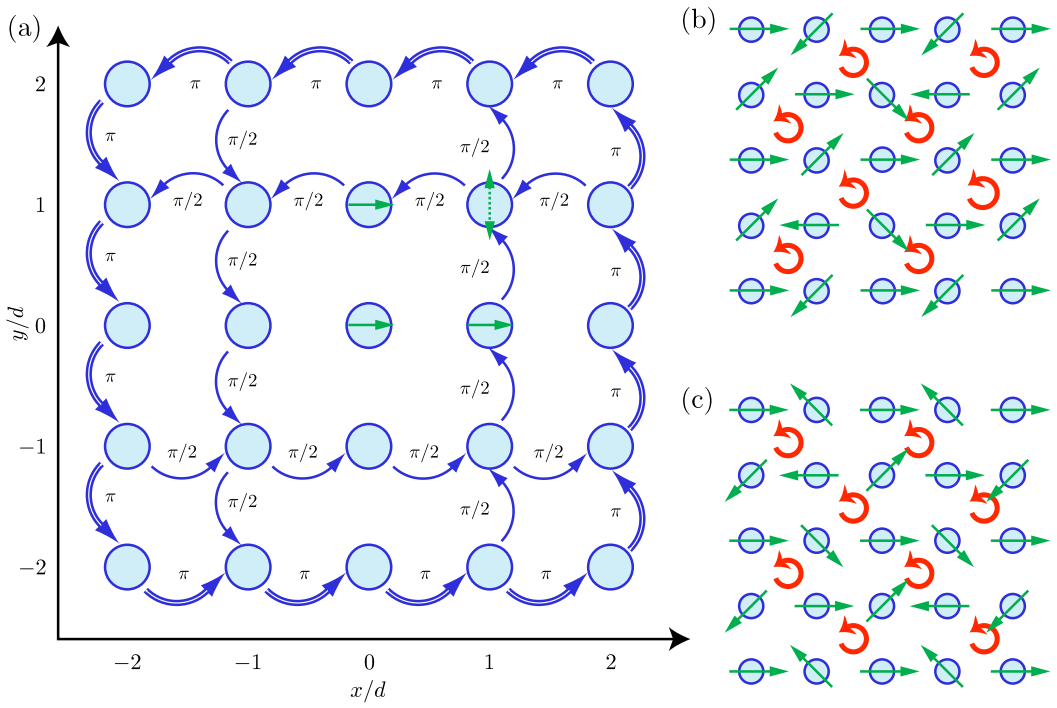

Figure 4.3: (a) Hopping induced phases in the symmetric gauge for $\alpha = 1/2$ given by equation (4.5). It is not possible to simultaneously satisfy the requirement that the wave function is single-valued and to arrange the phases of the wave function (shown by the green arrows) to minimise the energy on all bonds simultaneously. Instead the phases are arranged as shown in (b) and (c). There are two degenerate ground states, with a complimentary arrangement of vortices (marked by red arrows).

In a cold atom system, the number of atoms per site will not be constant due to the external trapping potential, and instead the hopping energy E_J will be site dependent. Calculations carried out for typical experimental parameters show that the ground still displays the characteristic vortex checkerboard in the centre of the condensate, with departures from this pattern towards the edge of the cloud [100].

The fully-frustrated case would be interesting to investigate in a cold-atom system as the phase transition that occurs as the on-site interaction energy is increased is not fully understood. Two types of long-range order are destroyed — the Ising order associated with the broken translation symmetry and the quasi-long-range phase order. It has been proposed that these types of order can be probed by examining the time-of-flight distribution after instantaneous release of the optical lattice [101], although the analysis was carried out for non-rotating systems, with the phase imprinted using the other methods described above (in a rotating system the diffraction peaks will expand by a factor proportional to the rotation frequency).

4.2.2 Experiments in the Josephson-junction regime

We have performed experiments using the optical lattice described in Chapter 2. As described previously, the lattice angle is controlled by the deflection angle of the lattice beams from the AODs. The optical lattice is rotated by modulating the frequency of the RF signal sinusoidally, with a $\pi/2$ phase difference between the x and y crystals. We have published the experimental results in [55] and they are reported in an earlier thesis [48], so only a summary of the main results are given here. Results from mean-field calculations obtained by numerically solving the time-dependent GPE in a rotating frame (see Appendix B for details) are also presented to highlight certain aspects of the experimental results (these were not published in [55]).

As discussed previously, we work in the regime where there are many hundreds of atoms per lattice site, and vary the optical lattice depth V_0/h from 100 Hz to 4 kHz. The chemical potential μ of the BEC in the absence of an optical lattice potential is around $h \times 500$ Hz, and for deep lattices (that is for $V_0 > \mu$), we are working within the Josephson-junction regime.

We start with a combined magnetic and optical trap with harmonic trapping frequencies $\{\omega_r, \omega_z\} = 2\pi \times \{20.1, 56\}$ Hz, and ramp up a stationary optical lattice to the desired lattice depth. The rotation frequency is ramped linearly before holding the rotation frequency at the final value for tens to hundreds of milliseconds. The optical lattice is then ramped down while rotating in 12 ms, allowing the condensates to merge while preserving any phase gradients between separate condensates. The cloud can then be held

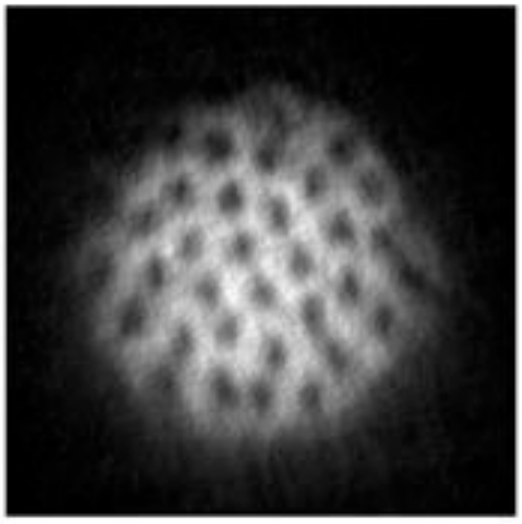

Figure 4.4: Absorption image of a BEC after ramp down of the rotating lattice, 800 ms hold in harmonic trap and 20 ms time-of-flight. The optical lattice was ramped up to $V_0 = h \times 900$ Hz, and rotated at $\Omega/2\pi = 15$ Hz.

in the harmonic trap for up to 1 s before it starts to spin down, and the resulting density distribution imaged using axial absorption imaging after 20 ms time-of-flight. Figure 4.4 shows an example of the resulting density distribution.

Mechanism for vortex nucleation

Figure 4.5(a) shows the number of vortices in the cloud after lattice ramp down as a function of rotation frequency. For the optical lattice with depth $V_0/h = 190$ Hz, the optical lattice potential does not act to break the cloud up into separate condensates, and so the optical lattice acts a 'stirring' potential. As previously demonstrated with other experiments that use stirring potentials to nucleate vortices [102], there is a minimum rotation frequency for vortex nucleation, which corresponds to the minimum frequency at which it is energetically favourable to support a vortex at the centre of the condensate [103].

For an optical lattice depth of $V_0/h = 1.2$ kHz, we see no such minimum nucleation frequency. At this lattice depth, the wave function consists of separate condensates that communicate only by tunnelling. Rotation of the

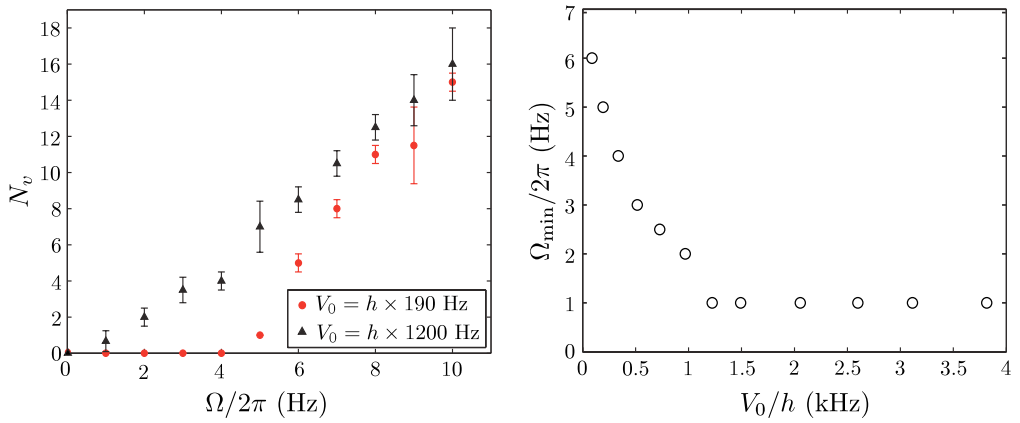

Figure 4.5: Vortex nucleation as a function of lattice depth, plots taken from [55]: (a) Number of vortices as a function of rotation frequency for two different lattice depths. (b) Minimum rotation frequency to nucleate a vortex as a function of lattice depth.

optical lattice leads to the accumulation of phases on the hopping terms, which results in phase differences between the sites. After the lattice potential is ramped down, phase differences of 2π around a plaquette are converted to a vortex in the condensate. There is thus no such minimum rotation frequency for a vortex to enter the condensate.[1] This is further illustrated in Figure 4.5(b), which shows the minimum rotation frequency to nucleate a vortex as a function of lattice depth. As the optical potential increases the minimum nucleation frequency decreases, until the optical lattice potential is deep enough to split the system into isolated condensates (at $V_0 > \mu$). At this point the minimum nucleation frequency drops below 1 Hz (which is the lowest rotation frequency we used).

All our images are taken after the lattice is ramped down in time-of-flight using destructive imaging so we cannot directly probe the mechanism by which vortices enter the system (although we are more likely to find vortices on the edge of the cloud for weak lattices and in the centre of the cloud for deep lattices). We can gain an insight into this mechanism by performing numerical simulations for our experimental parameters.

[1]The minimum frequency to support a vortex will be given by the condition that there is one magnetic flux quantum in the optical lattice, equivalent to $\alpha N_p = 1$, where N_p is the number of lattice plaquettes. For our parameters this gives a minimum nucleation frequency $\Omega_{\min}/2\pi \approx 0.5$ Hz.

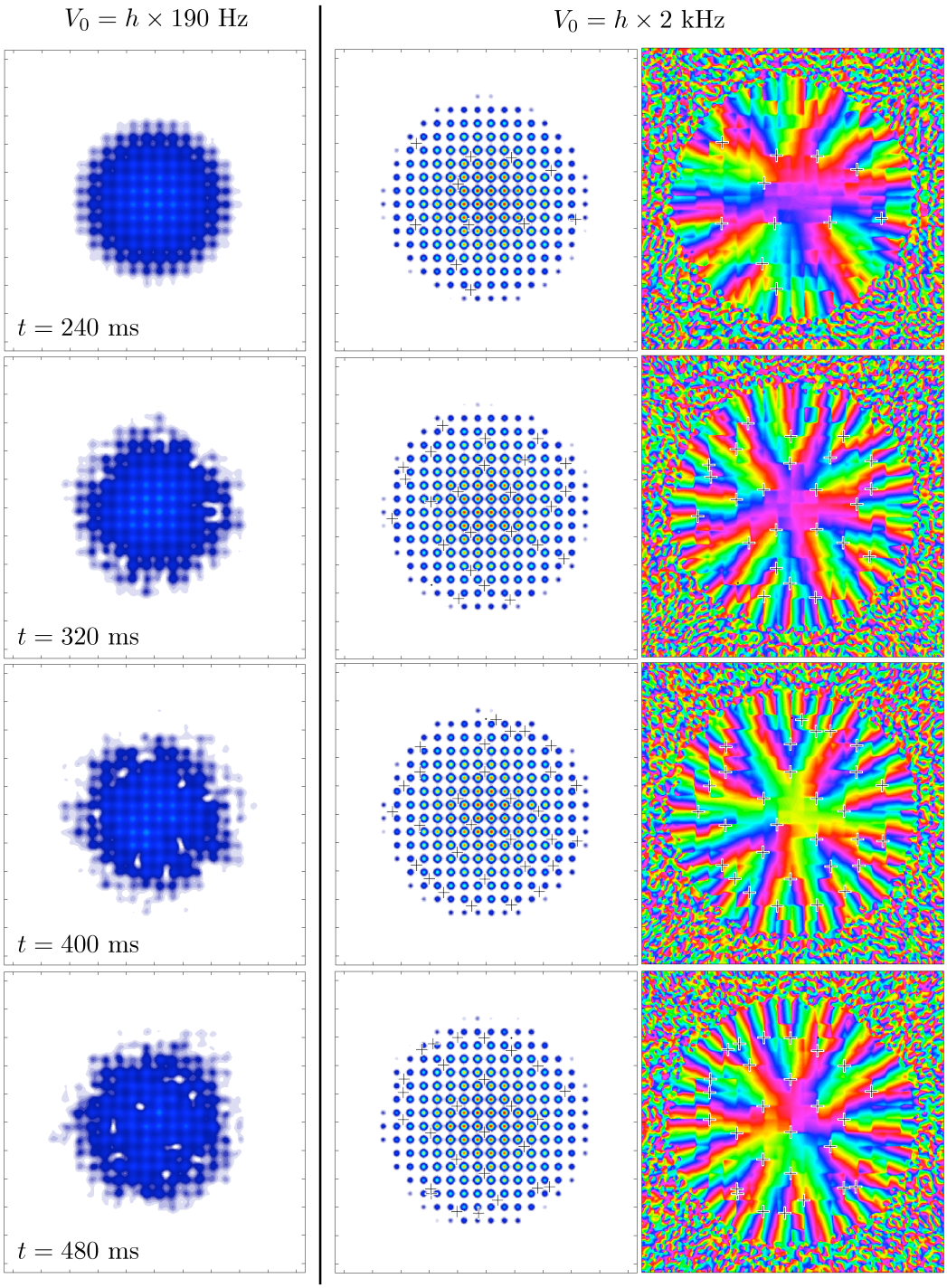

Figure 4.6: Simulations of ramp up of the rotating optical lattice for $\Omega/2\pi = 10$ Hz, $\beta = 1000$. The left column shows the density for a lattice with $V_0 = h \times 190$ Hz. The middle and right columns shown the density and phase respectively for a lattice with $V_0 = h \times 2$ kHz, where the position of the vortices is marked with a '+'. The images are 50 μm $\times$ 50 μm.

Numerical results obtained by solving the time-dependent GPE will now be described. Figure 4.6 shows a series of these results for an optical lattice having $V_0 = h \times 190$ Hz and $V_0 = h \times 2$ kHz, for rotation at $\Omega/2\pi = 10$ Hz. We start with the ground state in a stationary lattice, and ramp up the rotation frequency over 320 ms, before following with rotation for a further 200 ms (in the experimental sequence we rotate for a further 80 ms). The optical lattice potential is then ramped down in 12 ms.

As can be seen for the weak lattice, the vortices enter through the edge of the cloud, and move into the centre. This is in contrast to the case with a deep lattice where the cloud consists of separate condensates. The phase differences between plaquettes build up as the optical lattice is rotated, where the crosses indicate the presence of a 2π phase loop.

Note that although these calculations show a reduction in the minimum frequency to nucleate a vortex as the lattice depth is increased, this occurs for higher lattice depths than we see in the experiment. A possible reason for this is that dissipation is not included in the simulations, however the simulations illustrate qualitatively how vortices enter the system in the different regimes.

Radius as a function of rotation frequency

As described above, reaching the LLL regime requires a precise balancing of the rotation frequency and the harmonic trapping frequency. The LLL regime has been reached in a continuous rotating gas [104], which required $\Omega/\omega > 0.99$. At these high frequencies the system is very sensitive to any anisotropy in the trapping potential, and increasing the rotation frequency further is difficult without the cloud flying apart.

In our experiments with a rotating optical lattice [55] we obtained evidence that in deep lattices ($V_0 = h \times 1.1$ kHz) the radius did not increase as a function of rotation frequency. This was done by monitoring the number of vortices as a function of rotation frequency, which was found to have a linear dependence. Conversely, for intermediate depth lattices ($V_0 = h \times 600$ Hz), the number of vortices rose faster than linearly with rotation speed, indicating an increase in the radius of the cloud. For both lattices we found that Ω/ω could be increased to more than unity, without losing all the atoms from the optical lattice. For the deep lattice, we found that the heating played a large part as $\Omega \gtrsim \omega$, and we could not observe vortices for as high frequencies as with the intermediate depth lattice (in which we could rotate up to $\Omega/\omega = 1.15$). Thus it is instructive to perform simulations in deep lattices at $\Omega \geq \omega$ to learn more about the mechanisms at play in the absence of heating.

Figure 4.7 shows cross-cuts through the density of atoms in an optical lattice rotating at $\Omega/\omega \geq 1$ found by solving the time-dependent GPE. In these

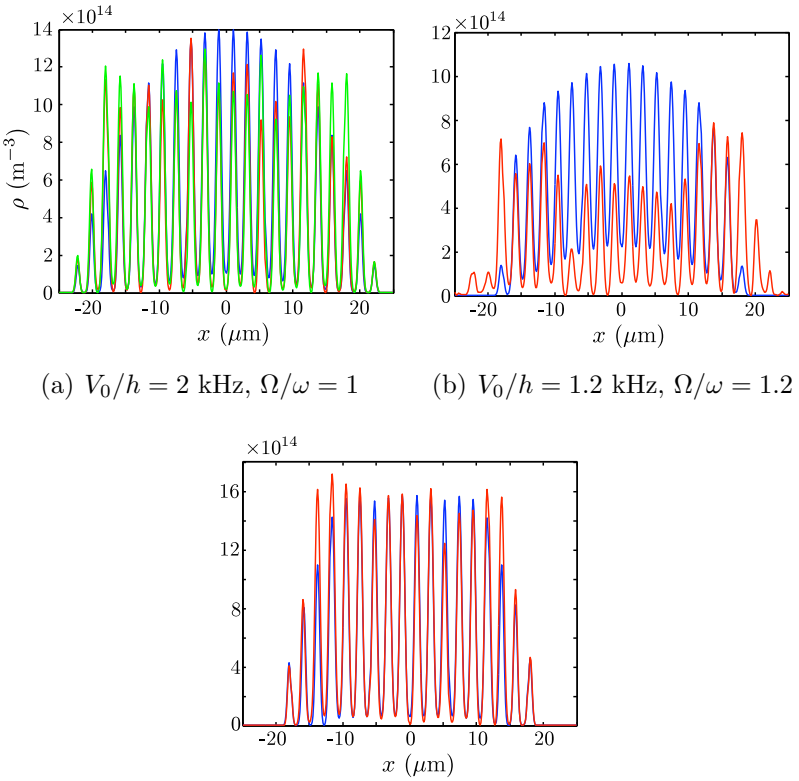

(a) $V_0/h = 2$ kHz, $\Omega/\omega = 1$ (b) $V_0/h = 1.2$ kHz, $\Omega/\omega = 1.2$

(c) $V_0/h = 2.4$ kHz, $\Omega/\omega = 1.2$

Figure 4.7: Simulation results showing a cross-cut through the density for an optical lattice rotating at $\Omega/\omega \geq 1$. The blue line denotes $t = 0$, the red line denotes $t = 240$ ms, the green line denotes $t = 2.4$ s. In (a) and (c) the radius is unchanged and all the atoms remain trapped in the optical lattice. In (b), around 85% of the atoms remain trapped. $\beta = 2000$ for all figures (see Appendix B).

simulations we have not included the Gaussian trapping envelope of the optical lattice, so that the harmonic trapping frequency (in the lab frame) has the same magnitude for all lattice depths. In (a) we examine the case of a weak lattice rotating with an angular frequency exactly matched to the harmonic trapping frequency. In the corotating frame, the external potential will be precisely zero. We see no expansion of the cloud, even for times comparable to the single particle tunnelling time (for these parameters, $J/h \sim 1$ Hz). Although the radius is unchanged, the density profile is altered: the density in the centre of the cloud flattens, and the cloud develops steep edges. This is characteristic of that seen for self-trapping in other Josephson-junction experiments [105]. Self-trapping occurs when the repulsive-interaction energy

reaches a critical value, and the population imbalance between two neighbouring sites becomes self-locked [106].

The simulations show that the self-trapping acts to contain the cloud even when $\Omega/\omega > 1$, although for $V_0 = h \times 1.2$ kHz, 15% of the atoms are lost from the optical lattice. Thus for the case of interacting particles, the optical lattice can act to prevent expansion of the cloud for large rotation frequencies. Note that this effect can have undesirable consequences, since the system will not be able to reach the ground state if it cannot evolve to the equilibrium size for the effective trapping potential in the rotating frame.

For fewer atoms (and thus a smaller interaction energy), we would not expect to see self-trapping. An interesting question for further study is the extent to which other mechanisms, for example Bloch oscillations, act to stop expansion of the cloud for $\Omega/\omega > 1$.

Frustration

As described above, the system is fully frustrated at $\alpha = 1/2$ and the ground state consists of a checkerboard vortex pattern. Given the flexibility of our optical lattice potential, which allows us to vary the optical lattice periodicity as well as the rotation frequency, we attempted to investigate frustration effects by examining the pattern of vortices after ramp down of the optical lattice. Unfortunately we were unable to reliably generate square arrays of vortices. There are many possible reasons for this, some of which are technical in nature, and others which relate to the physical nature of these systems.

One limitation is the relatively large lattice spacing that is required to reach large values of α for the rotation frequencies we use. To reach $\alpha = 1$ requires a lattice spacing of 4.7 μm for a rotation frequency of $\Omega/2\pi = 16$ Hz. For these parameters, and a lattice depth $V_0/h = 2$ kHz, the Josephson tunnelling energy is $E_J/h < 1$ Hz. A previous experiment [107] probed pinning of vortices with a weak rotating optical lattice generated using a rotating mask (mechanical instabilities limited the depth of the optical lattice to $\sim 30\%$ of the chemical potential of the cloud). Pinning of the vortices to the maxima of the optical potential was observed at $\alpha = 1$, causing a transition from the Abrikosov triangular lattice [108] (the ground state in a rotating gas with no optical potential) to a square lattice.

Figure 4.8 shows simulation results for the parameters given above, in both the weak pinning regime ($V_0 = h \times 200$ Hz) and the deep lattice regime ($V_0 = h \times 2$ kHz) after the rotation frequency is ramped up over 320 ms, and the optical lattice rotated for 400 ms. In the weak pinning regime, a square lattice (with one defect) is observed. For the deep lattice, however, the weak

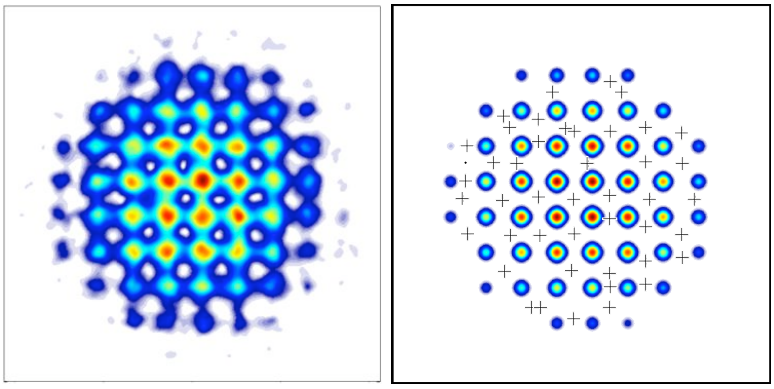

(a) $V_0 = h \times 200$ Hz (b) $V_0 = h \times 2$ kHz

Figure 4.8: Simulation results for a rotating lattice for $\alpha = 1$ for two different lattice depths, $\beta = 1000$. The positions of the vortices are marked with a '+' in (b). The images are 50 μm $\times$ 50 μm.

coupling between the lattice sites has prevented the system from reaching the ground state.

Of course for rational fractions of α the lattice spacing can be decreased, so increasing the tunnelling amplitude. Figure 4.9 shows simulation results for the case of $\alpha = 1/3$, with $d = 2.6$ μm and for rotation frequency of $\Omega/2\pi = 17.5$ Hz. The Josephson tunnelling energy is $E_J/h \sim 100$ Hz for $V_0/h = 2$ kHz. The checkerboard vortex array is not present for either the weak pinning potential of the deep optical lattice.[2]

The difficulty in reaching the ground state may be due to the energy landscape having a glassy nature in the presence of artificial magnetic fields, where many metastable states are present as a result of frustration effects. For example in studies which have numerically calculated the ground state, many runs need to be taken with different start states in order to reach the true ground state [109, 100]. The excitations of these ordered states also have small energy gaps: the $\alpha = 1/2$ state has two distinct types of thermal excitation [99]: interstitial vacancy pairs may be excited, which does not affect the long range order, or domain walls may be excited which separate regions of different chirality. Both of these excitations would make it difficult to discern long-range order in the arrangement of the vortices.

In a theoretical study which examined the evolution of vortex lattice

[2]As before, we do not take dissipation into account, which would probably show increased order for a given rotation time. Nevertheless, these simulations indicate how difficult it is to reach the true ground state while ramping up a rotating lattice.

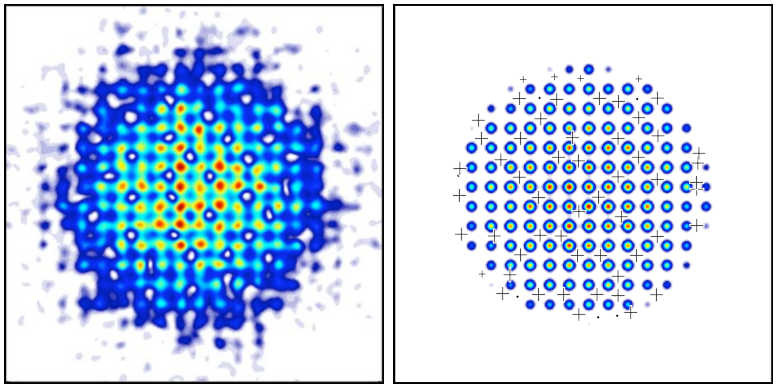

(a) $V_0 = h \times 200$ Hz (b) $V_0 = h \times 2$ kHz

Figure 4.9: Simulation results for a rotating lattice for $\alpha = 1/3$ for two different lattice depths, $\beta = 1000$. The positions of the vortices are marked with a '+' in (b). The images are 50 μm $\times$ 50 μm.

structures as the rotation frequency is ramped up for systems with low particle filling [110], it was found that competition between the vortex-vortex interaction and lattice pinning leads to hysteretic evolution, with multiple vortices entering at once. Ring-type structures, rather than the ground state square structures, were observed as the rotation frequency was ramped up, although for large rotation frequencies a domain of a square vortex array appeared in the centres. However, the systems treated in this study are a lot larger than we can currently reach in the experiment (30 to 60 sites filled along each direction).

Even given these difficulties, we have not been able to reproducibly observe a square array with a weak pinning potential at $\alpha = 1$, which has been observed in a previous experiment [107]. This may be due to other limitations of the experiment. For example, the extent of the cloud in the axial direction is still large enough to allow the vortex lines to bend, thus changing the nature of the vortex lattice states. In addition, technical limitations such as heating caused by the imperfections in the optical lattice potential will also limit the ability to reach the ground state in the system.

The other regimes shown in Figure 4.3 that are encountered as N_s is decreased will now be described. These regimes are not currently achievable with our experimental parameters, and we will conclude by discussing how one might reach the strongly correlated regime.

4.2.3 Mean-field states at low and intermediate filling

As the optical lattice filling is decreased, the system can no longer be treated as a Josephson-junction array. However, the system is still in the mean-field regime for $\nu \gtrsim 10$ and theoretical studies have been carried out to explore the superfluid regime for α close to a rational integer p, q. The form of the vortex lattice has been investigated for $\alpha \approx 1/2$ for a filling factor $\nu \approx 20$ (i.e. with an average of 10 atoms per lattice site) using the Gutzwiller ansatz [111]. It was found that the system behaves as a two-component superfluid with the two components of the wave function forming alternating stripes of a vortex lattice phase. In general, for $\alpha = p/q$, the system behaves as a q component superfluid.

The superfluid phase has also been theoretically treated for an average filling of ~ 1 atom per lattice site, in the region where these phases will be in competition with strongly correlated phases [112, 113], also concentrating on $\alpha = p/q$. A modulation of the density distribution in the superfluid phase is predicted, and it is found that the quasiparticle excitation spectrum reflects the Hofstadter spectrum.

4.3 Strongly correlated states

As the number of magnetic flux quanta is increased and becomes comparable to the number of atoms in the system, the vortex lattice melts to form a strongly correlated state. This is known as the fractional quantum Hall (FQH) regime. In a continuum system, it has been predicted that the vortex lattice will melt at $\nu \lesssim 6$ [114] (in our experiment $\nu \sim 10^5$).

The FQH effect was first discovered in a two-dimensional electron system, where plateaux in the resistivity where observed at fractional filling factors ν [115]. While the integer quantum Hall effect could be understood by considering the Landau level structure, the fractional quantum Hall effect can only be explained by taking into account strong correlations between the electrons. A wave function for the ground state at $\nu = 1/m$ which explained the features of these states was proposed by Laughlin [116]:

$$\psi_{\mathrm{L}} = \prod_{i<j} (z_i - z_j)^m \, \exp(-\sum_i |z_i|^2 / 4\ell_B^2), \tag{4.6}$$

where $z_i = x_i + \mathrm{i}y_i$ is the complex co-ordinate. This state has excitations with a fractional charge e/m. For electrons, m is odd, which satisfies the requirement that the wave function is anti-symmetric upon exchange. It has been predicted that bosonic analogues of these states are present in cold

atom systems in the presence of artificial magnetic fields [114]. For bosonic atoms, the wave function should instead be symmetric upon exchange, and it is found that in a rotating system the Laughlin wave function is the ground state for $m = 2$ [117]. As well as the Laughlin state, many other fractional quantum Hall states are predicted to occur for increasing values of ν [23].

Evidence for the presence of FQH states in a continuous bosonic system [118] has recently been demonstrated. Each site of an optical lattice formed an isolated system of around five atoms per lattice site. Evidence of a strongly correlated state was found by looking at atom losses as a result of photoassociation: a reduced probability of photoassociation is evidence of a strongly correlated state where the atoms seek to avoid one another.

The FQH states predicted to form in an optical lattice will now be briefly discussed. A numerical study of these states is presented in Chapter 7.

4.3.1 Continuum FQH regime

When $\alpha \ll 1$, the magnetic length ℓ_B is much larger than the optical lattice spacing, so the periodicity of the lattice does not have a large influence of the ground state. The states in the optical lattice are the same as those in the continuum, with the mass replaced by the effective mass in the optical lattice [96].

Exact diagonalisation of the Hamiltonian for small numbers of atoms in periodic boundary conditions for both hard core bosons [93] and finite interaction [119] have shown that a discretised Laughlin wave function is a good description of the ground state up to $\alpha \lesssim 0.2$.

4.3.2 FQH effect near Mott insulator transition

In the absence of an artificial magnetic field, there is a phase transition from a superfluid to a Mott insulator (MI) state in an optical lattice as the lattice depth (and therefore U/J) is increased [16] and this has been observed experimentally [17]. In a rotating optical lattice, the interplay between the MI state and the FQH states could be investigated. In one numerical study [120], the MI phase in an artificial magnetic field was studied, with a deviation $\epsilon = 1 - Ns$ of the filling from unity was commensurate with the number of magnetic flux quanta. This formed FQH states of excess particles/holes, which would be visible as extra steps in the density profile near the MI plateaux.

4.3.3 High field FQH regime

As the magnetic length ℓ_B becomes comparable to the optical lattice periodicity, the effect of the optical lattice becomes important, causing the ground state to be modified. This is a regime that cannot be reached in condensed matter systems, so would be of particular interest to investigate with ultracold atoms in optical lattices.

In an analytical study [96] it was predicted that at $\alpha \approx p/q$ the system would be analogous to a q-layer quantum Hall system, with different components of the wave function forming different layers. Another theoretical study modelled the wave function using a composite fermion description that does not have a counterpart in the continuum limit [121]. The trial wave functions are compared with the ground state found by exact diagonalisation, giving large overlaps.

In one study [122], it was found that by including tunnelling terms beyond nearest-neighbour, the Laughlin wave function would remain a good description of the ground state even for large values of α (at $\nu = 1/2$).

4.3.4 Reaching the strongly correlated regime in a rotating optical lattice

As described above, evidence of the FQH states has been observed in small continuous systems. The FQH regime has not yet been reached for systems with a large number of atoms in an optical lattice. Some of the experimental requirements and challenges to reach this regime will now be discussed.

Lattice parameters

In our experiments with the rotating lattice, the minimum lattice spacing we could achieve was ≈ 2 μm. This lattice spacing results in acceptable tunnelling energies and experimental time-scales when there were many hundreds of atoms per site. However, to reach the FQH regime requires a dilute system, and the single particle tunnelling time is not within a typical experimental time scale. In addition, in a large period lattice the on-site interaction energy, which sets the energy scale in the system, is small. It would thus be desirable to move to a smaller period lattice, which could be implemented using our experimental arrangement with a higher NA lens in combination with a blue-detuned lattice. For example, a lattice formed of light at 532 nm using an objective lens of 0.5 NA would have a lattice spacing of 0.53 μm.[3]

[3]This is experimentally feasible - recent experiments [26] have utilised an objective lens outside the cell with an NA of 0.68 and a working distance of 13 mm.

Magnetic field strength

The FQH regime occurs when the number of magnetic flux quanta is comparable to the number of atoms in the system. In the continuum limit we also require $\alpha \ll 1$. Taking $\nu = 1/2$, and $\alpha = 0.1$ leads to the condition that there should be an average filling of one atom every 20 lattice sites, or a 2D number density of $\rho = 2 \times 10^7$ cm^{-2}, and a rotation frequency $\Omega/2\pi = 150$ Hz. The requirement for such a low density is challenging, and for a typical sized system would mean there were ~ 100 atoms. The signal for such a small number of atoms could be improved by moving to a multi-layer geometry [123].

To reach the high field quantum Hall regime e.g. for $\alpha = 1/2$, would mean that there should be five times more atoms, thus improving the signal, but also a rotation frequency five times larger. Although in principle our rotating optical lattice can reach frequencies as high as ~ 1 kHz, it is unclear how large a role heating would play. These high frequencies would need to be balanced by a harmonic trapping potential, which would be possible using an optical trap [124].

Temperature

Another difficulty in reaching the FQH regime is the extremely low temperatures required. For comparison, the lowest temperature of a BEC attained is 500 pK [125].

In the continuum regime, the temperature must be less than the gap to the next excited Landau level, which is given by $2\hbar\Omega/\bar{m}$, where $\bar{m}$ is the ratio of effective mass to free mass m^*/m, which for typical parameters is more than one. For the parameters given above this leads to temperatures which are tens of nanokelvin, which should be experimentally feasible. Another limit on temperature is the energy to create anyonic excitations. The quasiparticle-quasihole pair creation gap is of order $Um\Omega d^2/h$ [111]. Interaction energies of order kHz can be created by applying a tight axial lattice to the system, resulting in temperatures of the order of a few to tens of nanokelvin.

The enhanced interaction energy in an optical lattice leads to larger energy scales than in the continuum thus making these states easier to reach experimentally. In addition, to reach the required temperatures, methods proposed for cooling in the lattice could be employed [126, 127].

Effective trapping frequency

Precise balancing of the trap frequency and rotation frequency is needed to reach the Laughlin state. If the effective trapping frequency becomes too

large, the energy of a particle at the edge of the system becomes larger than the interaction energy needed to create a particle at the centre. This leads to the relation $\Omega/\omega \geq 1 - UMd^2/2\pi\hbar^2 N$ [111], and for $U = 1$ kHz and $N = 100$, the result is $\Omega/\omega \geq 0.997$ for $d = 0.5$ μm. As the residual trapping frequency is raised further, a stepped structure of FQH states will occur [123].

Balancing the rotation frequencies so precisely can be problematic, as any small residual trap anisotropy will cause the atoms to fly out. As described above, using an optical lattice may add an additional confinement, which should make it easier to match the frequencies closely. In addition, a theoretical study has found that the presence of a quartic term in the residual trapping potential may make the Laughlin state easier to access [128]. The Gaussian-trapping envelope of a blue-detuned lattice will include a quartic term, or alternatively an external potential having a quartic term, such as a shell trap generated using RF dressed potentials [129], could be used.

Adiabatic path to FQH states

As described above with relation to Josephson-junction arrays, reaching the ground state by ramping up the rotation frequency can be difficult due to the complicated energy landscape. Ramping up the rotation frequency to reach the Laughlin state has been investigated theoretically by exact diagonalisations of a continuous system of up to four atoms [130]. It was found that reaching these highly-entangled states is also non-trivial, and an adiabatic path is calculated from an exact knowledge of the spectrum (which is only possible for small numbers of atoms).

Reaching these states in an optical lattice will also be non-trivial. One proposed scheme to reach these states is to start with a MI state in an optical superlattice potential before ramp up of the magnetic field [93]. After the magnetic field is ramped up, the long wavelength part of the superlattice potential is decreased, melting the MI to arrive at the Laughlin state.

Detecting strongly correlated states

The low densities required to reach the FQH regime mean that it is not possible to image a single system with absorption imaging. In the recent experiment [118], this was addressed by having several thousand systems, and taking an absorption image of the sum of all the systems. It has also been proposed that several isolated layers of FQH states can be imaged together, where cusps in the density profile indicate the presence of a stepped structure of FQH states in each layer [123].

With the recent progress in single-atom fluorescence imaging in optical

lattices [26, 25], the distribution of atoms in a single system could also be probed directly. The accordion lattice described in Chapter 2 could be used to first 'magnify' the system and thus more easily probe the configuration of atoms. By averaging the data over many shots, the density and two-point correlation function (which have a distinctive form for the Laughlin state described in Chapter 7) could be deduced. When single-atom fluorescence imaging is used, the parity rather than the number of atoms per lattice site is measured due to light-assisted collisions. Atom losses due to these collisions could be used in a similar way to [118] to probe the presence of a strongly correlated state, although for low filling the signal would be small.

It has been proposed that an additional small periodicity imaging lattice can be used after an accordion lattice has been expanded, to trap multiple atoms in a site of the accordion lattice into separate sites of the imaging lattice, and thus count the number of atoms per lattice site [131, 132]. An imaging system such as this could even be used with an experiment having multiple rotating puddles [118] to image the distribution in a single lattice site. Note that for this detection mechanism to be successful, the expansion time of the optical lattice must slow enough that the ramp is adiabatic with respect to the quantum Hall gap.

Chapter 5

Correlator product states

The remainder of this thesis will be concerned with the numerical description of strongly correlated states. In contrast to weakly-interacting systems, which we have been able to model well using the mean-field description of the GPE earlier in this thesis, strongly correlated states are extremely challenging to simulate numerically. However, many interesting effects, for example high-temperature superconductivity and the fractional quantum Hall effect, occur as a result of strong correlations between particles. The difficulty in numerically simulating these systems is one of the motivations for building 'quantum simulators' using atoms in optical lattices to probe the properties of these states.

Although challenging, developing tools to study these states numerically can be useful for improving our understanding of them, and for calculating the regimes that would be required to access these states experimentally. There has been a lot of success using a tensor network description of these systems to capture their most important properties [133]. These techniques have been used to describe large (i.e. comparable with experimental sized) systems in one dimension, but the scaling of the computational effort with system size for two-dimensional systems is poor and as such most calculations have been limited to small system sizes.

Recently a new technique has been proposed for simulating lattice systems: so-called correlator product states [134] or entangled plaquette states [135] (the descriptions are equivalent and they will hereafter be referred to as correlator product states (CPS)). These show promising results for numerical simulation of two-dimensional systems. An overview of tensor-network descriptions, and the CPS representation and minimisation method is given in this chapter. Results using the CPS representation for the 2D quantum Ising

model are described in Chapter 6, and to the Bose-Hubbard Hamiltonian in a magnetic field in Chapter 7.

5.1 Strongly correlated states

5.1.1 Hilbert space size

Modelling strongly correlated states exactly for more than a few atoms is not possible, due to the rapid increase in the size of the Hilbert space with the number of particles. In a spin system with d-dimensional spins, the size of the Hilbert space grows as d^N, where N is the number of spins. For a system of N bosons in an $L \times L$ optical lattice, the size of the Hilbert space grows as

$$\frac{(N + L^2 - 1)!}{N!(L^2 - 1)!}.$$

A typical desktop computer can store a local Hamiltonian for around one million basis states, while even a 'small' system size by experimental standards of $L = 20$, $N = 50$ has $\sim 10^{67}$ states.

Even though the full Hilbert space for systems of a realistic size is extremely large, numerical methods which utilise only a small portion of the Hilbert space are able to accurately reproduce much of their behaviour. This is because the ground and low-lying excited states of these systems have certain properties (which will be discussed in more detail below) which restrict them to a submanifold of the Hilbert space, with the remainder or the space being unphysical. This can be understood by considering the entanglement in the system.

5.1.2 Entanglement scaling

When considering the properties of the types of states that occur in nature, we see that physical systems usually have local Hamiltonians i.e. the interactions are short-range and between only a few of the atoms. These local properties are reflected in the ground-state of the system, although the ground-state may also exhibit global properties due to the competition in simultaneously satisfying the local constraints for all particle pairs in the system. These local properties lead to two connected effects: the first of these is related to the entanglement entropy S_L of the system, and the second to the correlation length ξ [136].

The Von-Neumann entropy $S_L = -Tr(\rho_L \log_2 \rho_L)$, where ρ_L is the reduced density matrix in an L^n block (where L is the length of one dimension

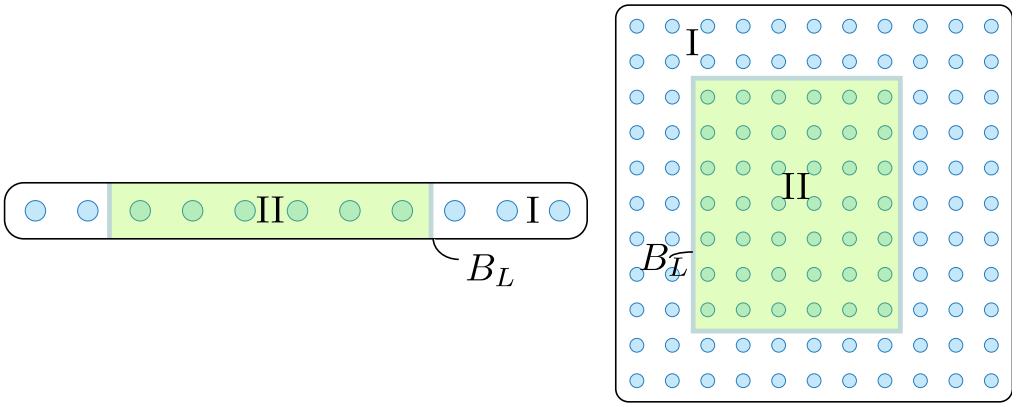

Figure 5.1: Illustration of the area-law for entanglement scaling. In a 1D system the entanglement entropy between region I and II scales with the size of the boundary B_L and so saturates with the size of the region II. In a 2D system the entanglement entropy between region I and II scales with the length of the boundary B_L.

of the block and n is the dimension of the system), quantifies the degree of entanglement between the block and the rest of the system. A random state has largest possible entanglement, and the entanglement entropy scales with the volume of the system. However, this state is not only unphysical, but is inaccessible from the ground-state in a realistic time-scale [137].

For most physical systems the entanglement entropy scales with the size of the boundary L^{n-1}, rather than with the volume of the system within the boundary, i.e. the system obeys an area law. This is illustrated in Figure 5.1. For one-dimensional spin systems, the entanglement is well-understood and the entanglement entropy saturates for off-critical systems and scales as $S_L \propto \ln(L)$ for critical systems [137] i.e. there is a logarithmic correction to the area law for critical systems. In two dimensions, there is not the same general formula but systems are expected to obey an area law with only logarithmic corrections at criticality, so the entanglement is still much smaller than for a random state. For topological states such as the FQH states the entanglement scaling is well known [138]: for these states the entanglement entropy scales as $S_L = aB_L - \gamma + O(1/B_L)$, where B_L is the boundary length of a smooth disk, a is a constant, and γ characterises the topological order of the state. For a FQH state with $\nu = 1/m$, the topological order is characterised by $\gamma = \ln\sqrt{m}$.

The adherence to an area law can be related to the correlation length: when the correlation function decays exponentially (as for off-critical gapped

systems), the entanglement is concentrated on the boundary. In critical systems where the correlation function decays as a power-law, this leads to the logarithmic corrections to the entanglement scaling.[1]

5.1.3 Tensor network description of many body states

The tensor network formulation is successful because it exploits the properties described above i.e. the set-up makes it straightforward to work in the physical parts of the Hilbert space. As well as providing a natural framework to describe the system, efficient methods for finding the ground-state [140, 141] and time-evolving these states [142] have also been developed.

Matrix product states in one dimension

A general state is given by the wave function $|\psi\rangle = \sum_{\mathbf{s}} W(\mathbf{s})|\mathbf{s}\rangle$, where $W(\mathbf{s})$ is the probability amplitude, which we refer to as the weight of a given configuration $\mathbf{s}$ (since we will later use $W(\mathbf{s})$ to provide a weighted sum for expectation values). The matrix product state (MPS) representation (for open boundary conditions) is

$$|\psi\rangle = \sum_{\mathbf{s}} \langle L|\mathbf{A}^{[1]s_1}\mathbf{A}^{[2]s_2}\cdots\mathbf{A}^{[N]s_N}|R\rangle|\mathbf{s}\rangle, \tag{5.1}$$

where $\mathbf{A}$ is a χ by χ matrix labelled by the site i and the configuration on that site s_i, and $|L\rangle, |R\rangle$ are suitably chosen boundary vectors [143, 137]. The weight $W(\mathbf{s})$ for each configuration is thus given as a product of the relevant matrices $\mathbf{A}^{[i]s_i}$ for that configuration. The matrix product state description is exhaustive, and to represent a general state by an MPS requires a dimension χ equal to half the dimension of the entire Hilbert space of the system. However, the reason they are useful is that many states can be very well approximated by an MPS description with the dimension χ much smaller than the Hilbert space size: for states that obey the area law the number of parameters needed scales polynomially with N [144]. In these systems the entanglement entropy scales with the boundary size (which is invariant with the block size), and so it is clear that the MPS representation obeys the area law, where the bond dimension χ required to accurately reproduce the state depends on the degree of entanglement in the system. A system that contains no entanglement can be described by a product state (i.e. $\chi = 1$,

[1] Note that for systems to satisfy an area law does not always require an exponentially decaying correlation length. Some systems that have an algebraically decaying correlation function (e.g. systems with a long-range interactions) still obey an area law [139].

which is equivalent to mean-field theory), and typically $\chi < 1000$ is used in a realistic calculation.

Calculation of expectation values is carried out by connecting 'bonds' in a tensor network, which is equivalent to contracting virtual indices (of dimension χ) and physical indices (of dimension d) by a series of matrix multiplications. Matrix product states are efficiently contractible in one dimension — to contract according to the underlying lattice structure involves multiplication of the matrices $\mathbf{A}$ from left to right, and scales as $Nd^2\chi^3$ for open boundary conditions ($Nd^2\chi^5$ for periodic boundary conditions).

Extensions to two dimensions

Matrix product states can be extended to two dimensions using projected entangled pair states (PEPS) [145, 146], which can be viewed as virtual systems of pairs of maximally entangled states that are locally projected onto the physical dimension d. Like MPS in one dimension, PEPS in two dimensions also obey an area law by construction, as the number of bonds across a boundary scales with the length of the boundary. Unlike MPS, they are not efficiently contractible. The contraction procedure is performed row by row, and the computation effort scales as χ^{2L}, where L is the number of rows. Recently a procedure for performing PEPS simulations using Monte Carlo sampling has been proposed, and it shows promising results for treating large bond dimensions [147].

Another approach to represent two-dimensional systems are string bond states [148]. Here the state is represented as a product of 'strings', where each string is represented by an MPS, and the ground-state can be found using variational methods essentially identical to those considered here.

5.2 Correlator product states

Correlator product states can be thought of as a simple form of tensor network states, where correlations between sites are encoded explicitly so that the amplitude for each wave function is given by a product of scalars. The construction means that it is relatively straightforward to find the ground-state using variational methods. The method has been applied to calculate energies in the spin-$\frac{1}{2}$ antiferromagnetic Heisenberg model on a square lattice of up to 10×10 spins [134, 135] and on a triangular lattice of up to 324 sites [149], the Fermi-Hubbard model [134, 150] and the frustrated $J_1 - J_2$ quantum spin Hamiltonian [135]. In all cases the energies found compared well with those found using other methods (e.g. PEPS, MPS, stochastic series

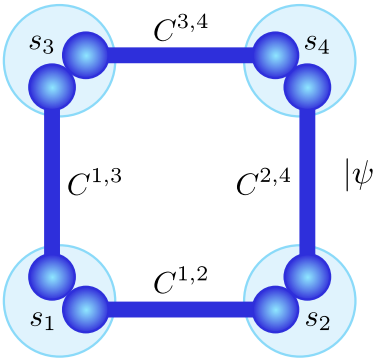

$$|\psi\rangle = \sum_{\mathbf{s}} C^{1,2}_{s_1,s_2} C^{1,3}_{s_1,s_3} C^{2,4}_{s_2,s_4} C^{3,4}_{s_3,s_4} |s_1, s_2, s_3, s_4\rangle$$

Figure 5.2: Illustration of the CPS ansatz for a simple 2 by 2 system with open boundary conditions.

expansion).

In [135] and [149] the spin-spin correlation is also calculated for the farthest point out in the lattice. The results are compared with a stochastic series expansion in [135], and a reasonable agreement is found.

We apply the correlator product description to two systems. The 2D quantum Ising model, described in Chapter 6, and bosonic atoms in optical lattices subject to artificial magnetic fields, described in Chapter 7.

5.2.1 Representing the wave function

In the correlator product state description, the weight $W(\mathbf{s})$ of a given configuration $\mathbf{s}$ is given by the product of correlator elements $C^{\{i\}}_{s_{\{i\}}}$ over the lattice

$$W(\mathbf{s}) = \prod_{\{i\}} C^{\{i\}}_{s_{\{i\}}}, \tag{5.2}$$

where each correlator element is a c-number that describes the amplitude of a configuration $s_{\{i\}}$ of a subgroup of sites $\{i\}$. This is illustrated in Figure 5.2, for the case where the subgroup of sites is a nearest neighbour pair i.e. 'bond' correlators.

Consider that the states s_i in the Figure are those of a spin-$\frac{1}{2}$ system. Each correlator $\mathbf{C}^{i,j}$ represent the amplitudes for different configurations of spins on two sites i, j.

$$\mathbf{C}^{i,j} = \begin{pmatrix} C^{i,j}_{\uparrow\uparrow} & C^{i,j}_{\uparrow\downarrow} \\ C^{i,j}_{\downarrow\uparrow} & C^{i,j}_{\downarrow\downarrow} \end{pmatrix} \tag{5.3}$$

The four-site system will have a total of sixteen basis states, and the weight for an example basis state $W(\uparrow\downarrow\downarrow\uparrow) = C^{1,2}_{\uparrow\downarrow} C^{1,3}_{\uparrow\downarrow} C^{2,4}_{\downarrow\uparrow} C^{3,4}_{\downarrow\uparrow}$.

The wave function in the CPS representation is given by

$$|\psi\rangle = \sum_{\{s\}} \prod_{\{i\}} C^{\{i\}}_{s_{\{i\}}} |s_1 \cdots s_L\rangle. \tag{5.4}$$

The wave function can also be given by a projection onto a subset of the basis states if, for example, the total atom number or spin is conserved:

$$|\psi\rangle = \sum_{\{s\}} \prod_{\{i\}} C^{\{i\}}_{s_{\{i\}}} \hat{P}_N |s_1 \cdots s_L\rangle. \tag{5.5}$$

This description can be extended to any form of correlator e.g. each correlator could represent four sites in a plaquette, or a string of a given number of sites. One advantage of using correlator product states is that the wave function amplitude is a simple product of c-numbers, so any arrangement of correlators between sites can be used without affecting the complexity of the calculation.[2] Thus, the type of correlator can be chosen to best match the properties or symmetries of the system, as will be discussed in subsequent chapters.

5.2.2 Relation to matrix product states

Correlator product states are exactly equivalent to matrix product states for the case where 'bond' correlators are used, and where the dimension of the matrices is equal to the physical dimension [134]. We will now discuss this equivalence, for the benefit of readers who are familiar with matrix product states, but it is not directly relevant for what follows.

Correlator product states can be thought of as a special class of matrix product states that can be factorised using the copy tensor. This is illustrated in Figure 5.3(a), where the copy tensor is illustrated with a black dot, while the large circle represents a matrix formed of the correlator elements as given in equation (5.3). The copy tensor has one input (the physical leg) and multiple outputs (two for the case of bond correlators in one dimension). The copy tensor acts by taking the value of the physical leg in one basis (e.g. $|\uparrow\rangle$ or $|\downarrow\rangle$) and copying it to all its legs.

[2] As will be explained in section 5.3.1, the computational effort scales with the number of sites covered by each correlator, and the number of correlators covering each site. It does not depend on the actual geometry of the correlators e.g. whether the correlators are for strings or plaquettes.

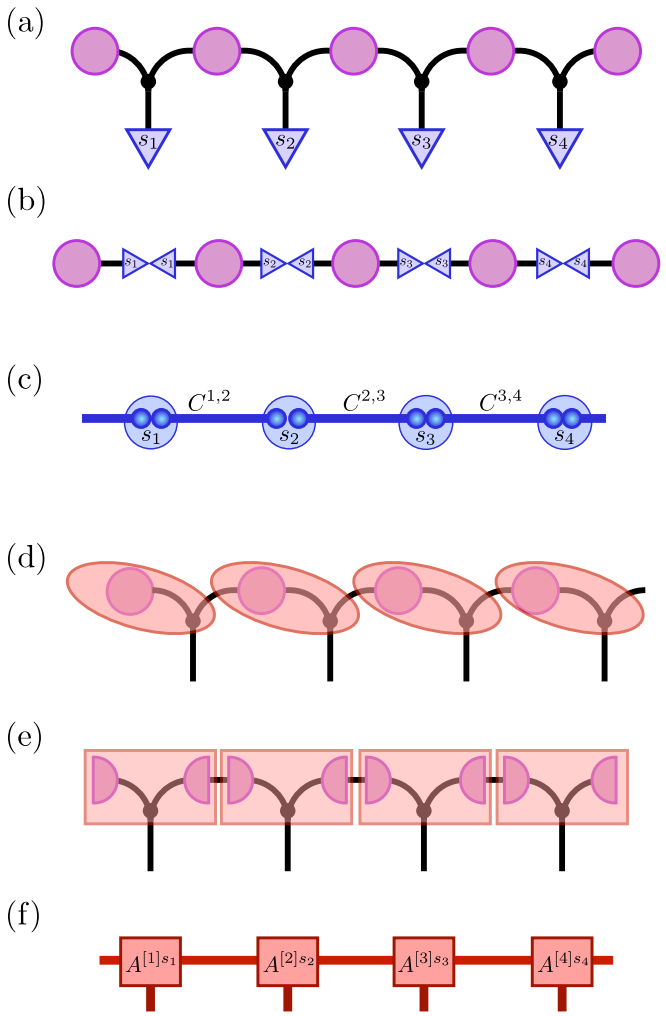

Figure 5.3: Illustration of the equivalence between matrix product states and correlator product states for the simple case of bond correlators, when the dimension of the correlators is the same as the physical dimension: (a) Shows the correlators connected by copy tensors (black dots); (b) this can be factorised, breaking up the connections while ensuring the same configuration is present on neighbouring correlators; (c) this gives a product of scalar correlator elements. This network can be considered to be equivalent to a MPS (f) where the matrices are formed of: (d) a single correlator and the copy tensor; or (e) two neighbouring 'split' correlators and the copy tensor.

As shown in Figure 5.3(b) this acts to break up the bonds between the matrices while ensuring that neighbouring matrices are contracted according to the same physical index on a pair of virtual legs. The result of this is a product of scalars, shown in Figure 5.3(c), which are the correlators for a given configuration.

We can see this equivalence to a matrix product state simply by expressing the $\mathbf{A}$ matrices as shown in Figures 5.3(d) and 5.3(f) i.e. each matrix is a product of the correlator matrix and the copy tensor. This is not the only way that the $\mathbf{A}$ matrices can be formed: alternatively each correlator matrix can be split into a product of two matrices e.g. by taking the square root of the matrix or performing a singular value decomposition [134] as shown in Figures 5.3(e) and 5.3(f). In all cases the boundary vectors are simply formed by terminating the network with uniform vectors (and multiply the uniform vectors with the 'split' correlator matrices if appropriate).

This can be illustrated with the simple case of a GHZ state. The antiferromagnetic GHZ state is given by $|\psi\rangle = |\uparrow\downarrow\uparrow\downarrow\cdots\uparrow\downarrow\rangle + |\downarrow\uparrow\downarrow\uparrow\cdots\downarrow\uparrow\rangle$. This has an exact correlator product state representation, where all the correlators are identical and where

$$\mathbf{C} = \begin{pmatrix} 0 & 1 \\ 1 & 0 \end{pmatrix}.$$

We can see from this correlator matrix that any configuration with neighbouring sites having the same configuration (i.e. diagonal elements) will be zero. All configurations with all neighbouring sites having different configurations (i.e. off-diagonal elements) will have the same amplitude. We can express the copy tensor as

$$\mathbf{P} = \begin{pmatrix} |\uparrow\rangle & 0 \\ 0 & |\downarrow\rangle \end{pmatrix},$$

by absorbing the physical leg inside of the matrix making its elements vectors. Forming the $\mathbf{A}$ matrices as given in Figures 5.3(d) and 5.3(e) by simply multiplying the copy tensor and the correlator tensor together gives $\mathbf{A}^{\downarrow} = \sigma^{+}$ and $\mathbf{A}^{\uparrow} = \sigma^{-}$. We can see this is a correct MPS representation since $(\mathbf{A}^{\uparrow})^2 = (\mathbf{A}^{\downarrow})^2 = 0$, and the only two non-zero amplitudes are with all neighbouring spins opposite i.e. an antiferromagnetic state.

In two dimensions, correlator product states can also be considered to be equivalent to a special case of PEPS — in this case the copy tensor copies the physical index to four different correlator matrices. String bond states [148] are another special factorisation of PEPS where the contractible components are themselves MPS, rather than a correlator matrix. States such as these can then be sampled efficiently, as they consist of product of scalar values,

each scalar value only depending on a small number of physical indices.

Note that although every nearest-neighbour bond one-dimensional CPS has a MPS dimension of $\chi = d$, the reverse is not always true. For example, consider the W-state, $|\psi\rangle = |\downarrow\uparrow\uparrow\cdots\uparrow\rangle + |\uparrow\downarrow\uparrow\cdots\uparrow\rangle + \cdots + |\uparrow\uparrow\uparrow\cdots\downarrow\rangle$. This has an exact MPS representation with $\chi = 2$ [151], but does not have an exact CPS representation (unless the projector $\hat{P}_N$ is used to project to states with total spin $N-2$). These are MPS that cannot be factorised using the copy tensor.

Since the MPS representation is exhaustive, every correlator product state will have an equivalent matrix product state. However, for certain systems, it may be far more efficient to use the CPS representation. For example, in the MPS representation long-range correlations are mediated by the bonds between neighbouring sites. Thus, in general, a very large bond-dimension χ will be needed between neighbouring sites to capture the entanglement between sites spaced by a large distance (although there are specific cases where long range correlations are efficiently mediated using MPS). However, using CPS it is possible to include a correlator directly between distant sites, describing the entanglement with a small bond dimension since the bond directly links the two sites (we see an example of this in relation to the Laughlin wave function, described in detail in Chapter 7). Correlator product states can thus describe systems that do not obey an area law.

5.3 Determining the ground-state wave function

Given that the weight for each configuration is given by a product of scalars, the ground-state wave function can be found easily using variational methods. In [134] a generalised eigenvalue method was used, where a reduced Hamiltonian and overlap matrix are constructed via Monte Carlo sampling. A deterministic method has also been shown in [150]. We have used a stochastic minimisation method [152] to determine the ground-state that has previously been applied to one-dimensional systems represented by matrix product states [153].

5.3.1 Calculating expectation values

We determine expectation values of the energy and other operators using Monte Carlo importance sampling, which gives a polynomial scaling of the computation time required with the system size for a given statistical error

(typically N^3). The energy E is given by

$$E = \langle\psi|H|\psi\rangle = \frac{\sum_{\mathbf{s},\mathbf{s}'} W^*(\mathbf{s}')\langle\mathbf{s}'|H|\mathbf{s}\rangle W(\mathbf{s})}{\sum_{\mathbf{s}} |W(\mathbf{s})|^2}, \tag{5.6}$$

where we have assumed that the wave function is not normalised, which will generally be the case when using correlator product states. The energy can be expressed as a weighted sum

$$E = \frac{\sum_{\mathbf{s}} |W(\mathbf{s})|^2 \sum_{\mathbf{s}'} \frac{W^*(\mathbf{s}')}{W^*(\mathbf{s})}\langle\mathbf{s}'|H|\mathbf{s}\rangle}{\sum_{\mathbf{s}} |W(\mathbf{s})|^2} = \sum_{\mathbf{s}} P(\mathbf{s})E(\mathbf{s}) \tag{5.7}$$

which we can express as a sum over configurations of the product of the local energy $E(\mathbf{s})$ and the probability $P(\mathbf{s})$, given by

$$P(\mathbf{s}) = \frac{|W(\mathbf{s})|^2}{\sum_{\mathbf{s}} |W(\mathbf{s})|^2}, E(\mathbf{s}) = \sum_{\mathbf{s}'} \frac{W^*(\mathbf{s}')}{W^*(\mathbf{s})}\langle\mathbf{s}'|H|\mathbf{s}\rangle. \tag{5.8}$$

The Hamiltonian can be replaced with any other operator to calculate other expectation values. The probability of a given configuration is never explicitly calculated using Equation (5.8). Instead, the configurations are visited according to importance sampling, i.e. the number of times a configuration is visited is proportional to the probability of that configuration, with the local energy contribution added to the total energy each time that configuration is visited. To achieve this we use the Metropolis Algorithm [154]:

Pick initial configuration We start by picking an initial configuration $\mathbf{s}$. When picking an initial configuration it is important to pick one that is not too far in configuration space from the most likely configurations. In the case of a spin-$\frac{1}{2}$ system (see Chapter 6), for the first sample we start with all spins polarised. After the first sample, in which the absolute magnetisation is calculated, we start with an initial configuration having the same magnetisation as previously calculated. In the case of the Bose-Hubbard model on a disk, we start with all atoms within 90% of the disk radius.

Propose a move We then propose a move $\mathbf{s} \to \mathbf{s}'$ to a new configuration. In a spin-$\frac{1}{2}$ system this is done by flipping a spin, where each spin is visited sequentially. For the Bose-Hubbard model, this is done by moving a particle to a new, random, site, where each particle is moved in sequence.

Determine acceptance probability The acceptance probability P_{acc} describes how likely the proposed configuration is in comparison to current configuration and thus gives the probability of accepting the new move. It is calculated from the ratio of the weights for the proposed and current configurations using $\min\left[\frac{|W(\mathbf{s}')|^2}{|W(\mathbf{s})|^2}, 1\right]$. If $P_{\text{acc}} > \mathtt{r}$, where $\mathtt{r}$ is a random number between 0 and 1, the move is accepted, and the proposed configuration becomes the current configuration, otherwise the move is rejected and the current configuration remains unchanged and is used again.

Determine local variables The local energy $E(\mathbf{s})$, is then calculated for the current configuration, as well as the local values of any other operators.

A new move is then proposed, the acceptance probability recalculated and the total energy summed according to this method. This is repeated $F \times N$, times, where we call F the number of sweeps per sample, and N is the number of particles in the system (since we visit each particle or site sequentially in a given sweep). Before the $F \times N$ sweeps that contribute to the estimation of the energy and other values there are a few warm-up sweeps that do not contribute to the estimates, to ensure that the random walk through configuration space starts in an equilibrium position. Also the local expectation value is not calculated and added to the total value every sweep, but instead is added every $\mathtt{s}^{th}$ sweep, where $\mathtt{s}$ is the sample rate ~ 10, to allow a larger portion of the configuration space to be sampled, and to ensure that the configurations that are sampled are independent from one another.

At no point during the calculation is knowledge of the normalisation of the wave function needed. The most time-consuming step in the calculation is that of determining the correlator fraction $W(\mathbf{s}')/W(\mathbf{s})$. Since the configuration weight is given by a simple product of numbers, to calculate this fraction only the correlators that represent the sites where the configurations have changed are required. Calculation of the correlator fraction scales with $N_s N_c$, where N_s is the number of sites covered by a correlator and N_c is the number of correlators that cover a given site. If the Hamiltonian is local then there are only a few configurations $\mathbf{s}'$ that have a non-zero matrix element in the local energy, so only a few correlator fraction terms need to be calculated for each contribution to the energy.

5.3.2 Minimising the energy

We minimise the energy using a stochastic minimisation method which requires only the sign of the first derivative of the energy with respect to the correlator elements [152].

The first derivative is given by

$$\frac{\partial E}{\partial C^{\{i\}}_{s_{\{i\}}}} = 2(\langle \Delta^{\{i\}}_{s_{\{i\}}} E\rangle - \langle \Delta^{\{i\}}_{s_{\{i\}}}\rangle\langle E\rangle), \tag{5.9}$$

where $\Delta^{\{i\}}_{s_{\{i\}}}(\mathbf{s})$ is given by

$$\Delta^{\{i\}}_{s_{\{i\}}}(\mathbf{s}) = \frac{1}{W(\mathbf{s})}\frac{\partial W(\mathbf{s})}{\partial C^{\{i\}}_{s_{\{i\}}}} \tag{5.10}$$

This is trivial to compute, since $W(\mathbf{s})$ is simply a product of the different correlators C. If each correlator is only used once it is given by $1/C^{\{i\}}$, whereas if the same correlator is used for multiple sites (e.g. in a translationally invariant system) it is given by $b^{\{i\}}/C^{\{i\}}$, where $b^{\{i\}}$ is the number of times the correlator $C^{\{i\}}$ appears in the product for the correlator amplitude for configuration $\mathbf{s}$.

We calculate the expectation value of the derivative in the same way that other operators are calculated for F sweeps in a sample, and the derivatives for all correlators are calculated simultaneously. After this every correlator is updated according to

$$C^{\{i\}}_{s_{\{i\}}} \rightarrow C^{\{i\}}_{s_{\{i\}}} - \mathtt{r}\delta(k)\mathrm{sign}\left(\frac{\partial E}{\partial C^{\{i\}}_{s_{\{i\}}}}\right), \tag{5.11}$$

where $\mathtt{r}$ is a random number between 0 and 1, and $\delta(k)$ is the step-size for a given iteration k. Unlike the Newton method, the second derivative is not required, considerably simplifying the calculation. As reported in [152] this method is found to give better convergence than the Newton method, since it is faster to compute and also because it avoids statistical errors in the second derivative, which can be very large. In addition, this method does not exactly follow the true gradient which is preferable since it is not always efficient to move in exactly the same direction as the steepest descent.

To achieve convergence, the number of samples is increased every iteration, and the step size $\delta(k)$ is reduced. For every iteration k, F is given by $F_0 k$, and the procedure is repeated $G = G_0 k$ times per iteration, where typically F_0 and $G_0 \sim$ 10. The step size is reduced per iteration as $\delta = \delta_0 k^{-\eta}$.

We have found best results with η between 0.75 and 0.9.

After an initial run with a relatively large step size to get close to the result, the resulting correlators are then used as a starting point for a new run of iterations (i.e. k is reset) where F_0 and G_0 are unchanged, but δ_0 is decreased. Depending on the system parameters this can reduce the energy further (while for other parameters the energy has already converged after the first run).

After minimisation is complete, the procedure is repeated for a single iteration with zero step size and large F and G, to obtain an accurate estimate of the expectation values.

Chapter 6

Two-dimensional quantum Ising model

We now consider spin models in lattice systems. As described in 1.3.2, spin models can be realised by using spin dependent lattices to engineer the spin exchange interaction, or by mapping the hardcore Bose-Hubbard Hamiltonian to a spin model.

6.1 Background

We choose to apply the correlator product state (CPS) method to the 2D quantum Ising model, which is described by the Hamiltonian

$$H = -\sum_{i=1,j=1}^{L} (\sigma_z^{[i,j]}\sigma_z^{[i+1,j]} + \sigma_z^{[i,j]}\sigma_z^{[i,j+1]} + B\sigma_x^{[i,j]}), \tag{6.1}$$

where i and j denote the lattice index in the two perpendicular directions, and B is the transverse magnetic field. This model has not so far been realised in ultracold atom systems.[1] However, the reason we choose to study this model is because it is one of the simplest systems that exhibits a quantum phase transition at a finite magnetic field. The system moves from an ordered ferromagnet in the z direction at $B = 0$ to a state disordered in the z direction at $B > B_c$. By applying the correlator product states to this system, we can

[1]The model has an experimental realisation in three dimensions in $LiHoF_4$ crystals [155]. The holmium atoms have an easy axis at low temperatures, which will align either parallel or anti-parallel to this axis.

investigate the performance of the description, and compare with the many previous studies performed using other numerical and analytical methods. This system is thus used to benchmark the method and demonstrate its usefulness before moving to the Bose-Hubbard model in Chapter 7.

The position of the critical point has been calculated using a finite-size scaling analysis, and was found to be at $B_c \approx 3.044$ [156, 157, 158]. Approximate numerical methods that have been used to determine the properties of the ground state for larger systems include an adjusted density-matrix renormalisation method to handle two-dimensional systems of limited width [159]. This particular method was able to reach system sizes of 30×6 spins. The system has also been investigated using string bond states [148] for a 10×10 system[2] and tree tensor networks (TTNs) [160], which are another type of tensor network state, for up to a 32×32 system.

6.2 System set-up

6.2.1 Correlator types

We study the ground states of the quantum Ising model using different types of correlator, and compare their properties. We use periodic boundary conditions - the translational invariance of the system allows us to use one correlator of each type to describe the system.

The types of correlators used are illustrated in Figure 6.1. For all correlator types we restrict to only real parameters without any loss of generality. The simplest we use are nearest-neighbour bond correlators, with one correlator for the vertical bonds and one correlator for the horizontal bonds as shown in Figure 6.1(a). This gives a description of the ground state using only eight parameters. We also use bond correlators with longer range bonds. Figure 6.1(b) shows the set-up with the maximum bond length $\Delta\mathbf{r}_{\max} = (1, 1)$, and in the following calculations we use correlators up to $\Delta\mathbf{r}_{\max} = (10, 10)$. The correlators for $\Delta\mathbf{r}_{\max} = (r_{\max}, r_{\max})$ include all bonds with the vector between two sites up to the maximum distance i.e. it includes all the diagonal bonds as well as bonds along the lattice axes. This is demonstrated in Figure 6.2 which shows all the correlator bonds that originate from a single lattice site for $r_{\max} = 2$ — these correlators will be repeated across the entire lattice. For correlators up to $r_{\max}$, the number of correlator elements is $8r_{\max}(r_{\max} + 1)$. As described in section 5.3.1, the computational effort scales with the num-

[2]The authors state that the code used is a simple non-optimised MATLAB code for the purposes of demonstrating the technique only. Accordingly, it is likely that larger systems could be treated in this way.

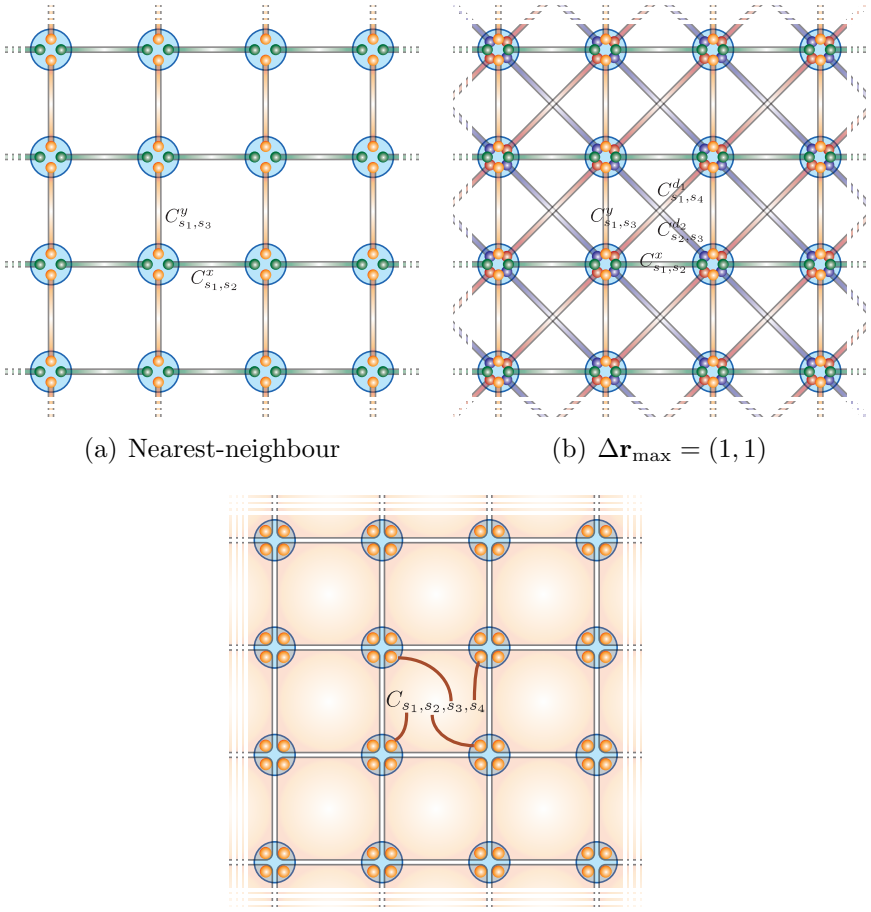

(a) Nearest-neighbour (b) $\Delta\mathbf{r}_{\max} = (1, 1)$

(c) 2×2 plaquette

Figure 6.1: Illustration of the different correlator types used to simulate the 2D Ising model.

ber of sites covered by the correlator multiplied by the number of correlators associated with a given site. This gives a scaling of $\mathcal{C} \propto 4r_{\max}(r_{\max} + 1)$.

We also use plaquette correlators, with the smallest 2×2 plaquette illustrated in Figure 6.1(c). Plaquette correlators up to a size of 4×4 plaquettes, i.e. a plaquette that covers 16 sites, were used. The correlators are set up so they are displaced from one another by one site, i.e. so that the correlators overlap one another. The number of elements in an $n \times n$ correlator scales as 2^{n^2}, so the memory requirements for a given plaquette correlator size scale much faster than for bond correlators. However the computation effort scales as $\mathcal{C} \propto n^4$, which grows much more slowly than the number of elements in the system. This means we would expect a calculation using 3×3 plaque-

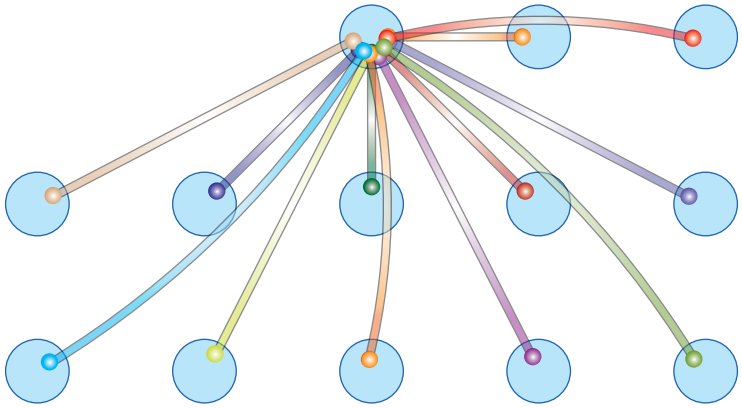

Figure 6.2: Bond correlators for $\Delta\mathbf{r}_{\max} = (2,2)$ originating from a single site. These correlators are repeated across the entire lattice.

tte correlators to be as computationally intensive as a calculation using bond correlators up to $r_{\max} = 4$, and a calculation using 4×4 plaquette correlators to be as computationally intensive as a calculation using bond correlators up to $r_{\max} = 8$. However, although the computational effort is similar, the way the minimisation algorithm behaves is not necessarily the same for different correlator types, which we will see in section 6.3.

6.2.2 Calculation of energy and derivative

The energy and derivative, as well as other observables, are calculated using the algorithm described in section 5.3.1. Calculation of the interaction energy terms $\sigma_z^{[i,j]}\sigma_z^{[i+1,j]}$ is straightforward since the operators are diagonal: the local energy $E_{zz}(\mathbf{s})$ is given by

$$E_{zz}(\mathbf{s}) = -\sum_{i=1,j=1}^{L} (s^{[i,j]}s^{[i+1,j]} + s^{[i,j]}s^{[i,j+1]}), \tag{6.2}$$

where $s^{[i,j]} = \pm1$. In a translationally invariant system, we can dispense with the sum over all sites and simply take the exchange energy of the first and second (or any other pair) of spins.

To calculate the transverse energy terms $B\sigma_x^{[i]}$, we use $\sigma_x = \sigma_+ + \sigma_-$. The only non-zero terms of the energy estimator $E(\mathbf{s}) = \sum_{\mathbf{s}'} \frac{W(\mathbf{s}')}{W(\mathbf{s})}\langle\mathbf{s}'|H|\mathbf{s}\rangle$, are those for which $\mathbf{s}'$ differs from $\mathbf{s}$ by a single spin-flip, so the local transverse

Correlator type	No. of elements	Energy	Error
Nearest-neighbour bonds	8	$-3.2348(4)$	13×10^{-3}
Bonds with $\Delta\mathbf{r}_{\max} = (1,1)$	16	$-3.2384(3)$	9×10^{-3}
Bonds with $\Delta\mathbf{r}_{\max} = (2,2)$	48	$-3.2457(3)$	2×10^{-3}
Bonds with $\Delta\mathbf{r}_{\max} = (3,3)$	96	$-3.2465(2)$	1×10^{-3}
2×2 plaquettes	16	$-3.2387(4)$	9×10^{-3}
3×3 plaquettes	512	$-3.2463(2)$	1×10^{-3}
4×4 plaquettes	65,536	$-3.24725(5)$	2×10^{-5}

Table 6.1: Energy per site found using stochastic minimisation for the 2D Ising model in a 6×6 system for different correlator types. Results are compared with exact results found in [156] at $B = 3.05266$

energy is given by

$$E_x(\mathbf{s}) = -\sum_{i=1,j=1}^{L} \frac{W(\mathbf{s}'_{ij})}{W(\mathbf{s})}. \tag{6.3}$$

We also calculate the absolute magnetisation $\langle|\sigma_z|\rangle$ of the ground state. Note that the expectation value of the magnetisation $\langle\sigma_z\rangle$ will always be zero, since the symmetry of the system means the ground state will form equal superpositions of configurations with all spins flipped. However, we can calculate the absolute magnetisation which quantifies how well the spins are aligned with one another, by summing the local absolute magnetisation

$$|\sigma_z(\mathbf{s})| = \frac{1}{L^2}\left|\sum_{i=1,j=1}^{L} s^{[i,j]}\right|. \tag{6.4}$$

The derivative is calculated using equation (5.9), where $\Delta^{\{i\}}_{s_{\{i\}}}(\mathbf{s}) = b^{\{i\}}/C^{\{i\}}$, where $b^{\{i\}}$ is the number of time the correlator $C^{\{i\}}$ appears in the product for the correlator amplitude for configuration $\mathbf{s}$.

For bond correlators and for 2×2 plaquette correlators, we start with a uniform state, and perform initial minimisation with $F_0 = 10$, $G_0 = 10$, $\delta_0 = 0.02$, $\eta = 0.9$ for 25 iterations. For 3×3 and 4×4 plaquette correlators, we build the initial correlator using the 2×2 plaquette correlator that results from the first round of minimisation. For all correlator types, we then reset the iteration counter, and perform the minimisation procedure again using the minimised correlator as a starting point, and $\delta_0 = 0.005$ for 30 iterations. We then obtain accurate estimations of the expectation values by performing a final calculation with one iteration having $F = 10,000$, $G = 100$, $\delta = 0$.

Correlator type	No. of elements	Energy
Nearest-neighbour bonds	8	−3.2325(1)
Bonds with $\Delta\mathbf{r}_{\max} = (1,1)$	16	−3.2356(1)
Bonds with $\Delta\mathbf{r}_{\max} = (5,5)$	240	−3.23850(6)
Bonds with $\Delta\mathbf{r}_{\max} = (10,10)$	880	−3.2358(1)
2×2 plaquettes	16	−3.23599(9)
3×3 plaquettes	512	−3.23864(4)
4×4 plaquettes	65,536	−3.23895(4)

Table 6.2: Energy per site found using stochastic minimisation for the 2D Ising model in a 31×31 system for different correlator types at $B = 3.05$

6.3 Results

6.3.1 Energies

We first calculate the energy for a 6×6 system. This is the largest system that has been solved exactly [156], so provides a good comparison for how well the method is working. This system size has also been solved using TTNs [160], so we also compare the accuracy of the CPS method those results.

The ground state is found at $B = 3.05266$, which is calculated to be the pseudo-critical point in a 6×6 system, with a ground state energy of -3.2472744... The energy of the ground state found using different correlator types is shown in Table 6.1. The error, that is the difference between the energy estimated using CPS and the ground state energy found exactly, is also displayed. As expected, the energy converges to the exact value the larger the correlator size. The agreement for a given plaquette size can be compared with that found using TTNs [160]. In that work to reduce the error to around 2×10^{-5} required $\chi = 200$, therefore the number of parameters is comparable to 4×4 plaquette correlators which achieve a similar accuracy.

We next apply the CPS method to much larger systems. Table 6.2 shows the minimised energy in a 31×31 system at $B = 3.05$, which should be close to the pseudo-critical point. This is the largest system in which we can calculate the ground state energy in a reasonable time for 4×4 plaquette correlators, although larger system sizes can be reached for smaller correlators.

The minimised energy converges for plaquette correlators, however for bond correlators we encounter difficulties in minimising the energy within $25 + 30$ iterations. Even though the number of elements is much larger for 4×4 plaquette correlators, the energy converges much more readily. It could be that having a larger number of parameters actually allows the system more

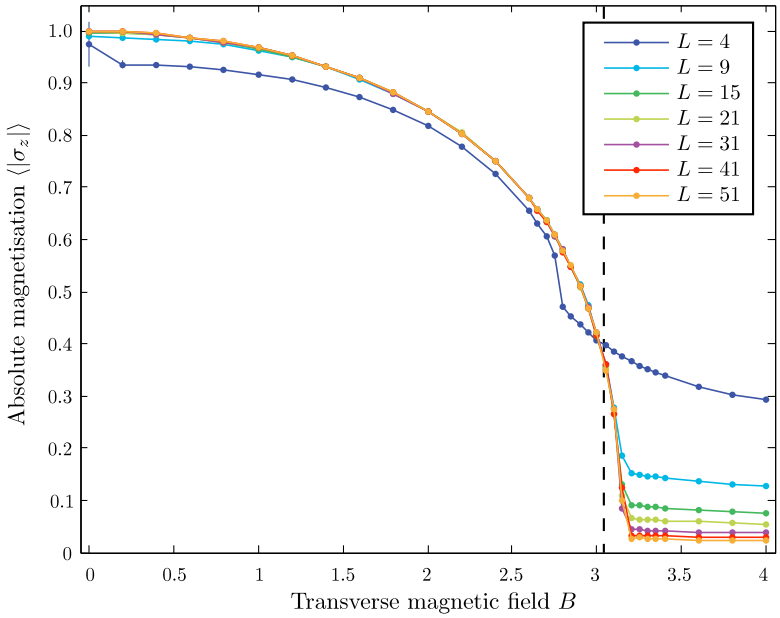

Figure 6.3: Magnetisation as a function of transverse magnetic field for an $L \times L$ system, for the ground state found using 2×2 plaquette correlators. The dotted line indicates the critical magnetic field found by a finite-scaling analysis in [156].

freedom in finding the minimum energy state, while constraining the number of parameters for such long range bonds tends to result in a more difficult minimisation problem. It is well known from optimisation theory that having more parameters than is strictly needed can often aid the algorithm.

Using the TTN method, the authors of [160] state that they no longer obtain convincingly converged results for $L \geq 10$ with $\chi \approx 500$ close to the critical point. The authors examine the magnetisation for different values of χ to determine how well the results are converging. In the next section we examine the behaviour of various parameters as the transverse magnetic field is varied.

6.3.2 Transition point

As described above, there is a quantum phase transition as the magnetic field is increased, from a state with ferromagnetic order in the z direction when $B < B_c$ to a state with disordered z components at $B > B_c$. The critical point in the thermodynamic limit, found using a finite-scaling analysis in [156], is $B_c = 3.044$, where the pseudo-critical point was defined using the

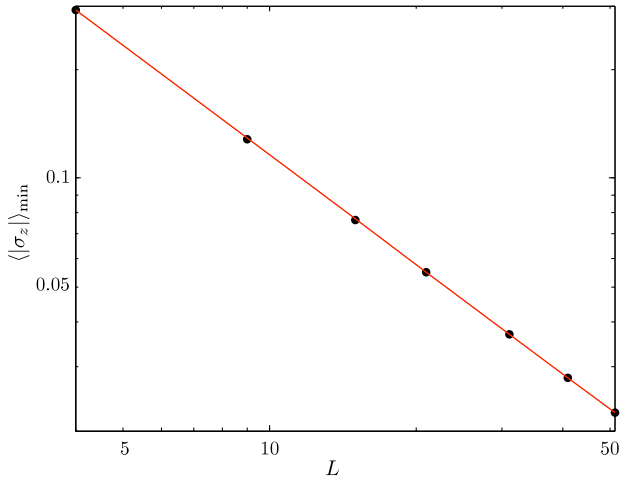

Figure 6.4: Absolute magnetisation at $B = 4$ for an $L \times L$ lattice. The black dots show the calculated absolute magnetisation and the red line shows a fit of the form $\langle|\sigma_z|\rangle_{\min} = aL^{-b}$. The fitted parameters are $a = 1.181(5)$, $b = 1.001(2)$.

ratio of the energy gap between consecutive system sizes.

The absolute magnetisation as a function of transverse magnetic field is calculated using 2×2 plaquette correlators for a number of $L \times L$ system sizes, shown in Figure 6.3. The error bars for each point, where the error is given as the standard deviation of the G different samples, are plotted, but for most cases are smaller than the marker for the data point. For the largest system size ($L = 51$), the calculation took around two weeks.

We find a sharp drop in the magnetisation at around $B = 3.05$ as we would expect, where the change in magnetisation becomes steeper as the system size increases. We also find that magnetisation for $B > B_c$ is flatter and decreases as the system size increases: for $L = 51$, the minimum magnetisation is 0.022. Figure 6.4 shows the minimum magnetisation (which occurs at $B = 4$) as a function of lattice size, with a fit to polynomial decay of the minimisation i.e. $\langle|\sigma_z|\rangle_{min} = aL^{-b}$. The data fits an inverse scaling with system size, indicating that the magnetisation decays to zero in an infinite system.

As we saw with respect to the minimum energy, the larger the correlator used the better the approximation to the ground state. For this reason we also investigate how the absolute magnetisation as a function of magnetic field changes as the plaquette size is increased, and for different plaquette types. This is shown in Figure 6.5.

The plot in Figure 6.5 also indicates the position of the critical point found by a finite-scaling analysis in [156]. We see that as the correlator

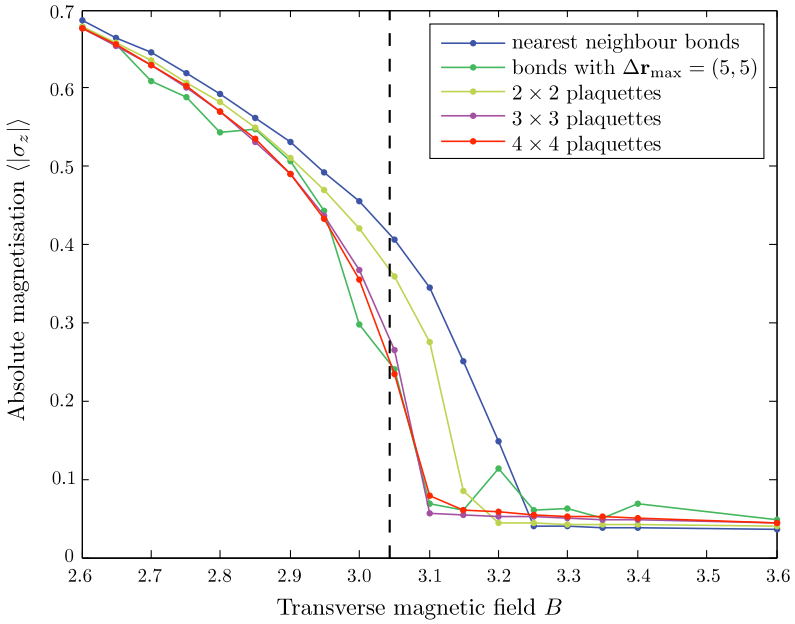

Figure 6.5: Absolute magnetisation as a function of transverse magnetic field for a 31×31 system, for the ground state found using different sized correlators. The dotted line indicates the critical magnetic field found by a finite-scaling analysis in [156].

size increases, the change in the magnetisation moves closer to the critical point. The results begin to converge for large plaquette correlators although there are still some differences. We also see that the minimum magnetisation increases, indicating that the decay of the minimisation is slower than that shown in Figure 6.4.

Of note is the behaviour of the magnetisation for bond correlators with $r_{\max} = 5$, which shows noisy behaviour. As described above, we encountered difficulties minimising these correlators, which tended to get 'stuck' at certain values. Restarting the minimisation procedure (i.e. resetting the step size δ, and the number of sweeps F and samples G) improves the convergence, and if this procedure were to be repeated it seems likely that the magnetisation for bond correlators with $r_{\max} = 5$ would also tend to the values found for large plaquette correlators. However, such a calculation would be much more time consuming for a similar degree of convergence to the exact value since more iterations would be required.

We also investigate the transverse magnetisation as a function of magnetic field, which is shown in Figure 6.6. As expected, the transverse magnetisation

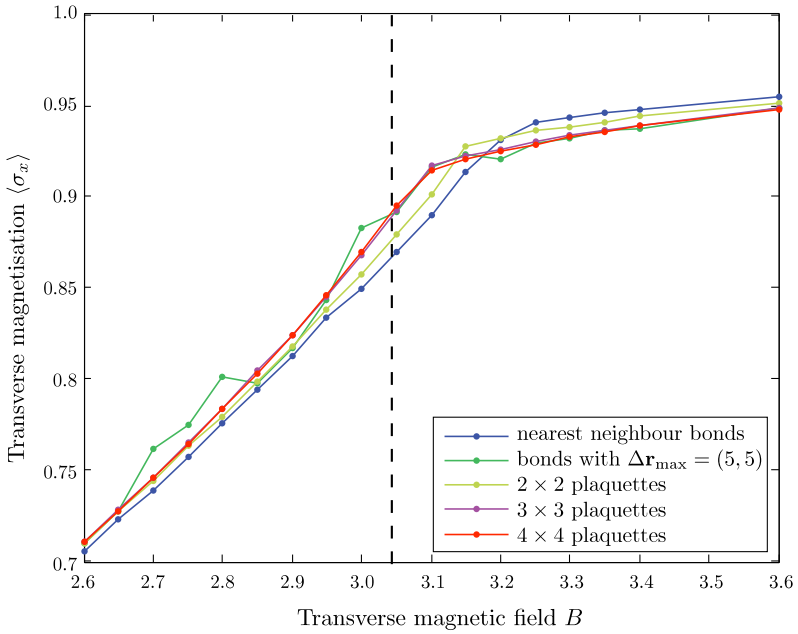

Figure 6.6: Transverse magnetisation as a function of transverse magnetic field for a 31×31 system, for the ground state found using different sized correlators. The dotted line indicates the critical magnetic field found by a finite-scaling analysis in [156].

increases as a function of transverse magnetic field, and levels off at a value close to 1 at the critical point. We see this value decrease as the correlator size increases, and as with the absolute magnetisation, we see the change in gradient move close to the estimated critical point as the correlator size increases. We see similar noisy behaviour in the transverse magnetisation calculated using bond correlators with $r_{\max} = 5$. The magnetisation close to $B = B_c$ does not completely converge for the larger correlators: the difference in $\langle \sigma_x \rangle$ for the 4×4 plaquette correlator and the 3×3 plaquette correlator is 0.003. This is comparable with the convergence found using TTNs in [160], where for a 10×10 system, the difference in the transverse magnetisation for $\chi = 100$ and $\chi = 200$ is ~ 0.002.

6.3.3 Long-range correlations

As discussed in section 5.1.2 the success of the tensor network approach is intimately connected with the decay of correlations in the system. When the correlations are short range, the tensor network representation is likely to be able to model the system well, with a number of parameters much smaller than the Hilbert space size. However, when the correlations decay algebraically, it can be difficult to model the system well using these methods, and a larger number of parameters are required to describe the entanglement in the system.

We calculate the two point correlation function given by

$$C_{x,y} = \langle \sigma_z^{[0,0]} \sigma_z^{[x,y]} \rangle - \langle |\sigma_z^{[0,0]}| \rangle \langle |\sigma_z^{[x,y]}| \rangle, \tag{6.5}$$

after the wave function has been minimised, at different values of the transverse magnetic field and for different correlator types. The two point correlation function $C_{x,y}$ describes the probability of two spins on separated sites being aligned with one another, where the uncorrelated average is subtracted. It can only be non-zero if entanglement exists between these two sites.

When the system is close to the pseudo-critical point, we would expect the correlation function to decay algebraically, and thus expect the system to be the hardest to simulate numerically. Figure 6.7 shows calculations of the correlation function at $B = 3.05$ in a 31×31 system. Figures 6.7(a) and 6.7(b) show a plot of $C_{x,y}$ for different correlator types. It is clear that using nearest-neighbour bonds to describe the system discards much of the information about long-range correlations in the system, which are revealed when a larger correlator (4×4 plaquette) is used. In Figures 6.7(c) and 6.7(d) we plot the average of the two-point correlation function for a given distance l for a lattice point given by

$$C_l = \frac{1}{4}(C_{l,0} + C_{-l,0} + C_{0,l} + C_{0,-l}). \tag{6.6}$$

The error bars denote the standard deviation of this average. Figure 6.7(c) shows a linear plot for different correlator types, demonstrating that a slower decay of the correlation function is revealed as the correlator size is increased. However even for the larger correlators the correlation function is not yet converged.

Figure 6.7(d) shows a log-log plot of the same data. None of the correlators indicate an algebraic decay of the correlation function, although bond correlators with $r_{\max} = 5$ shows the slowest decay, and the behaviour does appear to be tending to an algebraic decay.

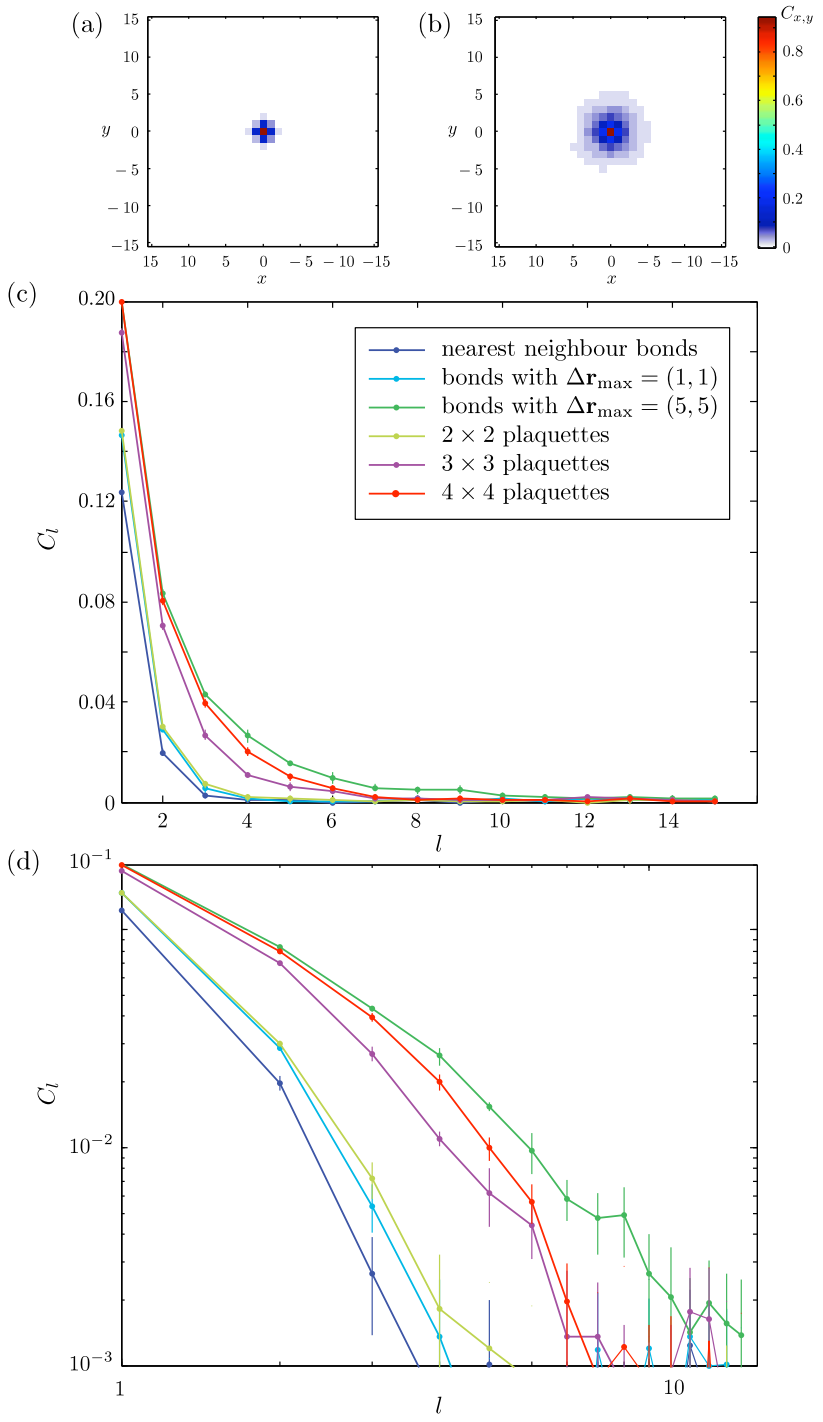

Figure 6.7: Two point correlation function $C_{x,y}$ at $B = 3.05$ for (a) nearest-neighbour bond correlators, and (b) 4×4 plaquette correlators. (c) C_l for different correlator types and (d) the same data on a log-log scale.

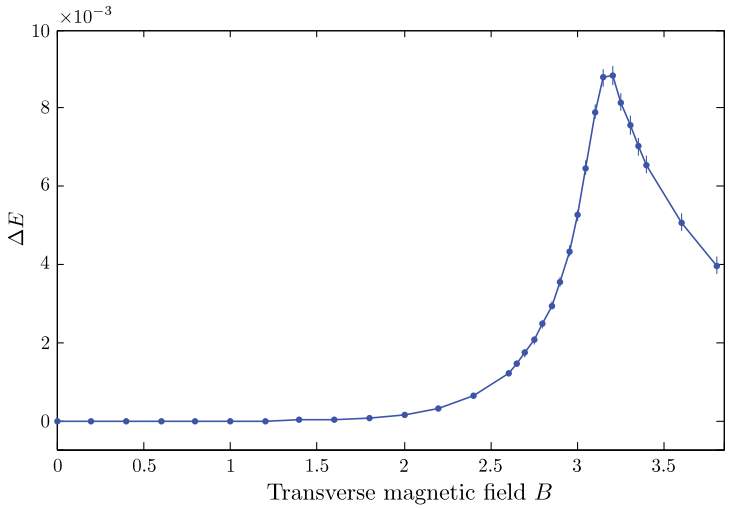

Figure 6.8: Difference in energy between ground state calculated using nearest-neighbour bond correlators, and ground state calculated using 4×4 plaquette correlators.

It is perhaps surprising that the bond correlators show the slowest decay of correlator length when they do not produce the lowest ground state energy. The reason for this could be that the structure of bond correlators allows an efficient description of long-range correlations since it provides direct bonds between distant lattice sites. However the relatively small number of parameters (in comparison to the plaquette correlators) limits the accuracy to which it can describe global properties of the system, such as the energy and magnetisation. Of course it is possible that the difficulty in minimising these correlators also plays a part. It would be interesting to investigate this matter further, although it would require a large increase in calculation time.

We also investigate how the behaviour of the correlation function affects the calculation of the energy. Figure 6.8 shows the difference between the energy calculated using nearest-neighbour bond correlators (which give the highest ground state energy) and the energy calculated using 4×4 plaquette correlators (which give the lowest ground state energy), for different values of the transverse magnetic field B. We find that there is not much difference between the two values away from $B = B_c$, but the energy difference increases when $B \approx B_c$.

We can understand this behaviour by considering the decay of the correlation function for different values of the transverse magnetic field. This is illustrated in Figure 6.9, which shows the average correlation function C_l

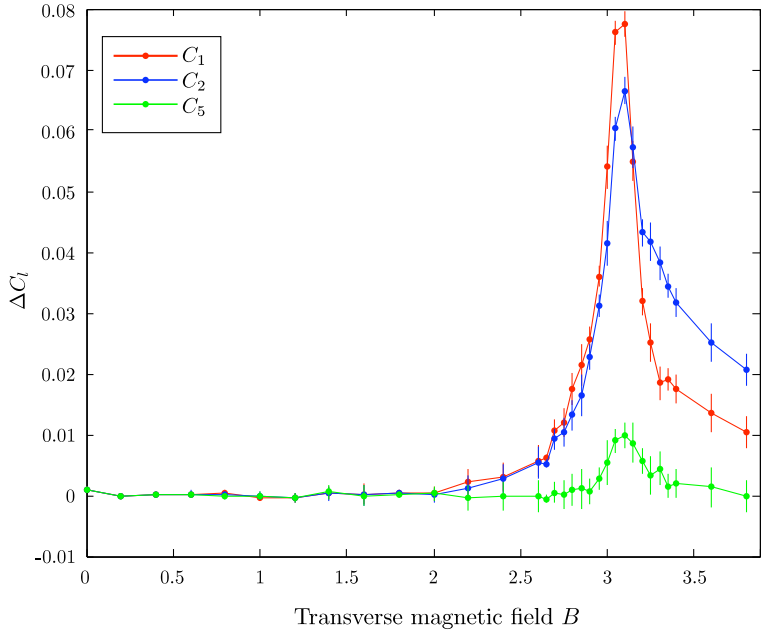

Figure 6.9: Difference in two point correlation function between ground state calculated using nearest-neighbour bond correlators, and ground state calculated using 4×4 plaquette correlators

for different separations l, calculated using 4×4 plaquette correlators. We see the same form as shown in Figure 6.8. This is exactly the behaviour that would be expected: when the correlations are short range the energy can be calculated accurately using a small number of parameters, however as the correlation length increases larger correlators are needed to describe the system accurately.

6.4 Summary

We have investigated the performance of various forms of correlator product states for describing the ground state of the 2D quantum Ising model. Even correlators with a small number of parameters (16 parameters for the 2×2 plaquette correlator) can describe the qualitative behaviour of large systems (up to 51×51 spins). Increasing the correlator size to 4×4 site plaquettes provides accurate results for small systems although for large systems does

not lead to complete convergence. We have found that large correlators can describe long range correlations in a 31×31 system, and that bond correlators are more successful than plaquette correlators at describing long range correlators. However we have encountered difficulties in reliably determining the ground state expectation values using bond correlators. In addition, the ground state energy obtained is larger than that found using plaquette correlators. The findings in this section provide insights for further studies and the usage of correlator product states for optical lattice systems.

Chapter 7

The fractional quantum Hall effect in optical lattices

We will now apply the correlator product state (CPS) method to the Bose-Hubbard model in an artificial magnetic field, with the aim of studying the FQH effect in optical lattices, which was introduced in section 4.3. The FQH regime has yet to be reached in an optical lattice,[1] and simulations of realistic-sized systems are useful for determining the parameters that would be required and the expected behaviour of these strongly correlated states. Our calculations concentrate on the low α regime, where the Laughlin wave function given in equation (4.6) is a good description of the ground state.

7.1 Background

Exact calculations have previously been used to numerically determine the properties of the Bose-Hubbard model in an artificial magnetic field [93, 119, 97, 121]. However, as explained in section 5.1.1, the system sizes that can be solved using these calculations are very small. Density matrix renormalisation group methods have been applied to the study of continuous FQH states in a spherical geometry [161] and in a narrow channel geometry [162] and in both cases were able to treat systems larger than those that could be treated with exact diagonalisations. In [120] the energy of a variational wave

[1] As stated before, the FQH regime has been reached in an optical lattice where each site contained an isolated continuous FQH system of an average of five atoms [118].

function for the Laughlin state formed of excess particles/holes in the vicinity of the Mott insulator state was calculated using variational Monte Carlo and compared with the energy of the Gutzwiller mean-field vortex lattice.

In [163] the exact matrix product representation of the Laughlin wave function was determined for different values of the filling factor ν, and it was found that there was no efficient description for the bosonic case of $\nu = 1/2$. Recently, it has been shown that both fermionic and bosonic fractional quantum Hall states can be represented using local Grassmann tensor networks [164, 165].

In the following, we will see that the long-range bonds provided by the CPS description allow us to accurately represent the Laughlin wave function with a small number of parameters.

7.2 Exact calculations

We first carry out exact calculations of the system so that we can determine the accuracy of the results found using correlator product states. Previous exact calculations that have compared the ground state with the Laughlin wave function have been carried out in a toroidal geometry, i.e. with periodic boundary conditions, to diminish edge effects and so represent the bulk properties of the system [93, 119].

We carry out our calculations in a disk geometry with hard wall boundary conditions for two reasons. The first reason is that these states are more suitable for being studied with correlator product states. The Laughlin wave function for $\nu = 1/2$ on a torus is given by [166]:

$$\psi_{\mathrm{L}} = \vartheta \begin{bmatrix} (\ell + N - 1)/2 \\ 1 - N \end{bmatrix} (2Z/L|2i) \prod_{i<j} \vartheta \begin{bmatrix} 1/2 \\ 1/2 \end{bmatrix} ((z_i - z_j)/L|i)^2 \qquad (7.1)$$

where Z is the centre-of-mass co-ordinate $\sum_i z_i$, $\ell = 0, 1$ (i.e. there are two degenerate solutions) and where $\vartheta \begin{bmatrix} a \\ b \end{bmatrix} (z|\tau)$ are theta functions. The presence of the centre-of-mass co-ordinate means that the wave function cannot be decomposed into a product of terms dependent on pairs of sites, and thus there is no exact correlator product representation for this state. On the other hand, in a disk geometry the Laughlin wave function is given by equation (4.6), which can be expressed as a product of terms dependent on the number of atoms on each pair of sites, and it has an exact CPS representation [134] which will be described in section 7.3.

The other reason we work in a disk geometry is to better approximate

experimental conditions, where the system is held in a spherically symmetric trap (for the case of a rotating optical lattice). In these experiments edge effects will be present, and since using the CPS representation we hope to reach system sizes comparable with experimental systems, our calculations will be able to represent both a sizeable bulk region and the edge region of the system.

One consequence of working in a disk geometry is that it is unclear how to define the number of magnetic flux quanta [80]. We define the average filling factor of the system as $\nu_{\text{ave}} = N/N_{\phi_{\text{disk}}}$, where N is the number of atoms in the disk, and $N_{\phi_{\text{disk}}}$ is the number of magnetic flux quanta piercing the entire disk of radius R (where R is in units of the lattice periodicity d). The number of magnetic flux quanta per plaquette is then given by $\alpha = N/(\pi R^2 \nu_{\text{ave}})$.

We use the Bose-Hubbard Hamiltonian with the magnetic field given in the symmetric gauge, introduced in equation (4.4),

$$H = \sum_{i,j} \Big\{ -J \left(e^{\mathrm{i}\pi\alpha i}\, \hat{a}^\dagger_{i,j} \hat{a}_{i,j-1} + e^{-\mathrm{i}\pi\alpha j}\, \hat{a}^\dagger_{i,j} \hat{a}_{i-1,j} + \text{h.c.} \right) + \varepsilon_{i,j} \hat{a}^\dagger_{i,j} \hat{a}_{i,j} + \frac{U}{2} \hat{a}^\dagger_{i,j} \hat{a}^\dagger_{i,j} \hat{a}_{i,j} \hat{a}_{i,j} \Big\}, \tag{7.2}$$

with the residual harmonic trapping term $\varepsilon_{i,j}$ set to zero, and allow the atoms to hop within a disk of radius $R = (L+1)/2$ in an $L \times L$ lattice. We first take the hard core limit, where only one atom is allowed on each lattice site. The maximum system size we can reach is five atoms in a 6×6 lattice. We vary the average filling factor ν_{ave} for a given atom number N by varying α, and find the overlap with a discretised $m = 2$ Laughlin wave function. The results are shown in Figure 7.1.

There are two features to note from these plots. The first of these is that the average filling factor ν_{ave} for which good overlap with the Laughlin wave function occurs is smaller than the expected value of $1/2$. This can be explained by considering boundary effects: previous Monte Carlo simulation results in the continuum (for the fermionic case) [167, 168] show that the wave function amplitude falls off at the boundary in width $\sim \ell_B$. To ensure that there are two magnetic flux quanta per atom in the bulk region, we therefore require there to be $2N$ flux quanta in an area $\pi(R - a\ell_B)^2$, where a is a suitably chosen constant. This gives a filling factor $\nu_{\text{ave}} = \left(\sqrt{m} + \frac{a}{\sqrt{2N}} \right)^{-2}$, for an effective filling factor in the bulk region of $\nu_{\text{eff}} = 1/m$. By matching to the data for the exact results, we get $a \approx 1.5$. This reduces to $\nu_{\text{ave}} = 1/m$ in the thermodynamic limit as we would expect, since the ratio of the magnetic length to system size decreases with the number of atoms in the system.

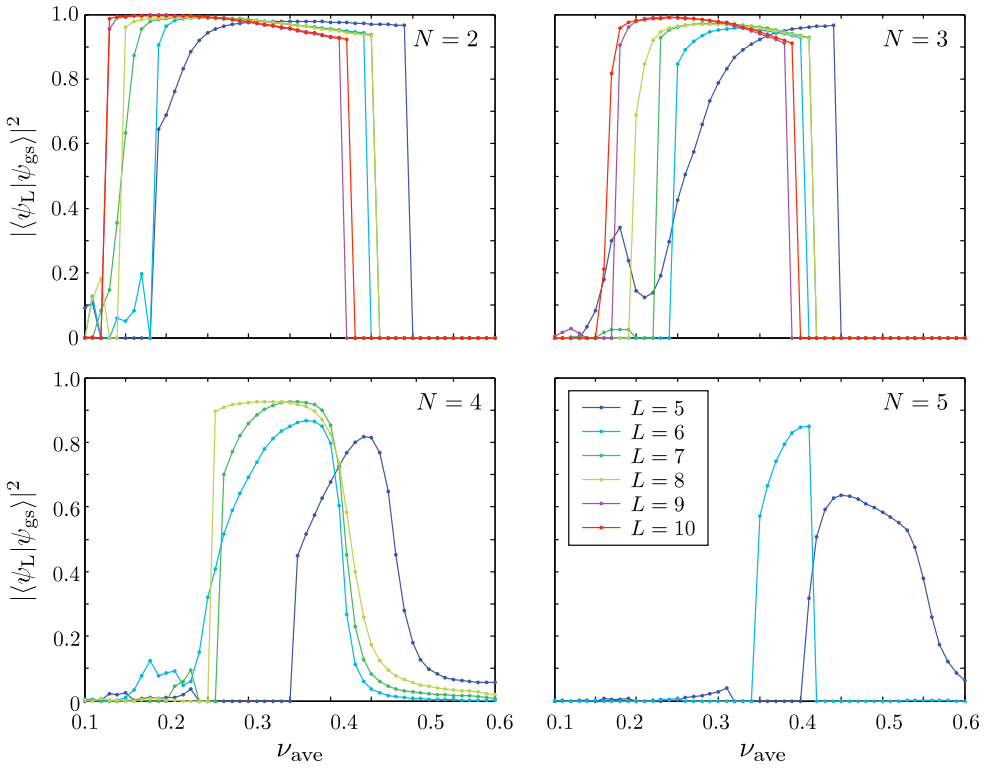

Figure 7.1: Overlap of the ground state in a disk with the Laughlin wave function as a function of average filling factor ν_{ave}.

We also notice from the plots that the width of the region of good overlap decreases with increasing atom number.

We can contrast this behaviour to that in a toroidal geometry, where the filling factor is precisely defined as N/N_ϕ, where the number of magnetic flux quanta in the system N_ϕ is an integer. Here we (and previous calculations [93]) find good overlap with the ground state when $\alpha = 2N/N_p$ is small, N_p being the number of lattice plaquettes.

Taking the optimum value of ν_{ave} determined for each system size for a disk, we consider the overlap as a function α, as has been previously calculated for periodic boundary conditions [93]. As shown in Figure 7.2, we also see good overlap for $\alpha \ll 1$, and a drop off of the overlap as $\alpha \gtrsim 0.25$, similar to the case with periodic boundary conditions.

We also consider the overlap with the Laughlin wave function for a system with a finite on-site interaction i.e. we include the full Hilbert space. Calculations with a finite on-site interaction in a toroidal geometry found that the Laughlin wave function was a good description of the ground state for

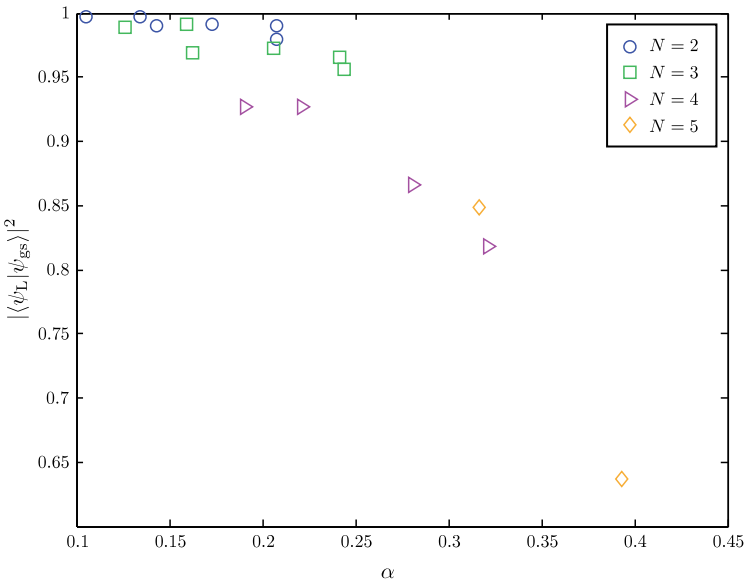

Figure 7.2: Overlap of the ground state in a disk with the Laughlin wave function as a function of the number of magnetic flux quanta per plaquette α.

a non-zero repulsive interaction [119]. Our calculations in a disk geometry are shown in Figure 7.3. We see the same result for a disk, provided that $\alpha \lesssim 0.15$. For large values of α a small value of U/J is required. Note that from an experimental perspective, as described in section 4.3.4, the relevant energy scales are proportional to U, and thus a large value of U is likely to be used in any case.

7.3 CPS representation of the Laughlin wave function

The Laughlin wave function given in equation (4.6), has an exact CPS representation, and it was the existence of this representation which motivated us initially to explore this particular numerical method. The CPS representation of the Laughlin wave function is given by

$$|\psi\rangle = \sum_{\{s\}} \prod_i C_{s_n}^{[1]n} \prod_{n_1<n_2} C_{s_{n_1},s_{n_2}}^{[2]n_1,n_2} \hat{P}_N |s_1 \cdots s_L\rangle,$$

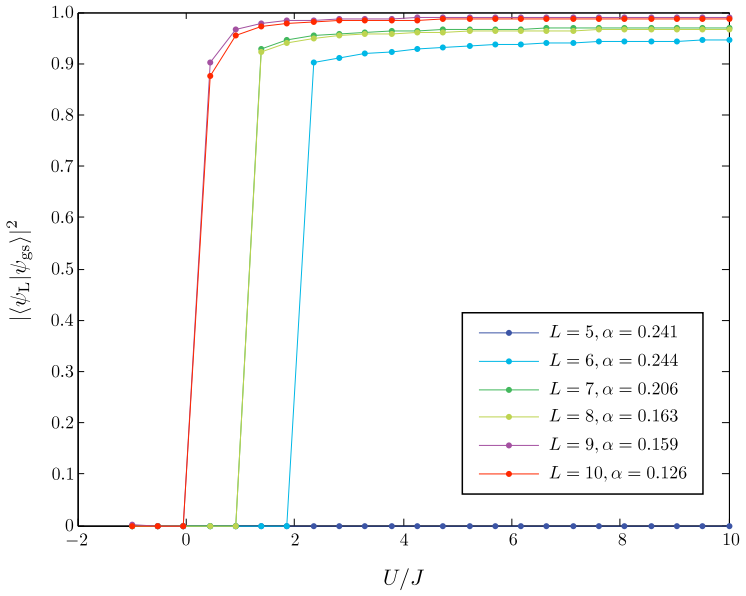

Figure 7.3: Overlap of the ground state in a disk with the Laughlin wave function as a function of the ratio of the on-site interaction energy U to the tunnelling energy J.

with

$$\mathbf{C}^{[1]n} = \begin{pmatrix} 1 \\ \mathrm{e}^{-|z_n|^2/4\ell_B^2} \end{pmatrix}$$

and

$$\mathbf{C}^{[2]n_1,n_2} = \begin{pmatrix} 1 & 1 \\ 1 & (z_{n_1} - z_{n_2})^2 \end{pmatrix}, \tag{7.3}$$

for the hard core bosonic case, and where $\hat{P}_N$ projects onto configurations where $\sum s_n = N$, and where n labels lattice sites with x, y indices i, j. When finite interactions are included, and we allow a maximum of $N_{\max}$ atoms per lattice site, the correlators $C^{[1]n}$ have dimensions $N_{\max} \times 1$ and the correlators $C^{[2]n_1,n_2}$ have dimensions $N_{\max} \times N_{\max}$. Given that the Laughlin wave function acts to prevent any two particles coming together on the same site, when $N_{\max} > 1$ all additional elements are zero. To represent the wave function exactly there must be a bond correlator $C^{[2]n_1,n_2}$ between every pair of sites in the disk, as well as an on-site correlator $C^{[1]n}$ for every site. The correlators $C^{[2]n_1,n_2}$ are defined slightly differently from the bond correlators in Chapter 5. In this case, we use $d_{\max}$ to correspond to the maximum Manhattan distance of the bonds in the system (in Chapter 5, we considered

correlators where the maximum displacement in each direction was $\Delta r_{\max}$). Since the system is not translationally invariant, the same correlator cannot be used to represent all the pairs with a given displacement. Note also that because the Hamiltonian is complex, we must allow the correlators to be complex to find the ground state.

7.3.1 Ground state calculation

To minimise the ground state, we start with a variety of initial correlators: the Laughlin correlator; a uniform correlator; and either of these two cases with varying amounts of random offset. We find that the success of the energy minimisation depends on the choice of initial state, where the best initial state depends on the system parameters.

We apply the minimisation algorithm set out in section 5.3.1. We start with an initial configuration $|s_1, s_2, \cdots, s_M\rangle$, where s_n is the number of atoms on site $n = (i, j)$, and the positions of the atoms are chosen randomly with two constraints: for all values of $N_{\max}$, we ensure that the starting configuration does not contain more than one atom on each site; and we also require atoms to be within 90% of the radius of the disk. We then propose a move by taking each atom in turn, and moving it to any new random position in the disk.

The local interaction energy for each configuration can simply be found by $E_U(\mathbf{s}) = (U/2)\sum_n s_n(s_n - 1)$. Since the tunnelling energy contains off-diagonal terms, the correlator fraction must be calculated. We loop through each lattice site n_1 that contains one or more atoms, and determine all the lattice sites n_2 that an atom can hop to resulting in configuration $\mathbf{s}'$. The local tunnelling energy is then given by

$$E_J(\mathbf{s}) = -J \sum_{n_1,n_2} \frac{W^*(\mathbf{s}')}{W^*(\mathbf{s})} \mathrm{e}^{i\phi_{n_1,n_2}} \sqrt{s_{n_1} s'_{n_2}}, \tag{7.4}$$

where ϕ_{n_1,n_2} is given by $\pi\alpha i(j_2 - j_1) - \pi\alpha j(i_2 - i_1)$.

We calculate the expectation values using the acceptance probability $P_{\text{acc}} = \min\left[\frac{|W(\mathbf{s}')|^2}{|W(\mathbf{s})|^2}, 1\right]$ for each configuration in a slightly different way to that calculated for the 2D Ising model in Chapter 6. Instead of accepting or rejecting the configuration and then calculating the local value of the expectation value for that configuration, the acceptance value is used to calculate the local energy using both the proposed configuration $\mathbf{s}'$ and the current configuration $\mathbf{s}$ as proposed in [169] according to

$$E(\mathbf{s}', \mathbf{s}) = (1 - P_{\text{acc}})E(\mathbf{s}) + P_{\text{acc}}E(\mathbf{s}'). \tag{7.5}$$

This gives the same average as the weighted sum given in section 5.3.1, however the variance is smaller since it reduces the fluctuations caused by accepting unlikely configurations, as well as including information about the unlikely configurations. We find that using this expression leads to a more stable minimisation of the energy, although it does increase the computation time by a factor of $\sim$ 2–4, since the energies of all the configurations need to be calculated, rather than just newly accepted configurations as in the previous case. After the local value is calculated, the configuration is then changed in accordance with P_{acc}. Once the derivative is calculated, all the correlators are updated simultaneously.

While minimising the energy, we encounter the same difficulties as for bond correlators in the case of the 2D Ising model. Since the Hamiltonian is complex and we know this is a system that supports highly non-trivial frustrated states, this system is more complicated than the 2D Ising model, therefore it is understandable that we encounter numerous local minima. As described above, the minimisation can be vastly improved by starting with an appropriate initial state. One factor that contributes to the difficulty of minimising the energy is that unlike with plaquette correlators used in Chapter 6, there is no simple way to build a larger correlator from the small correlator case, thus generating a suitable starting state when there are many parameters.[2]

7.4 Results

This section presents preliminary results for finding the ground state in a rotating lattice subject to an artificial magnetic field. Note that these results are generated using a simple non-optimised MATLAB code, and so it is expected that we will eventually be able to reach larger system sizes than those presented here once a C version of the code is constructed.

We first apply the minimisation procedure to three atoms in a 9×9 lattice, so that we can compare the results with those from an exact calculation of section 7.2 above. For these parameters, $\nu_{\text{ave}} = 0.24$ to give $\nu_{\text{eff}} = 1/2$, $\alpha = 0.159$, and the overlap with the Laughlin wave function is 0.99. Although we need correlators for all pairs of sites to describe the Laughlin wave function exactly, given that we know that the minimisation problem becomes more difficult the more bonds we have, we investigate how well the CPS

[2]With plaquette correlators a larger correlator is built from a smaller correlator by tiling the smaller plaquettes over the larger plaquette area. With bond correlators we are instead adding a new link to the system (rather than replacing one correlator with another).

representation can approximate the ground state as $d_{\max}$ is varied ($d_{\max} = 0$ corresponds to a product of the on-site correlators $C^{[1]n}$). We allow moves to configurations in the entire Hilbert space i.e. $N_{\max} = 3$, and set $U/J = 10$, which ensures that for the correct filling factor, there will be a good overlap with the Laughlin wave function. We find the best convergence with an initial minimisation having $F_0 = 50, G_0 = 10, \delta_0 = 0.005$ and $\eta = 0.75$, and then a second round of minimisation (i.e. with the iteration number reset) with the step size δ_0 reduced to 0.001 and η increased to 0.9.

ν_{ave}	GS energy	$d_{\max}$	Estimated energy	Exact energy	Overlap
0.24	-3.112	0	-2.77(1)	-2.771	0.000
		3	-3.053(4)	-3.054	0.130
		6	-3.079(4)	-3.078	0.265
		9	-3.100(3)	-3.100	0.972
		12	-3.109(2)	-3.109	0.995
1	-3.620	0	-3.590(7)	-3.584	0.955
		6	-3.617(2)	-3.616	0.999
		12	-3.618(2)	-3.617	1.000
5	-3.698	0	-3.672(5)	-3.668	0.954
		6	-3.695(2)	-3.694	0.999
		12	-3.696(2)	-3.695	1.000
10	-3.700	0	-3.675(5)	-3.671	0.954
		6	-3.697(2)	-3.697	0.999
		12	-3.698(2)	-3.698	0.999

Table 7.1: Results for 3 atoms in a 9×9 lattice, with finite on-site interaction $U/J = 10$. The energy per atom is given in units of J. The exact energy and the overlap are found by rebuilding the wave function using the minimised correlator elements. $\nu_{\text{ave}} = 0.24$ corresponds to $\nu_{\text{eff}} = 0.5$. At $\nu_{\text{eff}} = 0.5$, the Laughlin wave function has energy per atom -3.106J, and the overlap of the ground state with the Laughlin wave function is 0.990.

For comparing results with the exact case, we rebuild the full many-body wave function using the correlators according to equation (7.3). We calculate the exact energy for comparison with the energy estimated from Monte Carlo sampling, as well as the overlap with the ground state determined from an exact diagonalisation of the Hamiltonian. Note that we cannot estimate an overlap with the CPS representation using sampling, as the calculation does not assume any knowledge of the normalisation of the wave function.

As well as considering a filling factor ν_{ave} where we expect a good overlap with the Laughlin wave function, we also consider larger filling factors, so

we can compare how well the correlator product description works outside of the strongly correlated regime. The results are summarised in Table 7.1.

When the ground state of the system is a strongly correlated state (i.e. at $\nu_{\text{ave}} = 0.24$), we see that the overlap is zero for $\Delta r_{\max} = 0$, and that the CPS representation becomes a good description of the system as the number of correlators is increased. However even using bonds up to a distance of 6 sites in a 9×9 system leads to a poor overlap. This suggests that the Laughlin state, being a highly entangled state, requires very long range correlators for an accurate description. As the filling factor is increased, we see that the system can now be very well described by short-range correlators, indicating that the system is no longer in a strongly correlated state. The product state ($d_{\max} = 0$) is also a good representation of the ground state in this regime, although even for the largest filing factor it does not provide as good a description as the CPS with short-range bonds since it entirely neglects correlations.

We also look at minimising the energy for a large system that cannot be solved exactly. We consider the case of ten atoms in a 15×15 lattice. As before, we allow any configuration in the full Hilbert space i.e. up to ten atoms on a single site, and take $U/J = 10$. For these parameters, $\nu_{\text{ave}} = 0.33$ to give $\nu_{\text{eff}} = 1/2$, and $\alpha = 0.151$ so the Laughlin wave function should still be a good description of the state.

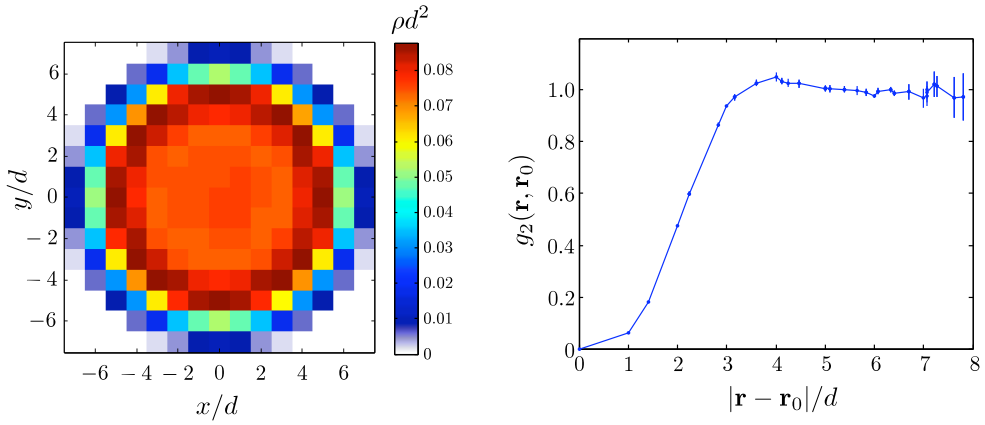

Figure 7.4: Density and correlation function of the Laughlin state for ten atoms in a 15×15 lattice found by sampling the CPS representation of the Laughlin wave function. $\mathbf{r}_0$ is the central lattice site. For these parameters $\ell_B = 1.03d$.

We first calculate the density, g_2 correlation function and energy of the Laughlin state using the correlators given in equation (7.3) for comparison

with the estimated ground state, where the g_2 correlation function is given by

$$g_2(\mathbf{r},\mathbf{r}') = \frac{\langle a^\dagger_{\mathbf{r}} a^\dagger_{\mathbf{r}'} a_{\mathbf{r}'} a_{\mathbf{r}}\rangle}{\langle a^\dagger_{\mathbf{r}} a_{\mathbf{r}}\rangle \langle a^\dagger_{\mathbf{r}'} a_{\mathbf{r}'}\rangle} \tag{7.6}$$

$$= \frac{\langle a^\dagger_{\mathbf{r}'} a_{\mathbf{r}'} a^\dagger_{\mathbf{r}} a_{\mathbf{r}}\rangle - \delta_{\mathbf{r},\mathbf{r}'}\langle a^\dagger_{\mathbf{r}} a_{\mathbf{r}}\rangle}{\langle a^\dagger_{\mathbf{r}} a_{\mathbf{r}}\rangle \langle a^\dagger_{\mathbf{r}'} a_{\mathbf{r}'}\rangle}. \tag{7.7}$$

The energy is found to be $-3.15(1)J$ per atom, and the density and g_2 correlation function are shown in Figure 7.4. For these plots, there are FN sweeps and a single sample, with $F = 10^7$. As expected, the density shows a small flat central region with density $\rho = \alpha\nu_{\text{eff}}/d^2 = 1/4\pi\ell_B^2$, with an edge region that is a small multiple of the magnetic length. The g_2 correlation function shows that there is zero probability of finding two atoms at the same point. There is a small ridge around $|\mathbf{r} - \mathbf{r}_0| = \ell_B\sqrt{4\pi}$ consistent with the uniform density of the cloud.

We then minimise the energy, using different values of $d_{\max}$ as we did for the small system. The results after a single run of the minimisation routine with $F_0 = 50, G_0 = 10, \delta_0 = 0.001$ and $\eta = 0.75$ are shown in Figure 7.5 for $\nu_{\text{ave}} = 0.33$ and in Figure 7.6 for $\nu_{\text{ave}} = 10$. The minimisation routine was run for the same time for each type of correlator, and the estimated energy is plotted as a function of scaled iteration number. Also shown are the g_2 correlation function and the density for each value of $d_{\max}$.

For $\nu_{\text{ave}} = 0.33$ we see a large difference in the final energy as a function of $d_{\max}$. When $d_{\max} = 22$ (the size required to cover every pair of sites in the system) the final energy is the same as the energy of the Laughlin state (within the error). For $d_{\max} = 17$ we see the final energy is also close to the energy of the Laughlin state. We see a small departure for the shorter range correlators, and a very large difference for a simple product state. The plot also highlights that for the product and short range correlators we did not start with an initial state close to the ground state (best convergence was achieved with a uniform initial state), whereas we were able to do so with the longer range correlators by using the Laughlin CPS representation as an initial state.

The minimum energy found is consistent with the expectation value of g_2 for each value of $d_{\max}$: the two longest range correlators show the dependence we would expect for a Laughlin state, while the short range and product correlators show a non-zero probability of two atoms being found on the same site. The density plots for $d_{\max} = 0, 6, 11$ have a strange profile, and it is not clear to what extent this results from the correlators themselves being

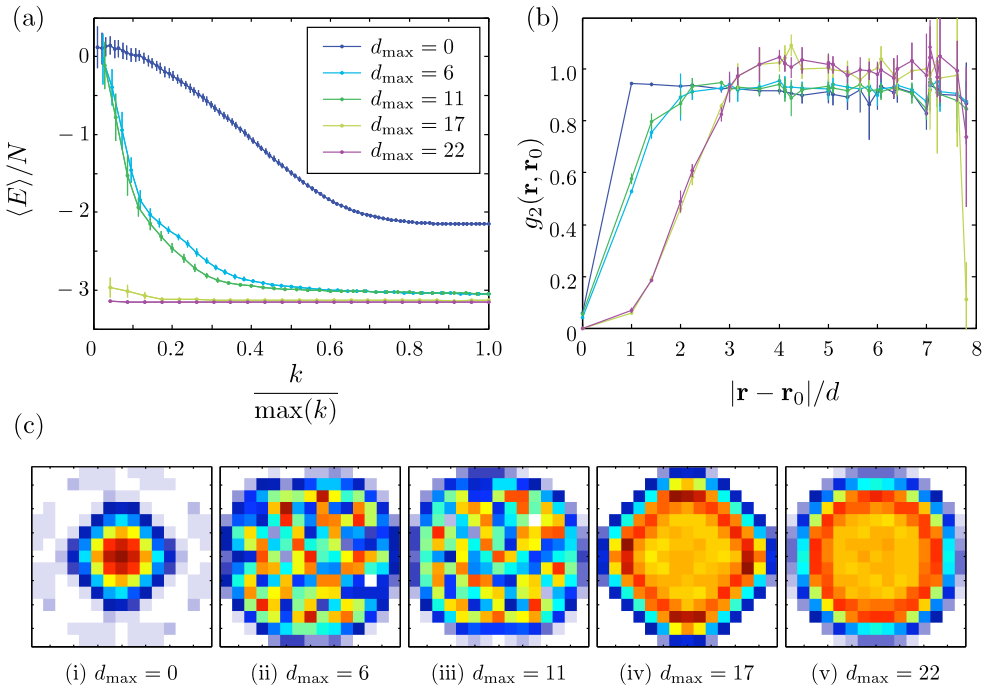

Figure 7.5: (a) Energy minimisation, (b) correlation function and (c) density of a ten atom correlator product state at $\nu_{\text{ave}} = 0.33$ ($\nu_{\text{eff}} = 1/2$) in a 15×15 lattice, for different correlator bond lengths. Note that the density plots are not all shown at the same colour scale, and the plots are scaled relative to a maximum density ρd^2 of (i) 0.37; (ii) and (iii) 0.13; (iv) and (v) 0.10.

unable to describe the ground state, or imperfect minimisation resulting in the system getting stuck in a local minimum (the density profiles for the small system show similar behaviour for product and short range correlators). The density found using correlators with $d_{\max} = 17$ is approaching the density we would expect for the ground state (and that for $d_{\max} = 22$) although there are still noticeable differences.

For $\nu_{\text{ave}} = 10$, we see that all the correlators with $d_{\max} \neq 0$ have similar density profiles, g_2 correlation functions and minimised energies. For $d_{\max} = 0$ there is a small energy difference (note the difference in the energy scale between Figures 7.5 and 7.6), but the density and g_2 correlation function are qualitatively the same. This is what we would expect when the atoms no longer form a state with long-range correlations.

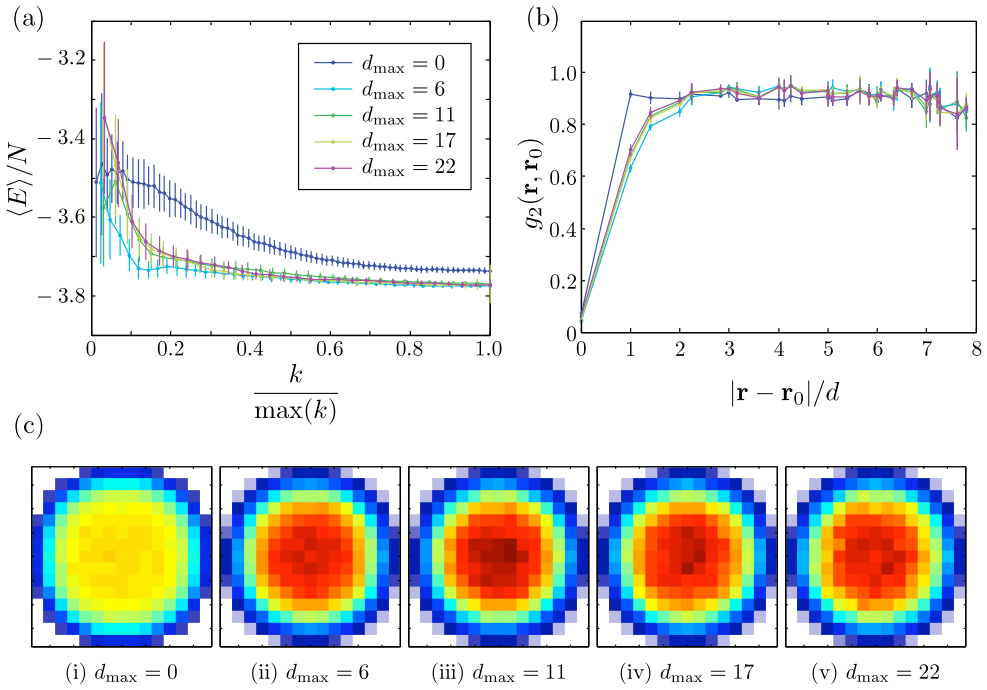

Figure 7.6: (a) Energy minimisation, (b) correlation function and (c) density of a ten atom correlator product state at $\nu_{\text{ave}} = 10$ in a 15×15 lattice, for different correlator bond lengths. The density plots are scaled relative to a maximum density ρd^2 of 0.105

7.5 Further work

We have investigated the CPS representation of the ground state for large systems in an optical lattice subject to an artificial magnetic field. Although the system sizes treated are not comparable to realistic experimental sizes, we expect to be able to treat larger systems with optimised code. To our knowledge these are the largest system sizes for which ground state calculations have been carried out in this regime. To represent FQH states with PEPS would require a very large bond dimension, and it is unlikely that systems of this size could be reached.

Our calculations have shown that at $\nu_{\text{eff}} = 1/2$, correlators between all sites are needed to accurately represent the ground state. We have encountered complexities in finding the ground state, which are reduced if an appropriate initial state is chosen. Thus improved estimates may be obtained by trying different forms of starting state other than the random, uniform or Laughlin state correlators used here.

These preliminary results are promising, however many questions remain about how well the CPS representation describes FQH states in optical lattices. We have concentrated on calculations in the low field regime $\alpha < 0.2$, and it would be interesting to see whether this method can be adapted to yield accurate results in the high field regime [96, 121] where the Laughlin wave function is no longer a good description of the ground state. We have carried out calculations in small systems following the method given above for states with $\alpha \sim 0.5$ and have been unable minimise to the ground state energy. However, given the flexibility available for the types of correlators we can use, it can be investigated whether different correlator types (such as plaquettes) represent the high α states more accurately. We have also only considered the $\nu_{\text{eff}} = 1/2$ FQH state. It could be investigated whether the higher density FQH states can be represented by correlator product states, and if so the transition from a vortex lattice to the FQH regime could then be investigated in large systems with the numerical methods presented here.

Chapter 8

Summary and conclusions

In this thesis we have experimentally and theoretically investigated systems of ultracold atoms in optical lattices for simulating condensed matter systems.

8.1 Summary of results

We demonstrated the first use of an optical lattice with dynamically variable periodicity for expanding the optical lattice whilst keeping the atoms trapped. This system can be used to perform quantum simulation experiments at a lattice spacing smaller than the resolution of the imaging system, and then 'magnify' the system for single-site detection. We found that the optical lattice spacing could be varied from 2.2 to 5.5 μm in a few milliseconds whilst the atoms remained trapped.

We also analysed experimental results obtained from the rotating optical lattice with many hundreds of atoms per lattice site. In these experiments, when the optical lattice potential was deep the system was analogous to two-dimensional Josephson-junction array in a magnetic field. We solved the time-dependent GPE in the rotating frame to illustrate the new method for vortex nucleation demonstrated in the experiment. We also investigated numerically rotation above the harmonic trapping frequency in deep lattices, and found evidence for self trapping of the condensate which prevented the atoms being lost from the trap.

We investigated a recently proposed method that could be used to efficiently numerically describe strongly correlated states [134, 135], so-called correlator product states (CPS), where we calculated the ground state using a stochastic minimisation technique [152, 153]. We first applied this description to the two-dimensional quantum Ising model in a transverse magnetic

field. We compared the results obtained using correlator product states with exactly found results for a 6×6 system and found good agreement when larger CPS were used. We were able to describe the essential features of the model in up to a 51×51 system using small plaquette correlators. We then investigated the use of different CPS types in 31×31 system and found that larger CPS were able to describe the long-range correlations present around the transition point. We found that far from the transition point short range CPS were able to describe the ground state to a similar degree of accuracy as longer range CPS.

We then applied the correlator product state description to the Bose-Hubbard Hamiltonian in a magnetic field, in the regime in which FQH states are predicted to occur, motivated by the fact that the Laughlin wave function has an exact correlator product state representation. We first outlined exact diagonalisation calculations carried out in a disk geometry where the Laughlin wave function was found to be a good description of the ground state. We then compared the exactly found ground state with the ground state found by stochastic minimisation of different sized CPS. We found that correlators between every pair of sites in the system were required to accurately describe the ground state when the Laughlin wave function was a good description. However at lower magnetic fields we found that the ground state could be described well with short range CPS. We then applied the method to a system consisting of ten atoms in a 15×15 system, which is much larger than the systems that can be solved exactly. Similarly to the small system size, we found that short range CPS could not describe the ground state of the system in the strongly correlated regime, although a correlator range of around 75% of the maximum site separation in the system could reproduce the essential features of the ground state.

8.2 Future prospects

In any future optical lattice experiments it would be preferable to move to a system with a smaller lattice periodicity, to allow us to reach the strongly correlated regime where the site filling is of order one. This could be achieved by using a higher numerical aperture lens and/or a blue-detuned optical lattice. Fluorescence imaging in combination with the accordion lattice could be employed to allow single-atom imaging of these strongly correlated regimes. However, as discussed in Chapter 4, reaching the FQH regime in a rotating optical lattice requires some challenging constraints to be met.

The next step after observation of FQH states in an optical lattice (for example by measurement of the two-point correlation function), would be

detection of fractionally charged excitations. It has been proposed that the 1/2-statistics of excitations of the Laughlin state could be created and manipulated using focussed lasers [170]. Looking even further into the future, some of the higher density FQH states (e.g. the $\nu = 3/2$ Read-Rezayi sate) are predicted to support non-Abelian statistics, and there are proposals to use these for topological quantum computation [171]. These systems would form intrinsically fault-tolerant quantum computers as they are not affected by local noise.

The flexible optical lattice could be modified to realise different types of model Hamiltonians. A rotating triangular lattice could be generated using three AODs mounted at 120° to one another, each AOD generating a beam that rotates around the optical lattice in the same way as with the current arrangement. The AODs could then be driven with the same RF signal, to ensure that the frequencies applied to the AODs are in phase with one another, and thus that the lattice beams have the same frequency and so interfere with one another. The optical lattice beams could also be controlled to provide different types of dynamic Hamiltonian, such as 'shaking' the optical lattice potential as described in section 3.2.3 which can be used to control both the magnitude and sign of the tunnelling term. Elliptical acceleration of a triangular optical lattice has been proposed for modelling frustrated antiferromagnets using spinless bosons [172]. For certain parameters these can realise a gapped spin liquid phase, which may also be a candidate for topological quantum computing.

The results from the CPS calculations are very promising, and there are still many questions to be explored. Given the flexibility with which correlator product states can be arranged, they are ideally suited to comparing the behaviour of systems in different lattice geometries. The work on representing the FQH states in optical lattices with correlator product states is encouraging and it will be interesting to see to what extent these states can represent states other than the continuum Laughlin state. A deterministic method for calculating the CPS ground state has been proposed [150]. This method relies on the fact that a correlator on a given site will only affect a small subset of the remaining sites in the lattice, so it is not suitable for representing FQH states. However it could be useful for other systems, for example for exploring the superfluid to Mott insulator transition in two-dimensional systems.

In terms of the next steps in quantum simulation, there has been a lot of work in preparing quantum gases of ground-state polar molecules with strong electric dipole moments [173]. When loaded into optical lattices, the long-range dipolar interactions can be used to realise a much larger variety of condensed matter models than can realised with ultracold atoms. For

example, it has been predicted that polar molecules in optical lattices can be used to realise Mott Insulator phases at rational fillings and supersolid phases [174, 175]. The larger spin-spin coupling achievable with cold polar molecules would also lead to a more robust implementation of spin models than that mediated by the spin exchange coupling for atoms described in section 1.3.2, and in [176] it was proposed how a complete toolbox for effective two-spin interactions with tuneable range, spatial anisotropy and large coupling strengths could be realised using polar molecules in optical lattices. There are also many interesting possibilities to perform simulation experiments even without optical lattices. A 2D gas of fermionic molecules can also be used to realise p-wave superfluids [177] which have topological properties related to those of the FQH states.

Quantum simulation is a flourishing area, and the tools that are being developed will be able to investigate strongly correlated states in new ways.

Appendix A

Atomic transitions in ^{87}Rb

Figure A.1 illustrates the hyperfine structure of the ground and first excited states in ^{87}Rb.

The light for laser cooling is frequency detuned by $\Delta = -15$ MHz below the $F = 2$ – $F' = 3$ transition. There is a 0.4% probability that the laser cooling light will also excite atoms to the $F' = 2$ hyperfine level, from which they can decay to the $F = 1$ hyperfine level and be lost from the cooling cycle. The repumping light excites these atoms back to the $F' = 2$ level, forming a closed cycling transition.

The optical pumping beam is σ^- polarised with respect to a quantisation axis provided by the small bias field one of the shim coil pairs, and transfers atoms to the low-field seeking $F = 1, m_F = -1$ Zeeman sub-level for magnetic trapping. For imaging the atoms, the repumping beam is first applied to transfer atoms back to the F = 2 hyperfine level, before the probing beam is applied.

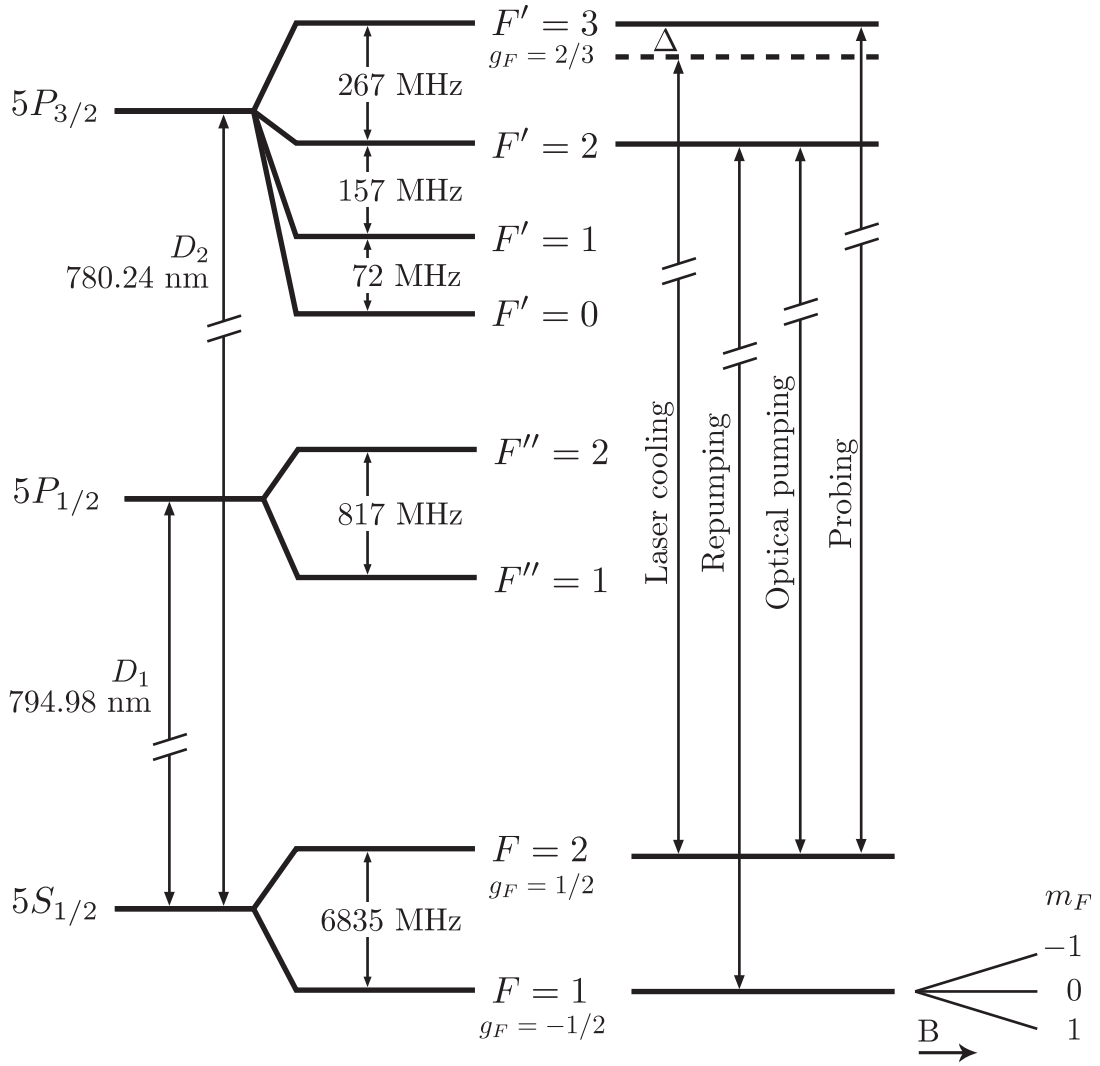

Figure A.1: Hyperfine levels of the ground and first excited states in ^{87}Rb, and the transitions used for during the experimental sequence.

Appendix B

The time-splitting spectral method

For simulations of atoms in the optical lattice in the mean-field regime where there are several hundred atoms per lattice site, we solve the time dependent GPE numerically using the time-splitting spectral method.

B.1 Stationary optical lattice

For a non-rotating optical lattice potential V_L, we solve the time-dependent GPE in the lab frame following the procedure outlined in [178]. The dimensionless time-dependent GPE is given by

$$i\frac{\partial}{\partial\tilde{t}}\tilde{\psi}(\tilde{x},\tilde{y},\tilde{t}) = \left[\frac{1}{2}(\tilde{p}_x^2+\tilde{p}_y^2)+\frac{1}{2}(\tilde{x}^2+\tilde{y}^2)+\tilde{V}(\tilde{t})+\beta|\tilde{\psi}(\tilde{x},\tilde{y},\tilde{t})|^2\right]\tilde{\psi}(\tilde{x},\tilde{y},\tilde{t}), \tag{B.1}$$

where we have assumed that the axial motion is frozen out. The dimensionless units are given in terms of the radial harmonic trapping frequency ω_r

and the radial magnetic length $a_r = \sqrt{\hbar/M\omega_r}$ as:

$$\begin{aligned}
(\tilde{x}, \tilde{y}) &= \frac{(x, y)}{a_r}, \\
(\tilde{p}_x, \tilde{p}_y) &= \frac{(p_x, p_y)a_r}{\hbar}, \\
\tilde{\psi}(\tilde{x}, \tilde{y}, \tilde{t}) &= a_{ho}\psi(x, y, t), \quad \text{so that } \int |\tilde{\psi}(\tilde{x}, \tilde{y}, \tilde{t})|^2 \, \mathrm{d}\tilde{x}\mathrm{d}\tilde{y} = 1, \\
\tilde{t} &= \omega_r t, \\
\tilde{V}(\tilde{x}, \tilde{y}, \tilde{t}) &= \frac{V_L(x, y, t)}{\hbar\omega_r}.
\end{aligned}$$

The two-dimensional interaction parameter β is given by $\sqrt{8\pi}a_s N/a_z$ in the weakly interacting regime (by assuming a Gaussian profile in the axial direction), and by $\frac{5}{7}(gN\omega_z/a_r^3\hbar\omega_r^2)^{\frac{4}{5}}(4\pi/15)^{\frac{1}{5}}$ in the strongly interacting regime (by assuming a Thomas-Fermi distribution). In our calculations, we take β as a constant for the entire routine, however note that this is not entirely accurate, since the axial extent of the cloud will change as the optical lattice is ramped up due to the increased interaction energy. For our experimental parameters, using the expression for the strongly interacting case, $\beta \sim 1000$, and it will vary depending on the lattice depth, axial trapping frequency and number of atoms.

To solve equation (B.1), we split the Hamiltonian in two parts: those that are diagonal in the momentum, and those that are diagonal in the position. We solve the time evolution in between time t_n and $t_n + \Delta_t$ in the steps:

$$i\frac{\partial}{\partial\tilde{t}}\widehat{\psi}(\tilde{p}_x, \tilde{p}_y, \tilde{t}) = \frac{1}{2}(\tilde{p}_x^2 + \tilde{p}_y^2)\widehat{\psi}(\tilde{p}_x, \tilde{p}_y, \tilde{t}),$$

between t_n and $t_n + \Delta_t/2$;

$$i\frac{\partial}{\partial\tilde{t}}\tilde{\psi}(\tilde{x}, \tilde{y}, \tilde{t}) = \left[\frac{1}{2}(\tilde{x}^2 + \tilde{y}^2) + \tilde{V}(\tilde{t}) + \beta|\tilde{\psi}(\tilde{x}, \tilde{y}, \tilde{t}_n)|^2\right]\tilde{\psi}(\tilde{x}, \tilde{y}, \tilde{t})$$

between t_n and $t_n + \Delta_t$; and

$$i\frac{\partial}{\partial\tilde{t}}\widehat{\psi}(\tilde{p}_x, \tilde{p}_y, \tilde{t}) = \frac{1}{2}(\tilde{p}_x^2 + \tilde{p}_y^2)\widehat{\psi}(\tilde{p}_x, \tilde{p}_y, \tilde{t})$$

between $t_n + \Delta_t/2$ and $t_n + \Delta_t$. $\widehat{\psi}(\tilde{p}_x, \tilde{p}_y, \tilde{t})$ is the momentum space representation of $\tilde{\psi}(\tilde{x}, \tilde{y}, \tilde{t})$. Each step of the evolution can thus be integrated exactly,

and using a half-step scheme reduces the error associated with the splitting to Δ_t^3. In our calculations, we use the MATLAB Fast Fourier Transform (FFT) to find $\widehat{\psi}(\tilde{p}_x, \tilde{p}_y, \tilde{t})$.

B.2 Rotating optical lattice

When moving to the rotating frame, we subtract ΩL_z from the Hamiltonian, which contains cross terms of the position and momentum. This means we can no longer apply the same splitting method as was used above. We follow the procedure outlined in [179] to evolve the wave function. The dimensionless time-dependent GPE in the rotating frame is given by

$$i\frac{\partial}{\partial\tilde{t}}\tilde{\psi}(\tilde{x},\tilde{y},\tilde{t}) = \left[\frac{\tilde{p}_x^2+\tilde{p}_y^2}{2} + \tilde{\Omega}(\tilde{y}\tilde{p}_x - \tilde{x}\tilde{p}_y) + \frac{\tilde{x}^2+\tilde{y}^2}{2} + \tilde{V}(\tilde{t}) + \beta|\tilde{\psi}(\tilde{x},\tilde{y},\tilde{t})|^2\right]\tilde{\psi}(\tilde{x},\tilde{y},\tilde{t}), \tag{B.2}$$

where $\tilde{\Omega}$ is the scaled rotation frequency Ω/ω_r. To solve equation (B.2) we transform into x-momentum space and y-momentum space in separate steps by solving:

$$i\frac{\partial}{\partial\tilde{t}}\widehat{\psi}(\tilde{p}_x,\tilde{y},\tilde{t}) = \frac{1}{2}(\tilde{p}_x^2 + \tilde{\Omega}\tilde{y}\tilde{p}_x)\widehat{\psi}(\tilde{p}_x,\tilde{y},\tilde{t}),$$

between t_n and $t_n + \Delta_t/2$;

$$i\frac{\partial}{\partial\tilde{t}}\widehat{\psi}(\tilde{x},\tilde{p}_y,\tilde{t}) = \frac{1}{2}(\tilde{p}_y^2 - \tilde{\Omega}\tilde{x}\tilde{p}_y)\widehat{\psi}(\tilde{x},\tilde{p}_y,\tilde{t}),$$

between t_n and $t_n + \Delta_t/2$;

$$i\frac{\partial}{\partial\tilde{t}}\tilde{\psi}(\tilde{x},\tilde{y},\tilde{t}) = \left[\frac{1}{2}(\tilde{x}^2+\tilde{y}^2) + \tilde{V}(\tilde{t}) + \beta|\tilde{\psi}(\tilde{x},\tilde{y},\tilde{t}_n)|^2\right]\tilde{\psi}(\tilde{x},\tilde{y},\tilde{t})$$

between t_n and $t_n + \Delta_t$;

$$i\frac{\partial}{\partial\tilde{t}}\widehat{\psi}(\tilde{p}_x,\tilde{y},\tilde{t}) = \frac{1}{2}(\tilde{p}_x^2 + \tilde{\Omega}\tilde{y}\tilde{p}_x)\widehat{\psi}(\tilde{p}_x,\tilde{y},\tilde{t}),$$

between $t_n + \Delta_t/2$ and $t_n + \Delta_t$; and

$$i\frac{\partial}{\partial\tilde{t}}\widehat{\psi}(\tilde{x},\tilde{p}_y,\tilde{t}) = \frac{1}{2}(\tilde{p}_y^2 - \tilde{\Omega}\tilde{x}\tilde{p}_y)\widehat{\psi}(\tilde{x},\tilde{p}_y,\tilde{t}),$$

between $t_n + \Delta_t/2$ and $t_n + \Delta_t$. As before, each step of the evolution can be integrated exactly.

Bibliography

[1] Z. F. Ezawa. *Quantum Hall effects: Field Theoretical Approach and Related Topics*. World Scientific, Singapore, first edition, 2008.

[2] R. E. Prange and S. M. Girvin. *The Quantum Hall Effect*. Springer-Verlag, New York, second edition, 1987.

[3] P. A. Lee, N. Nagaosa, and X.-G. Wen. Doping a Mott insulator: Physics of high-temperature superconductivity. *Rev. Mod. Phys.*, 78:17, 2006.

[4] R. Feynman. Simulating physics with computers. *Int. J. Theor. Phys.*, 21:467.

[5] S. Lloyd. Universal Quantum Simulators. *Science*, 273:1073, 1996.

[6] I. Buluta and F. Nori. Quantum Simulators. *Science*, 326:108, 2009.

[7] M. Anderson, J. R. Ensher, M. R. Matthews, C. E. Wieman, and E. A. Cornell. Observation of Bose-Einsten condensation in a dilute atomic vapor. *Science*, 269:198, 1995.

[8] K. B. Davis, M.-O. Mewes, M. R. Andrews, N. J. van Druten, D. S. Durfee, D. M. Kurn, and W. Ketterle. Bose-Einstein condensation in a gas of sodium atoms. *Phys. Rev. Lett.*, 75:3969, 1995.

[9] C. C. Bradley, C. A. Sackett, J. J. Tollett, and R. G. Hulet. Evidence of Bose-Einstein Condensation in an Atomic Gas with Attractive Interactions. *Phys. Rev. Lett.*, 75:1687, 1995.

[10] M. R. Andrews, C. G. Townsend, H.-J. Miesner, D. S. Durfee, D. M. Kurn, and W. Ketterle. Observation of Interference Between Two Bose Condensates. *Science*, 275:637, 1997.

[11] I. Bloch, T. W. Hänsch, and T. Esslinger. Measurement of the spatial coherence of a trapped Bose gas at the phase transition. *Nature*, 403:166, 2000.

[12] M. R. Matthews, B. P. Anderson, P. C. Haljan, D. S. Hall, C. E. Wieman, and E. A. Cornell. Vortices in a Bose-Einstein Condensate. *Phys. Rev. Lett.*, 83:2498–2501, 1999.

[13] O. M. Maragò, S. A. Hopkins, J. Arlt, E. Hodby, G. Hechenblaikner, and C. J. Foot. Observation of the Scissors Mode and Evidence for Superfluidity of a Trapped Bose-Einstein Condensed Gas. *Phys. Rev. Lett.*, 84:2056–2059, 2000.

[14] P. Courteille, R. S. Freeland, D. J. Heinzen, F. A. van Abeelen, and B. J. Verhaar. Observation of a Feshbach Resonance in Cold Atom Scattering. *Phys. Rev. Lett.*, 81:69, 1998.

[15] S. Inouye, M. R. Andrews, J. Stenger, H.-J. Miesner, D. M. Stamper-Kurn, and W. Ketterle. Observation of Feshbach resonances in a Bose-Einstein condensate. *Nature*, 392:151, 1998.

[16] D. Jaksch, C. Bruder, J. I. Cirac, C. W. Gardiner, and P. Zoller. Cold Bosonic Atoms in Optical Lattices. *Phys. Rev. Lett.*, 81:3108, Jan 1998.

[17] M. Greiner, O. Mandel, T. Esslinger, T. W. Hänsch, and I. Bloch. Quantum phase transition from a superfluid to a Mott insulator in a gas of ultracold atoms. *Nature*, 415:39, 2002.

[18] R. Jördens, N. Strohmaier, K. Günter, H. Moritz, and T. Esslinger. A Mott insulator of fermionic atoms in an optical lattice. *Nature*, 455:204, 2008.

[19] U. Schneider, L. Hackermueller, S. Will, T. Best, I. Bloch, T. A. Costi, R. W. Helmes, D. Rasch, and A. Rosch. Metallic and Insulating Phases of Repulsively Interacting Fermions in a 3D Optical Lattice. *Science*, 322:1520, Jan 2008.

[20] M. Lewenstein, A. Sanpera, V. Ahufinger, B. Damski, A. Sen, and U. Sen. Ultracold atomic gases in optical lattices: mimicking condensed matter physics and beyond. *Adv. Phys.*, 56:243, 2007.

[21] I. Bloch, J. Dalibard, and W. Zwerger. Many-body physics with ultracold gases. *Rev. Mod. Phys.*, 80:885, 2008.

[22] D. Jaksch and P. Zoller. The cold atom Hubbard toolbox. *Ann. Phys.*, 315:52, 2005.

[23] S. Viefers. Quantum Hall physics in rotating Bose–Einstein condensates. *Journal of Physics: Condensed Matter*, 20:123202, 2008.

[24] M. Greiner, I. Bloch, O. Mandel, T. W. Hänsch, and T. Esslinger. Exploring Phase Coherence in a 2D Lattice of Bose-Einstein Condensates. *Phys. Rev. Lett.*, 87:160405, 2001.

[25] W. S. Bakr, A. Peng, M. E. Tai, R. Ma, J. Simon, J. I. Gillen, S. Folling, L. Pollet, and M. Greiner. Probing the Superfluid-to-Mott Insulator Transition at the Single-Atom Level. *Science*, 329:547, 2010.

[26] J. F. Sherson, C. Weitenberg, M. Endres, M. Cheneau, I. Bloch, and S. Kuhr. Single-Atom Resolved Fluorescence Imaging of an Atomic Mott Insulator. *Nature*, 467:68, 2010.

[27] S. Fölling, F. Gerbier, A. Widera, O. Mandel, T. Gericke, and I. Bloch. Spatial quantum noise interferometry in expanding ultracold atom clouds. *Nature*, 434:481, 2005.

[28] T. Rom, T. Best, D. van Oosten, U. Schneider, S. Fölling, B. Paredes, and I. Bloch. Free fermion antibunching in a degenerate atomic Fermi gas released from an optical lattice. *Nature*, 444:733, 2006.

[29] E. Gross. Structure of a quantized vortex in boson systems. *Il Nuovo Cimento (1955-1965)*, 1961.

[30] L. P. Pitaevskii. Vortex Lines in an Imperfect Bose Gas. *Sov. Phys. JETP*, 13:451, 1961.

[31] A. Leggett. Bose-Einstein condensation in the alkali gases: Some fundamental concepts. *Rev. Mod. Phys.*, 73:307, 2001.

[32] C. J. Pethick and H. Smith. *Bose-Einstein Condensation in Dilute Gases*. Cambridge University Press, Cambridge, second edition, 2008.

[33] R. Grimm, M. Weidemüller, and Y. B. Ovchinnikov. Optical dipole traps for neutral atoms. *Adv. At. Mol. Phys.*, 42:95, 2000.

[34] N. W. Ashcroft and M. D. Mermin. *Solid State Physics*. Brooks Cole, first edition, 1976.

[35] O. Morsch and M. Oberthaler. Dynamics of Bose-Einstein condensates in optical lattices. *Rev. Mod. Phys.*, 78:179, 2006.

[36] F. S. Cataliotti, S. Burger, C. Fort, P. Maddaloni, F. Minardi, A. Trombettoni, A. Smerzi, and M. Inguscio. Josephson Junction Arrays with Bose-Einstein Condensates. *Science*, 293:843, 2001.

[37] A. Trombettoni and A. Smerzi. Discrete Solitons and Breathers with Dilute Bose-Einstein Condensates. *Phys. Rev. Lett.*, 86:2353, 2001.

[38] A. Smerzi and A. Trombettoni. Nonlinear tight-binding approximation for Bose-Einstein condensates in a lattice. *Phys. Rev. A*, 68:23613, 2003.

[39] R. E. Peierls. *Quantum Theory of Solids*. Clarendon Press, Oxford, second edition, 2001.

[40] R. Peierls. Zur Theorie des Diamagnetismus von Leitungselektronen. *Z. Phys.*, 80:763, 1933.

[41] P. G. Harper. Single Band Motion of Conduction Electrons in a Uniform Magnetic Field. *Proc. Phys. Soc.*, 68:874, 1955.

[42] L.-M. Duan, E. Demler, and M. Lukin. Controlling Spin Exchange Interactions of Ultracold Atoms in Optical Lattices. *Phys. Rev. Lett.*, 91:90402, 2003.

[43] A. B. Kuklov and B. V. Svistunov. Counterflow Superfluidity of Two-Species Ultracold Atoms in a Commensurate Optical Lattice. *Phys. Rev. Lett.*, 90:100401, 2003.

[44] J. K. Pachos and M. B. Plenio. Three-Spin Interactions in Optical Lattices and Criticality in Cluster Hamiltonians. *Phys. Rev. Lett.*, 93:56402, 2004.

[45] S. Sachdev. *Quantum Phase Transitions*. Cambridge University Press, first edition, 2001.

[46] A. Harsono. *Dipole trapping and manipulation of ultra-cold atoms*. PhD thesis, University of Oxford, UK, 2006.

[47] B. Fletcher. *A rotating optical lattice for ultracold atoms*. PhD thesis, University of Oxford, UK, 2008.

[48] R. A. Williams. *Vortex nucleation in a rotating optical lattice of ultracold atoms*. PhD thesis, University of Oxford, UK, 2009.

[49] E. L. Raab, M. Prentiss, A. Cable, S. Chu, and D. E. Pritchard. Trapping of neutral sodium atoms with radiation pressure. *Phys. Rev. Lett.*, 59:2631, 1987.

[50] K. I. Lee, J. A. Kim, H. R. Noh, and W. Jhe. Single-beam atom trap in a pyramidal and conical hollow mirror. *Optics Letters*, 21:1177, 1996.

[51] J. J. Arlt, O. Maragò, S. Webster, S. Hopkins, and C. J. Foot. A pyramidal magneto-optical trap as a source of slow atoms. *Opt. Commun.*, 157:303, 1998.

[52] P. Baranowski, J. Zacks, G. Hechenblaikner, and C. J. Foot. Testing and design of a lens system for atom trapping and fluorescence detection. *arXiv*, physics.optics:0412126v1, 2004.

[53] W. Alt. An objective lens for efficient fluorescence detection of single atoms. *Optik*, 113:142, 2002.

[54] R. A. Williams, J. D. Pillet, S. Al-Assam, B. Fletcher, M. Shotter, and C. Foot. Dynamic optical lattices: two-dimensional rotating and accordion lattices for ultracold atoms. *Opt. Express*, 16:16977, 2008.

[55] R. A. Williams, S. Al-Assam, and C. Foot. Observation of Vortex Nucleation in a Rotating Two-Dimensional Lattice of Bose-Einstein Condensates. *Phys. Rev. Lett.*, 104:050404, 2010.

[56] S. Friebel, C. D'andrea, J. Walz, M. Weitz, and T. W. Hänsch. CO_2-laser optical lattice with cold rubidium atoms. *Phys. Rev. A*, 57:20, 1998.

[57] M. Cristiani, O. Morsch, J. H. Müller, D. Ciampini, and E. Arimondo. Experimental properties of Bose-Einstein condensates in one-dimensional optical lattices: Bloch oscillations, Landau-Zener tunneling, and mean-field effects. *Phys. Rev. A*, 65:63612, 2002.

[58] P. L. Gould, G. A. Ruff, and D. E. Pritchard. Diffraction of atoms by light - The near-resonant Kapitza-Dirac effect. *Phys. Rev. Lett.*, 56:827, 1986.

[59] J. H. Huckans, I. B. Spielman, B. Laburthe Tolra, W. D. Phillips, and J. V. Porto. Quantum and classical dynamics of a Bose-Einstein

condensate in a large-period optical lattice. *Phys. Rev. A*, 80:43609, 2009.

[60] J. H. Denschlag, J. E. Simsarian, H. Häffner, C. McKenzie, A. Browaeys, D. Cho, K. Helmerson, S. L. Rolston, and W. D. Phillips. A Bose-Einstein condensate in an optical lattice. *J. Phys. B*, 35:3095, 2002.

[61] O. Morsch, J. H. Müller, D. Ciampini, M. Cristiani, P. B. Blakie, C. J. Williams, P. S. Julienne, and E. Arimondo. Decay and revival of phase coherence of a Bose-Einstein condensate in a one-dimensional lattice. *Phys. Rev. A*, 67:31603, 2003.

[62] S. Al-Assam, R. A. Williams, and C. Foot. Ultracold atoms in an optical lattice with dynamically variable periodicity. *Phys. Rev. A*, 82:021604, 2010.

[63] D. Jaksch. Optical lattices, ultracold atoms and quantum information processing. *Contemp. Phys.*, 45:367, 2004.

[64] K. D. Nelson, X. Li, and D. S. Weiss. Imaging single atoms in a three-dimensional array. *Nature Physics*, 3:556, 2007.

[65] A. Itah, H. Veksler, O. Lahav, A. Blumkin, C. Moreno, C. Gordon, and J. Steinhauer. Direct Observation of a Sub-Poissonian Number Distribution of Atoms in an Optical Lattice. *Phys. Rev. Lett.*, 104:113001, 2010.

[66] R. Scheunemann, F. S. Cataliotti, Theodor W Hänsch, and M. Weitz. Resolving and addressing atoms in individual sites of a CO_2-laser optical lattice. *Phys. Rev. A*, 62:51801, 2000.

[67] T. Gericke, P. Würtz, D. Reitz, T. Langen, and H. Ott. High-resolution scanning electron microscopy of an ultracold quantum gas. *Nature Physics*, 4:949, 2008.

[68] A. Burrell, D. J. Szwer, S. C. Webster, and D. M. Lucas. Scalable simultaneous multiqubit readout with 99.99% single-shot fidelity. *Phys. Rev. A*, 81:40302, 2010.

[69] R. Raussendorf and H. J. Briegel. A One-Way Quantum Computer. *Phys. Rev. Lett.*, 86:5188, 2001.

[70] B. Vaucher, A. Nunnenkamp, and D. Jaksch. Creation of resilient entangled states and a resource for measurement-based quantum computation with optical superlattices. *New J. Phys.*, 10:3005, Feb 2008.

[71] L. Fallani, C. Fort, J. E. Lye, and M. Inguscio. Bose-Einstein condensate in an optical lattice with tunable spacing: transport and static properties. *Opt. Express*, 13:4303, 2005.

[72] S. Schmid, G. Thalhammer, K. Winkler, F. Lang, and J. H. Denschlag. Long distance transport of ultracold atoms using a 1D optical lattice. *New J. Phys.*, 8:159, 2006.

[73] T. C. Li, H. Kelkar, D. Medellin, and M. G. Raizen. Real-time control of the periodicity of a standing wave: an optical accordion. *Opt. Express*, 16:5465, 2008.

[74] E. Peik, M. Ben Dahan, I. Bouchoule, Y. Castin, and C. Salomon. Bloch oscillations of atoms, adiabatic rapid passage, and monokinetic atomic beams. *Phys. Rev. A*, 55:2989, 1997.

[75] R. A. Williams. Private Communication.

[76] A. Eckardt, C. Weiss, and M. Holthaus. Superfluid-Insulator Transition in a Periodically Driven Optical Lattice. *Phys. Rev. Lett.*, 95:260404, 2005.

[77] A. Zenesini, H. Lignier, D. Ciampini, O. Morsch, and E. Arimondo. Coherent Control of Dressed Matter Waves. *Phys. Rev. Lett.*, 102:100403, 2009.

[78] V. G. Rousseau, G. G. Batrouni, D. E. Sheehy, J. Moreno, and M. Jarrell. Pure Mott Phases in Confined Ultracold Atomic Systems. *Phys. Rev. Lett.*, 104:167201, 2010.

[79] A. L. Fetter. Rotating trapped Bose-Einstein condensates. *Rev. Mod. Phys.*, 81:647, 2009.

[80] N. R. Cooper. Rapidly rotating atomic gases. *Adv. Phys.*, 57:539, 2008.

[81] J. Dalibard, F. Gerbier, G. Juzeliūnas, and Patrik Öhberg. Artificial gauge potentials for neutral atoms. *arXiv*, cond-mat.quant-gas:1008.5378v1, 2010.

[82] L. D. Landau and E. M. Lifshitz. *Mechanics*. Pergamon Press, Oxford, third edition, 1976.

[83] M. Cheneau, S. P. Rath, T. Yefsah, K. J. Günter, G. Juzeliūnas, and J. Dalibard. Geometric potentials in quantum optics: A semi-classical interpretation. *Europhys. Lett.*, 83:60001, 2008.

[84] I. B. Spielman. Raman processes and effective gauge potentials. *Phys. Rev. A*, 79:63613, 2009.

[85] Y.-J. Lin, R. L. Compton, A. R. Perry, W. D. Phillips, J. V. Porto, and I. B. Spielman. Bose-Einstein Condensate in a Uniform Light-Induced Vector Potential. *Phys. Rev. Lett.*, 102:130401, 2009.

[86] Y.-J. Lin, R. L. Compton, K. Jimenez-Garcia, J. V. Porto, and I. B. Spielman. Synthetic magnetic fields for ultracold neutral atoms. *Nature*, 462:628, 2009.

[87] G. Juzeliūnas and P. Öhberg. Slow Light in Degenerate Fermi Gases. *Phys. Rev. Lett.*, 93:33602, 2004.

[88] G. Juzeliūnas, P. Öhberg, J. Ruseckas, and A. Klein. Effective magnetic fields in degenerate atomic gases induced by light beams with orbital angular momenta. *Phys. Rev. A*, 71:53614, 2005.

[89] D. Jaksch and P. Zoller. Creation of effective magnetic fields in optical lattices: the Hofstadter butterfly for cold neutral atoms. *New J. Phys.*, 5:56, 2003.

[90] F. Gerbier and J. Dalibard. Gauge fields for ultracold atoms in optical superlattices. *New J. Phys.*, 12:3007, 2010.

[91] A. Klein and D. Jaksch. Phonon-induced artificial magnetic fields in optical lattices. *Europhys. Lett.*, 85:13001, 2009.

[92] M. Rosenkranz, A. Klein, and D. Jaksch. Simulating and detecting artificial magnetic fields in trapped atoms. *Phys. Rev. A*, 81:13607, 2010.

[93] A. S. Sorensen, E. Demler, and M. Lukin. Fractional quantum Hall states of atoms in optical lattices. *Phys. Rev. Lett.*, 94:086803, 2005.

[94] K. Osterloh, M. Baig, L. Santos, P. Zoller, and M. Lewenstein. Cold Atoms in Non-Abelian Gauge Potentials: From the Hofstadter 'Moth' to Lattice Gauge Theory. *Phys. Rev. Lett.*, 95:10403, 2005.

[95] D. R. Hofstadter. Energy levels and wave functions of Bloch electrons in rational and irrational magnetic fields. *Phys. Rev. B*, 14:2239, 1976.

[96] R. Palmer and D. Jaksch. High-Field Fractional Quantum Hall Effect in Optical Lattices. *Phys. Rev. Lett.*, 96:180407, 2006.

[97] R. Bhat, M. Krämer, J. Cooper, and M. J. Holland. Hall effects in Bose-Einstein condensates in a rotating optical lattice. *Phys. Rev. A*, 2007.

[98] S. Teitel and C. Jayaprakash. Josephson-Junction Arrays in Transverse Magnetic Fields. *Phys. Rev. Lett.*, 51:1999, 1983.

[99] T. C. Halsey. Josephson-Junction Arrays in Transverse Magnetic-Fields - Ground-States and Critical Currents. *Phys. Rev. B*, 31:5728, 1985.

[100] K. Kasamatsu. Uniformly frustrated bosonic Josephson-junction arrays. *Phys. Rev. A*, 79:021604, 2009.

[101] M. Polini, R. Fazio, A. H. MacDonald, and M. P. Tosi. Realization of fully frustrated Josephson-junction arrays with cold atoms. *Phys. Rev. Lett.*, 95:010401, 2005.

[102] C. Raman, J. R. Abo-Shaeer, J. M. Vogels, K. Xu, and W. Ketterle. Vortex Nucleation in a Stirred Bose-Einstein Condensate. *Phys. Rev. Lett.*, 87:210402, 2001.

[103] A. A. Svidzinsky and A. L. Fetter. Stability of a Vortex in a Trapped Bose-Einstein Condensate. *Phys. Rev. Lett.*, 84:5919, 2000.

[104] V. Schweikhard, I. Coddington, P. Engels, V. P. Mogendorff, and E. A. Cornell. Rapidly Rotating Bose-Einstein Condensates in and near the Lowest Landau Level. *Phys. Rev. Lett.*, 92:40404, 2004.

[105] T. Anker, M. Albiez, R. Gati, S. Hunsmann, B. Eiermann, A. Trombettoni, and M. K. Oberthaler. Nonlinear Self-Trapping of Matter Waves in Periodic Potentials. *Phys. Rev. Lett.*, 94:20403, 2005.

[106] A. Smerzi, S. Fantoni, S. Giovanazzi, and S. R. Shenoy. Quantum Coherent Atomic Tunneling between Two Trapped Bose-Einstein Condensates. *Phys. Rev. Lett.*, 79:4950, 1997.

[107] S. Tung, V. Schweikhard, and E. A. Cornell. Observation of vortex pinning in Bose-Einstein condensates. *Phys. Rev. Lett.*, 97:240402, 2006.

[108] A. A. Abrikosov. On the Magnetic Properties of Superconductors of the Second Group. *Sov Phys Jetp-Ussr*, 5:1174, 1957.

[109] H. Pu, L. O. Baksmaty, S. Yi, and N. P. Bigelow. Structural phase transitions of vortex matter in an optical lattice. *Phys. Rev. Lett.*, 94:190401, 2005.

[110] D. S. Goldbaum and E. J. Mueller. Commensurability and hysteretic evolution of vortex configurations in rotating optical lattices. *Phys. Rev. A*, 79:063625, 2009.

[111] R. Palmer, A. Klein, and D. Jaksch. Optical lattice quantum Hall effect. *Phys. Rev. A*, 78:013609, 2008.

[112] S. Powell, R. Barnett, R. Sensarma, and S. Das Sarma. Bogoliubov theory of interacting bosons on a lattice in a synthetic magnetic field. *arXiv*, cond-mat.quant-gas:1009.1389v1, 2010.

[113] S. Powell, R. Barnett, R. Sensarma, and S. Das Sarma. Interacting Hofstadter Spectrum of Atoms in an Artificial Gauge Field. *Phys. Rev. Lett.*, 104:255303, 2010.

[114] N. R. Cooper, N. Wilkin, and J. Gunn. Quantum Phases of Vortices in Rotating Bose-Einstein Condensates. *Phys. Rev. Lett.*, 87:120405, 2001.

[115] D. C. Tsui, H. L. Stormer, and A. C. Gossard. Two-Dimensional Magnetotransport in the Extreme Quantum Limit. *Phys. Rev. Lett.*, 48:1559, 1982.

[116] R. B. Laughlin. Anomalous quantum Hall effect - An incompressible quantum fluid with fractionally charged excitations. *Phys. Rev. Lett.*, 50:1395, 1983.

[117] N. R. Cooper and N. Wilkin. Composite fermion description of rotating Bose-Einstein condensates. *Phys. Rev. B*, 60:R16279, 1999.

[118] N. Gemelke, E. Sarajlic, and S. Chu. Rotating Few-body Atomic Systems in the Fractional Quantum Hall Regime. *arXiv*, cond-mat.quant-gas:1007.2677, 2010.

[119] M. Hafezi, A. S. Sorensen, E. Demler, and M. Lukin. Fractional quantum Hall effect in optical lattices. *Phys. Rev. A*, 76:023613, 2007.

[120] R. O. Umucalilar and E. J. Mueller. Fractional quantum Hall states in the vicinity of Mott plateaus. *Phys. Rev. A*, 81:053628, 2010.

[121] G. Moller and N. R. Cooper. Composite fermion theory for bosonic quantum Hall states on lattices. *Phys. Rev. Lett.*, 103:105303, 2009.

[122] E. Kapit and E. J. Mueller. Parent Hamiltonian for the Fractional Quantum Hall States in an Optical Lattice. *arXiv*, cond-mat.quant-gas:1005.3282, 2010.

[123] N. R. Cooper, F. J. M. van Lankvelt, J. W. Reijnders, and K. Schoutens. Quantum Hall states of atomic Bose gases: Density profiles in single-layer and multilayer geometries. *Phys. Rev. A*, 72:063622, 2005.

[124] M. D. Barrett, J. A. Sauer, and M. S. Chapman. All-Optical Formation of an Atomic Bose-Einstein Condensate. *Phys. Rev. Lett.*, 87:10404, 2001.

[125] A. E. Leanhardt, T. A. Pasquini, M. Saba, A. Schirotzek, Y. Shin, D. Kielpinski, D. E. Pritchard, and W. Ketterle. Cooling Bose-Einstein Condensates Below 500 Picokelvin. *Science*, 301:1513, 2003.

[126] D. McKay and B. DeMarco. Cooling in strongly correlated optical lattices: prospects and challenges. *arXiv*, cond-mat.quant-gas:1010.0198v1, 2010.

[127] P. Medley, D. M. Weld, H. Miyake, D. E. Pritchard, and W. Ketterle. Spin gradient demagnetization cooling of ultracold atoms. *arXiv*, cond-mat.quant-gas:1006.4674v3, 2010.

[128] A. G. Morris and D. L. Feder. Gaussian Potentials Facilitate Access to Quantum Hall States in Rotating Bose Gases. *Phys. Rev. Lett.*, 99:240401, 2007.

[129] M. Gildemeister, E. Nugent, B. E. Sherlock, M. Kubasik, B. T. Sheard, and C. J. Foot. Trapping ultracold atoms in a time-averaged adiabatic potential. *Phys. Rev. A*, 81:31402, 2010.

[130] M. Popp, B. Paredes, and J. I. Cirac. Adiabatic path to fractional quantum Hall states of a few bosonic atoms. *Phys. Rev. A*, 70:53612, 2004.

[131] M. Shotter. Design of a technique to measure the density of ultracold atoms in a short-period optical lattice in three dimensions with single atom sensitivity. *arXiv*, cond-mat.quant-gas:1011.5609v1, 2010.

[132] M. Shotter. *The development of techniques to prepare and probe at single atom resolution strongly interacting quantum systems of ultracold atoms*. PhD thesis, University of Oxford, UK, 2009.

[133] J. I. Cirac and F. Verstraete. Renormalization and tensor product states in spin chains and lattices. *J. Phys. A: Math. Theor.*, 42:4004, 2009.

[134] H. J. Changlani, J. Kinder, C. J. Umrigar, and G. K.-L. Chan. Approximating strongly correlated wave functions with correlator product states. *Phys. Rev. B*, 80:245116, 2009.

[135] F. Mezzacapo, N. Schuch, M. Boninsegni, and J. I. Cirac. Ground-state properties of quantum many-body systems: entangled-plaquette states and variational Monte Carlo. *New J. Phys.*, 11:083026, 2009.

[136] J. Eisert, M. Cramer, and M. B. Plenio. Colloquium: Area laws for the entanglement entropy. *Rev. Mod. Phys.*, 82:277, 2010.

[137] F. Verstraete, V. Murg, and J. I. Cirac. Matrix product states, projected entangled pair states, and variational renormalization group methods for quantum spin systems. *Adv. Phys.*, 57:143, 2008.

[138] A. Kitaev and J. Preskill. Topological Entanglement Entropy. *Phys. Rev. Lett.*, 96:110404, 2006.

[139] M. Cramer, J. Eisert, M. B. Plenio, and J. Dreißig. Entanglement-area law for general bosonic harmonic lattice systems. *Phys. Rev. A*, 73:12309, 2006.

[140] U. Schollwöck. The density-matrix renormalization group. *Rev. Mod. Phys.*, 77:259, 2005.

[141] U. Schollwöck. The density-matrix renormalization group in the age of matrix product states. *eprint arXiv*, cond-mat.str-el:1008.3477v1, 2010.

[142] G. Vidal. Efficient Simulation of One-Dimensional Quantum Many-Body Systems. *Phys. Rev. Lett.*, 93:40502, 2004.

[143] M. Fannes, B. Nachtergaele, and R. F. Werner. Finitely correlated states on quantum spin chains. *Commun. Math. Phys.*, 144:443, 1992.

[144] F. Verstraete and J. I. Cirac. Matrix product states represent ground states faithfully. *Phys. Rev. B*, 73:94423, 2006.

[145] F. Verstraete and J. I. Cirac. Renormalization algorithms for Quantum-Many Body Systems in two and higher dimensions. *arXiv*, cond-mat.str-el:0407066v1, 2004.

[146] V. Murg, F. Verstraete, and J. I. Cirac. Variational study of hard-core bosons in a two-dimensional optical lattice using projected entangled pair states. *Phys. Rev. A*, 75:33605, 2007.

[147] L. Wang, I. Pizorn, and F. Verstraete. Monte Carlo simulation with Tensor Network States. *arXiv*, cond-mat.str-el:1010.5450v1, 2010.

[148] N. Schuch, M. M. Wolf, F. Verstraete, and J. I. Cirac. Simulation of Quantum Many-Body Systems with Strings of Operators and Monte Carlo Tensor Contractions. *Phys. Rev. Lett.*, 100:40501, 2008.

[149] F. Mezzacapo and J. I. Cirac. Ground-state properties of the spin-1/2 antiferromagnetic Heisenberg model on the triangular lattice: A variational study based on entangled-plaquette states. *arXiv*, 12:103039.

[150] E. Neuscamman, H. Changlani, J. Kinder, and G. K.-L. Chan. Further developments in correlator product states: deterministic optimization and energy evaluation. *arXiv*, cond-mat.str-el:1008.4945v1, 2010.

[151] S. R. Clark. *Strongly correlated one-dimensional systems of cold atoms in optical lattices*. PhD thesis, University of Oxford, UK, 2007.

[152] J. Lou and A. W. Sandvik. Variational ground states of two-dimensional antiferromagnets in the valence bond basis. *Phys. Rev. B*, 76:104432, 2007.

[153] A. W. Sandvik and G. Vidal. Variational quantum Monte Carlo simulations with tensor-network states. *Phys. Rev. Lett.*, 99:220602, 2007.

[154] N. Metropolis, A. W. Rosenbluth, M. N. Rosenbluth, A. H. Teller, and E. Teller. Equation of State Calculations by Fast Computing Machines. *J. Chem. Phys.*, 21:1087, 1953.

[155] D. Bitko, T. F. Rosenbaum, and G. Aeppli. Quantum Critical Behavior for a Model Magnet. *Phys. Rev. Lett.*, 77:940, 1996.

[156] C. J. Hamer. Finite-size scaling in the transverse Ising model on a square lattice. *J. Phys. A*, 33:6683, 2000.

[157] H. Rieger and N. Kawashima. Application of a continuous time cluster algorithm to the two-dimensional random quantum Ising ferromagnet. *Eur. Phys. J. B*, 9:233, 1999.

[158] H.W. Blöte and Y. Deng. Cluster Monte Carlo simulation of the transverse Ising model. *Phys. Rev. E*, 66:66110, 2002.

[159] M. S. L. Du Croo de Jongh and J. M. J. van Leeuwen. Critical behavior of the two-dimensional Ising model in a transverse field: A density-matrix renormalization calculation. *Phys. Rev. B*, 57:8494, 1998.

[160] L. Tagliacozzo, G. Evenbly, and G. Vidal. Simulation of two-dimensional quantum systems using a tree tensor network that exploits the entropic area law. *Phys. Rev. B*, 80:235127, 2009.

[161] A. E. Feiguin, E. Rezayi, C. Nayak, and S. Das Sarma. Density Matrix Renormalization Group Study of Incompressible Fractional Quantum Hall States. *Phys. Rev. Lett.*, 100:166803, 2008.

[162] D. L. Kovrizhin. Density matrix renormalization group for bosonic quantum Hall effect. *Phys. Rev. B*, 81:125130, 2010.

[163] S. Iblisdir, J. I. Latorre, and R. Orús. Entropy and Exact Matrix-Product Representation of the Laughlin Wave Function. *Phys. Rev. Lett.*, 98:60402, 2007.

[164] B. Béri and N. R. Cooper. Local tensor network for strongly correlated projective states. *arXiv*, cond-mat.str-el:1101.5610v1, 2011.

[165] Z.-C. Gu, F. Verstraete, and X.-G. Wen. Grassmann tensor network states and its renormalization for strongly correlated fermionic and bosonic states. *arXiv*, cond-mat.str-el:1004.2563v1, 2010.

[166] N. Read and E. Rezayi. Quasiholes and fermionic zero modes of paired fractional quantum Hall states: The mechanism for non-Abelian statistics. *Phys. Rev. B*, 54:92260, 1996.

[167] O. Ciftja and C. Wexler. Monte Carlo simulation method for Laughlin-like states in a disk geometry. *Phys. Rev. B*, 67:75304, 2003.

[168] O. Ciftja. Monte Carlo study of Bose Laughlin wave function for filling factors 1/2, 1/4 and 1/6. *Europhys. Lett.*, 74:486, 2006.

[169] D. Ceperley, G. V. Chester, and M. H. Kalos. Monte Carlo simulation of a many-fermion study. *Phys. Rev. B*, 16:3081, 1977.

[170] B. Paredes, P. O. Fedichev, J. I. Cirac, and P. Zoller. 1/2-Anyons in Small Atomic Bose-Einstein Condensates. *Phys. Rev. Lett.*, 87:10402, 2001.

[171] C. Nayak, S. H. Simon, A. Stern, M. Freedman, and S. Das Sarma. Non-Abelian anyons and topological quantum computation. *Rev. Mod. Phys.*, 80:1083, 2008.

[172] A. Eckardt, P. Hauke, P. Soltan-Panahi, C. Becker, K. Sengstock, and M. Lewenstein. Frustrated quantum antiferromagnetism with ultracold bosons in a triangular lattice. *Europhys. Lett.*, 89:10010, 2010.

[173] L. D. Carr, D. DeMille, R. V. Krems, and J. Ye. Cold and ultracold molecules: science, technology and applications. *New J. Phys.*, 11:5049, 2009.

[174] B. Capogrosso-Sansone, C. Trefzger, M. Lewenstein, P. Zoller, and G. Pupillo. Quantum Phases of Cold Polar Molecules in 2D Optical Lattices. *Phys. Rev. Lett.*, 104:125301, 2010.

[175] L. Pollet, J. D. Picon, H. P. Büchler, and M. Troyer. Supersolid Phase with Cold Polar Molecules on a Triangular Lattice. *Phys. Rev. Lett.*, 104:125302, 2010.

[176] A. Micheli, G. K. Brennen, and P. Zoller. A toolbox for lattice-spin models with polar molecules. *Nature Physics*, 2:341, 2006.

[177] N. R. Cooper and G. V. Shlyapnikov. Stable Topological Superfluid Phase of Ultracold Polar Fermionic Molecules. *Phys. Rev. Lett.*, 103(15):155302, 2009.

[178] W. Bao, D. Jaksch, and P. A. Markowich. Numerical solution of the Gross-Pitaevskii equation for Bose-Einstein condensation. *J. Comput. Phys.*, 187:318, 2003.

[179] W. Bao and H. Wang. An efficient and spectrally accurate numerical method for computing dynamics of rotating Bose–Einstein condensates. *J. Comput. Phys.*, 217:612, 2006.